

POLITECNICO DI TORINO

Master's Degree in ARCHITECTURE FOR THE SUSTAINABILITY
DESIGN



**Politecnico
di Torino**

Master's Degree Thesis
Academic Year 2021/2022

The Contribution of UAV Photogrammetry for 3D Documentation.
Accuracy evaluation using the EuroSDR Benchmark and Villa Ghia test sites

Supervisor:
Filiberto Chiabrando

Candidate:
Mehmet Ali Kurt s275811

Co-supervisors:
Alessio Calantropio
Lorenzo Teppati Losè

SEPTEMBER 2022

Contents

Contents.....	iii
List of Figures	v
List of Tables	vii
Abstract.....	viii
Abbreviations	ix
1. Introduction	1
2. Methodology.....	5
2.1. Geomatics	5
2.2. Definition and History of Photogrammetry	6
2.3. Terrestrial Photogrammetry	8
2.4. Definition of UAV and UAV Photogrammetry.....	9
2.5. Digital Photogrammetry.....	13
2.5.1 Evolution of Camera Sensors	13
2.5.2 Metric Cameras:.....	14
2.5.3 Non-Metric Cameras:.....	15
2.6. Principles and Fundamentals of Photogrammetry	16
2.7 Structure from Motion (SFM)	18
2.7.1. Bundle Adjustment	18
2.8. Application	19
3. Test Areas.....	22
3.1. Benchmark - Wards Hill Quarry	22
3.2. Villa Ghia and Ciabòt delle Guardie	23
3.3 Ciabòt delle Guardie	25
4. Data Acquisition	27
4.1. Test Field Details	27
4.1.1. EUROS DR Benchmark.....	27
4.1.2. Villa Ghia	30
4.2. UAV and Camera Sensors.....	31
5. Data Processing.....	35
5.1. Image Orientation	36
5.2. Georeferencing with GCPs	38
5.2.1 Georeferencing without Ground Control Points.....	40

5.3. Tie Points Filtering.....	41
5.4. Building Dense Cloud	43
5.5. Generate Mesh and Texture	44
5.6. Generate of Digital Elevation Models and Orthoprojection	45
5.7. Cloud-to-Cloud (C2C) Distance:	47
6. Model Analysis and Results.....	50
6.1. Benchmark Case Study.....	50
6.1.1. Benchmark – DJI Zenmuse P1	55
6.1.2. Benchmark – DJI Phantom 4 RTK	61
6.1.3. Benchmark – DJI Zenmuse L1	63
6.2. Villa Ghia Case Study.....	66
6.2.1. Villa Ghia DJI Zenmuse P1 - Metashape.....	66
6.2.2. Villa Ghia DJI Zenmuse P1– Reality Capture	71
6.2.3. Villa Ghia DJI Zenmuse L1 - Metashape	74
6.2.4. Villa Ghia DJI Zenmuse L1–Reality Capture	75
6.2.5. Villa Ghia DJI Phantom 4 RTK - Metashape.....	76
6.2.6. Villa Ghia DJI Phantom 4 RTK– Reality Capture	79
6.3. Cloud-to-Cloud Distance Analysis Results.....	80
6.4. Density Analysis Results	85
7. Discussion & Conclusion	89
7.1. Discussion.....	90
7.1.1. Benchmark – DJI Zenmuse P1	90
7.1.2. Benchmark – DJI PHANTOM 4 RTK	90
7.1.3. Benchmark - DJI Zenmuse L1	91
7.1.4. Villa Ghia – Metashape DJI Zenmuse P1	91
7.1.5. Villa Ghia Metashape – DJI Phantom 4 RTK.....	91
7.1.6. Villa Ghia Metashape – DJI Zenmuse L1	92
7.1.7. Villa Ghia Reality Capture DJI Zenmuse P1	92
7.1.8. Villa Ghia Reality Capture DJI Phantom 4 RTK	93
7.1.9. Villa Ghia Reality Capture Zenmuse L1	93
7.2. Limitations of the UAV Photogrammetry Technology	93
7.3. Future Research	95
7.4. Conclusion.....	96

References:	98
Acknowledgment	104

List of Figures

Figure 2. 1 Relationship between the elements of geomatics (De Wulf et al. 2014)	6						
Figure 2. 2 Photogrammetric camera development from the 1850s to the 1980s (Luhman et al., 2011)	7						
Figure 2. 3 Major photogrammetric phases as a result of technological innovations. (Schenk, 2005).....	8						
Figure 2. 4 Aerial surveying technique by plane from 20s and Figure 2. 5 model helicopter aerial survey from 80s (The brownstone detectives, 2020, Wester-Ebbinghaus, 1980).	9						
Figure 2. 6 the adapted use of UAVs in leading industries (Wackwitz & Bödecker, 2008).....	11						
Figure 2. 7 Quadcopter	Figure 2. 8 Fixed-Wing UAV	12					
Figure 2. 9 Model airplane Firma Hegi, Przybilla 1979.	13						
Figure 2. 10 Distortion Types (Pilar Valerga Puerta et al., 2020).	15						
Figure 2. 11 Principles of Photogrammetry the Approximation of 2D measurements on stereo photographs to facilitate 3D mapping of the point on the ground (Osborn et al. 2018)	17						
Figure 2. 12 Representation of the demonstration of the bundle-adjustment technique performed by Reality Capture.	19						
Figure 3. 1 Geolocation of survey site	22						
Figure 3. 2 Panoramic view of Ward's Hill Quarry. (Figure from https://geospatialincl.github.io/eurosdrrpas-benchmark)	22						
Figure 3. 3 Site location of Villa Ghia.	23						
Figure 3. 4 Aerial view of Villa Ghia with its external surrounded walls	23						
Figure 3. 5 Ground floor and first-floor plans of Villa Ghia	24						
Figure 3. 6 Elevation of the Ciabòt delle Guardie	25						
Figure 3. 7 Ground floor plan of the Ciabòt	25						
Figure 4. 1 Flight mission path of the Benchmark test site.....	29						
Figure 4. 2 ICP and GCP target location of Benchmark. Figure 4. 3 CP label sprayed for identification	29						
Figure 4. 4 DJI Matrice 300 RTK (Figure from https://www.ingeniovirtual.com)	32						
Figure 4. 5 DJI Zenmuse P1	Figure 4. 6 DJI Zenmuse L1	Figure 4. 7 DJI Phantom 4 RTK	(Figure from https://www.dji.com)	(Figure from https://www.dji.com)	(Figure from https://www.dji.com)	33
Figure 5. 1 – Image orientation of model in Metashape	36						
Figure 5. 2 Matched points can be viewed in Agisoft MetaShape after the alignment is done. The blue lines show valid matching, while the red ones indicated non-matched.	37						
Figure 5. 3 Modules of Ground Control Points (GCPs).....	38						
Figure 5. 4 Leica GNSS1200	Figure 5. 5 GNSS on a tripod	39					
Figure 5. 6 Work principle of RTK.....	41						
Figure 5. 7 Noise filtering point selection in the model.....	42						
Figure 5. 8 and Figure 5. 9 Generated Photogrammetric Model of Villa Ghia in Reality Capture, Mesh (left) and Textured Model (right).....	44						
Figure 5. 10 And Figure 5. 11 the Digital Surface Model (left) and the Digital Terrain Model (right).	45						
Figure 5. 12 and Figure 5. 13 two Digital Surface Models from the exact location but processed with different software. (Left - Reality Capture and right – Metashape).....	46						
Figure 5. 14 and Figure 5. 15 the difference between mesh (left) and Orthoprojection photo (right).....	46						
Figure 5. 16 and Figure 5. 17 Orthoprojection seamline method taken by different software.	47						

Figure 5. 18 The scheme of Cloud-to-Cloud work principle	48
Figure 5. 19 C2C distance analysis generated by CloudCompare	49
Figure 6. 1 the generated contour lines of the Benchmark site by Agisoft Metashape. It can be seen the elevation difference of the quarry in the center of the model.	55
Figure 6. 2 the Total Error values of the DJI Zenmuse P1 Sensor.....	57
Figure 6. 3 the Orthoprojection image of the DJI Zenmuse P1 sensor's model	58
.....	60
Figure 6. 4 Workflow steps, camera location, mesh, texture, and Digital Elevation Model, Orthoprojection of DJI Zenmuse P1's model in Benchmark	60
Figure 6. 5 Orthoprojection image of DJI Phantom 4 RTK.....	61
Figure 6. 6 Total Error comparison of different phases of the DJI Phantom 4 RTK sensor.....	63
Figure 6. 7	64
Orthoprojection image of DJI Zenmuse L1	64
Figure 6. 8	64
Digital Elevation Model of DJI Zenmuse P1	64
Figure 6. 9 Total Error comparison of different phases of the DJI Zenmuse L1 sensor.....	66
Figure 6. 10 Orthoprojection image of DJI Zenmuse P1 in Villa Ghia	68
Figure 6. 11	70
Workflow steps, camera location, and Digital Elevation Model of DJI Zenmuse P1's model in Villa Ghia	70
.....	70
Figure 6. 12 Orthoprojection image of DJI Zenmuse P1 processed by Reality Capture	72
Figure 6. 13 Workflow steps, Model's seamlines, and Digital Elevation Model of DJI Zenmuse P1's model in Villa Ghia generated by Reality Capture	73
Figure 6. 14 Orthoprojection image of DJI Zenmuse L1 processed by Metashape.....	75
Figure 6. 15 Orthoprojection image of DJI Zenmuse L1 processed by Reality Capture.....	75
Figure 6. 16 Orthoprojection image of DJI Phantom 4 RTK processed by Metashape.....	78
Figure 6. 17 Orthoprojection image of DJI Phantom 4 RTK processed by Reality Capture.....	78
Figure 6. 18 Cloud-to-cloud (C2C) Distance of DJI Zenmuse P1 and DJI Phantom 4 RTK Sensors generated by Metashape cloud model.....	81
Figure 6. 19 The Cloud-to-cloud Distance computation of DJI Zenmuse P1 and DJI Zenmuse L1 sensors generated by Metashape cloud.....	82
Figure 6. 20 Cloud-to-cloud (C2C) Distance of Zenmuse P1 and Phantom 4 RTK Sensors generated by Reality Capture cloud model.....	83
Figure 6. 21 The Cloud-to-cloud Distance computation of Zenmuse P1 and Zenmuse L1 sensors generated by the Reality Capture cloud	84
Figure 6. 22 the DJI Zenmuse P1 Sensor's Cloud Density analyses.....	86
Figure 6. 23 the density analyses of the DJI Phantom 4 RTK sensor from the Metashape and Reality Capture (The model above – Metashape, the model below – Reality Capture).....	87
Figure 6. 24 the DJI Zenmuse L1 Sensor's Cloud Density analyses.....	88

List of Tables

Table 4. 1 comparison between the DJI Matrice 300 and Phantom 4 RTK drones used in these case studies.	32
Table 4. 2 the comparison of the DJI ZenMuse P1, DJI Phantom 4 RTK, and DJI ZenMuse L1 camera sensors used in Benchmark and Villa Ghia surveys.	33
Table 6. 1 Input and Output results of Benchmark and Villa Ghia by Metashape	50
Table 6.2. The overview of the data generated by Metashape in these two case studies.....	51
Table 6. 3 Camera Location Error of Metashape Models	52
Table 6. 4 Ground Control Points error of Benchmark and Villa Ghia generated by Metashape	53
Table 6. 5 The value of Ground resolution, projections and reprojection error of Metashape models.....	54
Table 6. 6 The initial data obtained for the Benchmark case study with the Zenmuse P1 sensor.	56
Table 6. 7 The enabled images acquired for the Benchmark case study with the Zenmuse P1 sensor.	56
Table 6. 8 Error values after GCPs imported model of the Zenmuse P1 sensor.....	56
Table 6. 9 The initial data obtained for the Benchmark case study with the Phantom 4 RTK sensor.	62
Table 6. 10 The enabled images acquired for the Benchmark case study with the Phantom 4 RTK sensor.	62
Table 6. 11 The error values after GCPs imported model of the Zenmuse Phantom 4 RTK sensor.	62
Table 6. 12 the initial data obtained for the Benchmark case study with the Zenmuse L1 sensor.	65
Table 6. 13 The enabled images acquired for the Benchmark case study with the Zenmuse L1 sensor. ...	65
Table 6. 14 The error values after GCPs imported model of the Zenmuse L1 sensor.	65
Table 6. 15 GCPs value of the P1 sensor in the Villa Ghia case study created by Metashape	67
Table 6. 16 GCPs value of the P1 sensor in the Villa Ghia case study created by Reality Capture	71
Table 6. 17 GCPs value of the Zenmuse L1 sensor in the Villa Ghia case study created by Metashape ...	74
Table 6. 18 GCPs value of the L1 sensor in the Villa Ghia case study created by Reality Capture	76
Table 6. 19 GCPs value of the Phantom 4 RTK sensor in the Villa Ghia case study created by Metashape	77
Table 6. 20 GCPs value of the Phantom sensor in the Villa Ghia case study created by Reality Capture .	79
Table 6. 21 The models' Surface Density Analysis generated by CloudCompare	85
Table 6. 22 The Volume Density analysis of three different sensors generated in two different software.	85
Table 7. 1 Storage size of the models	95

Abstract

The use of low-cost UAVs (Uncrewed Aerial Vehicles) for documenting and creating 3D models of archaeological and architectural sites as well as geographical areas is becoming increasingly popular. As this technology has become more widespread, the need to test the precision of the acquired data, the accuracy of the models, and the level of detail of the final products has also become vital. This thesis focuses on the contribution of UAV Photogrammetry for 3D Documentation by performing an accuracy evaluation of the employed platforms using the EuroSDR Benchmark and Villa Ghia test sites. The first chapters of this thesis briefly report the history, application areas, and fundamental principles of photogrammetry and UAV photogrammetry. The following sections focus on the selected case studies, drones and camera models, and post-processing methods in software. The methodological framework of this work was defined based on the data made available from the EuroSDR RPAS Benchmark (Peppas et al., 2022). The benchmark is divided into three separate phases and the case study is represented by the Wards Hill Quarry in Northumberland, U.K. As will be better detailed, the three subsequent phases of data release are organized as raw data only, processing with GNSS (Global Navigation Satellite System) base station data, processing with GNSS base station data and GCPs (Ground Control Points). The distributed data were processed following a photogrammetric approach in two different software; accuracy was then evaluated for all the different steps and finally, 3D models, DEM (Digital Elevation Model), and Orthoprojections were created. The accuracy and precision of these three models were tested with Agisoft Metashape. Afterward, the methodological approach set up with the benchmark data was used in a new survey carried out in Villa Ghia, Veneria Reale Italy. Data were recorded with the same sensors used in the Benchmark (DJI Zenmuse P1, DJI Zenmuse L1, and DJI Phantom 4 RTK camera), and different metric products (sparse cloud, dense cloud, mesh with texture, DEM, and Orthoprojections) were created using again two different software (Agisoft Metashape and Reality Capture). Finally, the accuracy of the processing and errors of the different datasets were analyzed and compared. Afterward, the open-source software CloudCompare was used to evaluate the accuracy of the generated 3D models based on Cloud-to-Cloud (C2C) distance and density analyses. This operation allowed us to assess the accuracy and level of details of the 3D models from a metrical and geometrical point of view. The final part of this work is then dedicated to a discussion of the different tested approaches, along with the achieved results to evaluate the results of UAVs photogrammetry in different operative scenarios related to the documentation of architectural built heritage, considering the pros and cons of this technique.

Abbreviations

µm – Micrometer

2D - 2 Dimensional

3D - 3 Dimensional

BA – Bundle Adjustment

C2C – Cloud-to-cloud

CCD - Charge-coupled device

CP - Check Points

DEM - Digital Elevation Model

DG - Direct Georeferencing

DSM - Digital Surface Model

DSS- Decision Support System

DTM - Digital Terrain Model

EPSG - European Petroleum Survey Group (Geodetic Parameter Dataset)

GCP - Ground Control Point

GCS - Ground Control Station

GIS - Geographic Information System

GNSS - Global Navigation Satellite System

GPS - Global Positioning System

GSD - Ground Sampling Distance

GSM - Global System for Mobile communications

LiDAR - Light Detection and Ranging

Laser-DSM - Digital Surface Model generated out of Laser data.

LSS – Laser Scanning System

MSS - Multispectral Scanner

ROA - Remotely Operated Aircraft

RMSE - Root Mean Square Error

RPA - Remotely Piloted Aircraft

RPV - Remotely Piloted Vehicle

RTK – Real-Time Kinematics

SAT-PP - Satellite Image Precision Processing

SIFT - Scale Invariant Feature Transform

SLR camera - Single-lens reflex camera

UA - Uncrewed Aircraft

UAS - Uncrewed Aerial System consists of an Uncrewed Aircraft (UA), a Control System (CS) - usually a Ground Control System (GCS) - and a communications data link between the UA and the CS.

UAV - Uncrewed Aerial Vehicle

UTM - Universal Transverse Mercator

UV - Uncrewed Vehicle

UVS - Uncrewed Vehicle System

VP- Vision Positioning

WGS - World Geodetic System

1. Introduction

The contribution of Uncrewed Aerial Vehicles (UAVs) highly increases and occupy places for new photogrammetry applications in the market each passing day. Acquiring and using UAVs has become much easier with the range of budget-friendly drone options, ease of use for their software and hardware, and their adaptivity for passive and active remote sensing applications. The use of drones is spreading worldwide to different disciplines such as agriculture, archaeology, mining engineering, aerospace and automotive industry, and medicine with various purposes (Kugler L. 2019; Luhman et al., 2011). Drones are mainly used in aerial photogrammetry and photogrammetry applications, except for disciplines such as medicine, construction industry, logistics, agriculture, infrastructure, safety & security, the automotive industry, and biomimetics.

For creating photogrammetric documentation, UAVs came into use and were integrated with traditional photogrammetry to obtain accurate and detailed three-dimensional models. In the Computer Vision (CV) domain, different software have developed algorithms to transfer and process the acquired data from drones by means of computers (Pepe; Costantino 2020). Additionally, for alternative digital remote sensing technologies like LIDAR (Light Detection and Ranging), UAV creates a stable platform for setup long enough acquisition to acquire data at the desired resolution (Habib et al. 2004). Using this kind of technology in architecture, for example, allows the creation of bird's eye perspectives of cultural heritage sites and their environment in a highly detailed way, which helps to emphasize the situation of the architectural site and the context surrounding it. Low altitude photogrammetric mapping technique is used for architectural sites to acquire detailed and accurate three-dimensional models from the site. (Zhang et al. 2011).

It is possible to obtain different metric products with photogrammetric processing. For example, Digital Elevation Model can be generated from the acquired images in the survey because these images contain an exact geographical position of the image, and it allows aligning the images correctly and generating the 3D model precisely. The development of this technology helps us to facilitate the use of the photogrammetric vehicles, and low budget, it brought a new dimension to the research about geomatics and architectural heritage and allowed us to analyze

cultural heritage sites in all aspects deeply, which offered a low-cost and time-saving alternative to the traditional photogrammetry and other surveying techniques.

This thesis is divided into two main parts. The first part is dedicated to theoretically exploring, learning, and analyzing the photogrammetric processes from data acquired and distributed in the Benchmark case study by Newcastle Geospatial Engineering in Northumberland, U.K. This case study offers different sensor data, which helps understand different models generated from different techniques and quality. The benchmark also focuses on three data analysis phases to detect the error and understand the working parameters of Ground Control Points (GCPs) coordinates for each phase. After the Benchmark case study was examined, a practical case study was needed that included all the steps of the photogrammetric pipeline on an architectural case. Data acquisition for the second case study in Politecnico di Torino using the same camera sensor of the EuroSDR Benchmark. The Villa Ghia case study allows us to perfectly analyze all around the site and error deviations because of a set of Ground Control Points measured with traditional topographic techniques. Moreover, Villa Ghia is an architectural site composed of different buildings and structures, unlike the benchmark data, which allows to better analyze the sensors' performances on this type of heritage. The second part of this study evaluates in an architectural context and discusses this type of application's feasibility.

The Villa Ghia survey focused on using different software for documentation on the architectural site and comparing the results obtained. The presence of GCPs in all models allowed accurate results.

This thesis investigates the accuracy results of models acquired by UAV photogrammetry and evaluates the time, labor, and cost spent in this process. The study primarily aims to use the UAV photogrammetry techniques in architectural heritage sites to obtain information needed to create Orthoprojection, 3D models and other metric products. With the use of UAVs, we aimed to take aerial images of architectural heritage sites, process these images, validate their accuracy, and turn them into 3D models.

Chapter 2 contains definitions related to photogrammetry such as geomatics, history of photogrammetry, working principles and methods, features of parameters, application areas, and evolution of sensors used. Chapter 3 explains the site description of both Benchmark and Villa

Ghia and indicates the test sites' locations, historical backgrounds, and the planimetry of existing buildings to estimate the area's characteristics.

Chapter 4 analyzes the data acquisition process for these two case studies and what procedures were followed to acquire data, details of image acquisition features of the sites, information about the surveyed area, used camera sensors, and their properties as a table to compare them with each other.

Chapter 5 reports the data processing workflow phases necessary to obtain a lower margin of error and more precise results in models. To analyze data, Reality Capture 1.2 (Reality Scan, 2022) and Agisoft Metashape 1.8.4 (Agisoft LLC, 2019) software are used. All the steps explain both software's workflow and its parameters. After processing the data, Digital Elevation Models and Orthoprojections are created respectively. At the end of the chapter, there is a cloud-to-cloud distance analysis between each sensor to comprehend the difference between them.

Chapter 6 contains the results of the error deviations of Benchmark and Villa Ghia and these results' comparisons.

Chapter 7 includes the discussion of the limitation of this study during the photogrammetric processing such as time, data size, and access, brief about the further research, and conclusion of thesis.

2. Methodology

2.1. Geomatics

The term "geomatics" refers to a comprehensive, interdisciplinary approach using selected tools and techniques to collect, integrate, manage, analyze, and disseminate digital and georeferenced spatial data. The novelty of this term is that it can georeference any geographical element of the Earth's surface. Geographical data, whether the size of an object or its properties, has been transformed by expert systems into information that can be used for various applications (Gomasasca, 2014) .

Geomatics consists of many disciplines working together to identify, collect, and display large amounts of data to generate different types of information. These disciplines are computer science, geodesy, cartography, photogrammetry, remote sensing, global positioning system, laser scanning system, geographic information system, and ontology. Computer science, which investigates the theoretical and algorithmic foundations of computers and computing, as well as their uses for processing information. Geodesy concerns the Earth's dimension and shape and identifies certain positions of points on the ground as a variation of its gravitational field (The geoid and the ellipsoid) (Gomasasca, 2014). Cartography creates a map of the Earth's surface. This map is based on the precise definitions of the surface's shape, size, and features. Photogrammetry reconstructs the shape a feature of an object by processing photographic images. Remote Sensing is the method of identifying and projecting a terrain's physical features at a distance by measuring reflected and emitted radiation. The Global Positioning System (GPS) determines the latitude and longitude of a receiver on Earth by using satellites, computers, and receivers. This is accomplished by estimating the timing difference between signals from different satellites. A laser scanning system (LSS) creates a 3D image of an object or surface using a laser source that emits radiation events at optical frequencies in the electromagnetic spectrum and a sensor that receives radiative backscatter from the detected (Gomasasca, 2014) . A geographic information system (GIS) can be described as a decision support system for collecting, organizing, managing, analyzing, and visualizing spatial data (Duckham et al. 2003). The decision support system (DSS) is a computer-based information system that assists organizations and business decision-making services. DSSs assist in making choices that may be unplanned and difficult to predict in advance at the management, operations, and planning levels

of an organization. Ontology is a data model in computer science that projects a domain by detailing the objects that comprise and detecting the semantic connections between them.

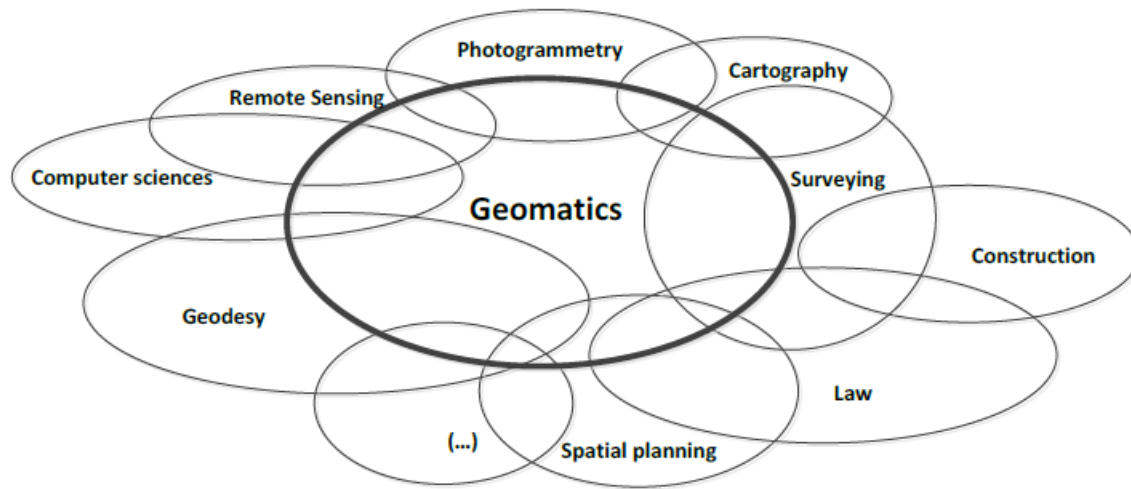


Figure 2. 1 Relationship between the elements of geomatics (De Wulf et al. 2014)

2.2. Definition and History of Photogrammetry

Photogrammetry is a science based on accurately and precisely measuring the properties of surfaces and objects without the need for contact and the acquisition of information. (Schenk, 2005). The word photogrammetry is derived from a combination of the ancient Greek words "photo" (light), "gramma" (drawn), and "metria" (measurement). The science of photogrammetry can record, measure, and evaluate images and the electromagnetic energies they emit. In general, photogrammetry is a technique of measuring the 2- or 3-dimensional coordinates and positions of objects on the Earth through photographs.

Photogrammetry's history dates to 1827. However, the exact date of the beginning of photogrammetry is accepted as the 1850s. This process was started by Daguerre and Niepce, who invented photography (Wolf et al. 2014). The history of photogrammetry can be broken down into 4 phases according to technological development. The first stage, photography, and plane tables between 1850-1900, the second stage, Stereoplotters and Airplane between 1901-1950, the third stage, Computers and Mathematical Model, between 1951-1971, and the final stage Digital and Computer Vision continues from 1972 to this day (Foster & Halbstein, 2014) . Photography and plan table analyses were enhanced by capturing the images from high rooftops, hills, or balloons, and then, linear perspective, created with simple math, was able to manually compare

known heights on top of the acquired images to obtain the additional height of objects within the image. In 1859, Gaspard Tournachon took the first aerial oblique photograph of a small village in Paris. It is widely accepted that the observation of the world and the remote sensing era began with this image (Kumar et al., 2004). Interestingly, the term "photogrammetry" was coined by Meydenbauer in 1893, thirty-five years after the first aerial photograph was taken (Awange et al. 2013).

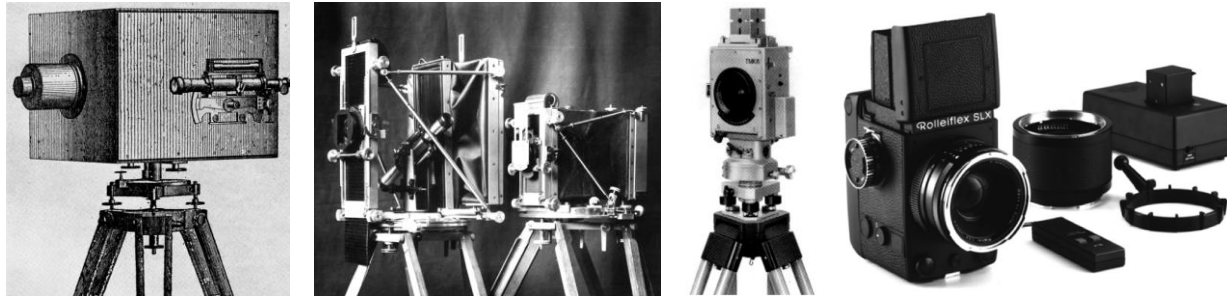


Figure 2. 2 Photogrammetric camera development from the 1850s to the 1980s (Luhman et al., 2011) .

The second phase contains an earlier period of aerial photogrammetry. Stereoplotters are the stereoscopic images edited by making measurements of an object with overlapping two images of the same object by optically calibrating and combining with technology. There were several different devices to compute the precise position of images, such as floating marks, stereo autography, serial-photo aerial cameras, Etc. In 1909 Wilbur Wright took the first aerial photo from an aircraft around Centocelli, Rome (Kingslake, 1942).

The third phase of photogrammetry represents the Computers and Mathematical Models. The accuracy of the results has increased noticeably with the integration of computer systems capable of rapid mathematical processing into the photogrammetric devices developed in stereo plotting and photography. Since the "algorithms for orientation and triangulation" have been developed in computer systems, both the accuracy of the results and the processing speed have been greatly accelerated (Foster & Halbstein, 2014) .

For the last phase of photogrammetric development, physical plotting devices such as stereo plotters used in previous technology have been replaced by light and range sensing (LIDAR) remote sensing technology, which uses lasers instead of analytical stereo images to map depth, distance, and location information. The first readable images of Earth from orbit were recorded from Landsat, sent by NASA in 1972. After Landsat's launch, the first MSS

images were obtained with high clarity of the landscape and agricultural area (Williams & Carter, 1976). Photogrammetry methods have revolutionized thanks to advances in digital imaging between the 1960s and 1980s; full-range commercial cameras were introduced in the 1990s (Luhman et al., 2011) . Digital photogrammetry can be classified into two sub-sections, aerial photogrammetry, and terrestrial photogrammetry, depending on the location of the photographs taken (Luhman et al., 2011).

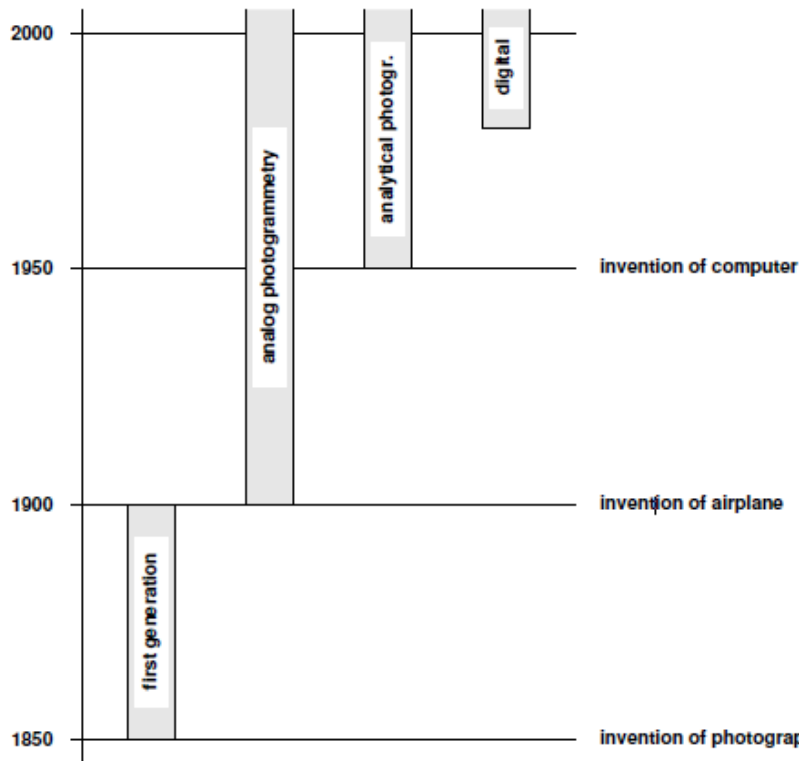


Figure 2. 3 Major photogrammetric phases as a result of technological innovations. (Schenk, 2005)

2.3. Terrestrial Photogrammetry

Terrestrial photogrammetry deals with images obtained with cameras positioned on the Earth. Depending on the user's needs or the topography, the cameras can be mounted on tripods, fixed to specific structures, or hand-held. Close-range photogrammetry generally considers the survey field distance up to approximately 300 meters. In terrestrial photography, cameras are capable of direct measurement, similar to GNSS control in aerial photogrammetry, as they are located in positions the user can reach and edit as needed. The exterior orientation of the image obtained in some terrestrial cameras can be calculated because its angular direction and fixed

value parameters are adjustable. External orientation parameters can be used as a control criterion in terrestrial photogrammetry as they wholly or partially change the control point positioning of the object space according to the optimum scenario (Wolf et al. 2014).

Since terrestrial photogrammetry can only be done with photographs taken from the ground, some details cannot be determined easily. When the calibrations and adjustments have been set for aerial photogrammetry, the image acquisition is taken high above the ground, which allows the detection of most of the details of topography. For this reason, aerial images have an important place in the development of photogrammetry. Aerial photogrammetry emerged with the development of motorized aircrafts, which became widespread with the World War I. Especially after the technological developments in the 90s, the use of individual commercial aircraft and digital cameras, and the increase in their use in photogrammetry, the use of UAVs in digital photogrammetry has paved the way for innovations. Thus, UAV photogrammetry, a sub-study field of digital photogrammetry, was constituted.



Figure 2. 4 Aerial surveying technique by plane from 20s and **Figure 2. 5** model helicopter aerial survey from 80s (The brownstone detectives, 2020, Wester-Ebbinghaus, 1980).

2.4. Definition of UAV and UAV Photogrammetry.

UAVs are motorized aircrafts that can be guided by remote control without the need for a pilot and can be used for repetitive operations as long as they are charged. UAVs (Eisenbeiss, 2009) can be used as remote-controlled, autonomous, semi-autonomous, or combinations of all these, or can be used as a combination of all these options when needed, depending on the situation.

The term UAV is used in fields such as photogrammetry and Remote Sensing in engineering and architecture, as well as in branches of science such as artificial intelligence and

robotics. The term UAV can also be used with names such as Remotely Piloted Vehicle (RPV), Remotely Operated Aircraft (ROA), Remote Controlled (RC) Helicopter, Uncrewed Vehicle Systems (UVS) and Model Helicopter.

UAVs were firstly developed for military purposes and applications (Bone and Bolkcom, 2004). They have been used for military surveillance, espionage, reconnaissance of enemy territory, and information gathering. Przybilla and Wester-Ebbinghaus (1979) performed the first experiments in geomatics applications. In the past, airplanes were used for this purpose. However, they have been gradually replaced by UAVs. This is because, in recent years, the use of UAVs has become widespread with the development of technology, the ease of access to the developed technology, the reduction of error margins, and faster and easier processing of data in the computer environment. The advantages of the technology are often tied to making operations quicker, cheaper, or safer. The benefits of the UAV-assisted operations are:

- Safety by giving a chance to obtain various data with the aerial survey methods without endangering the labors on dangerous
- Costs are associated with lowering data collecting operations costs
- Flexibility, related to carrying out operations as needed or on time
- The quickness that allows obtaining real-time data with the usage of adaptive technology
- Productivity with time-saving due to a high level of automation-driven technology
- The frequency that allows using, monitoring, and tracking of the iterative progress of work during the survey when it can be performed only limited times with the traditional methods

speed for the survey. They are less common in survey applications than Multicopters (Jackson, 2021).



Figure 2. 7 Quadcopter

Image from: <https://www.dji.com/>



Figure 2. 8 Fixed-Wing UAV

Image from: <https://www.unmannedsystemstechnology.com/>

Besides the advantages of using UAVs, there are also some disadvantages. Depending on the changing weather conditions (wind, rain, etc.), in some cases, it may be observed that the images taken from the drones are unstable depending on weather conditions, and the desired data cannot be collected. In addition, high-resolution data may not be collected depending on the price and features of the device used, and some information may not be obtained because the devices cannot be flown from the required heights depending on the size and engine power. Sun reflection and acquired data from the wrong angle with the sensor cause distortions in generated orthophotos and DSM/DTMs. Furthermore, because machines cannot think and solve problems like humans, it can be challenging to solve unusual problems when they arise.



Figure 2. 9 Model airplane Firma Hegi, Przybilla 1979.

2.5. Digital Photogrammetry

Digital photogrammetry concerns to produce the 3D information such as digital images or pictures from 2D data environments. It includes software programs and hardware that uses digital images as input and may carry out all photogrammetric obligations with interrogative or semi/fully automatic methods.

Digital photogrammetry ensures that the stereo images recorded in digital form are processed entirely in the computer environment, and the orientation and evaluation processes are performed semi-automatically or automatically. The interest in digital photogrammetry has multiplied because of the excessive resolution of the images, the preferred development of the photograph, and the ability to attain many colors within the computer environment. With the improvement of technology, the formation of rapid processors and compelling memories has caused the spread of digital photogrammetry. Digital images, which form the basis of digital photogrammetry, offer integrity with hardware and software program base, and form a common area of use for collecting and analyzing data.

2.5.1 Evolution of Camera Sensors

After the invention of photography in the early 19th century, aerial photography began to be used in the mid-19th century by thrill-seekers who launched cameras into the flight

instruments such as balloons, kites, rockets, etc. The first successful aerial photography was taken in 1858 by Gaspar Félix Tournachon (also known as) outside Paris with a hot air balloon. Afterward, with the World Wars and military developments, countries realized the potential of aerial photogrammetry, and a rapid development process was undertaken to advance in the field, especially for surveillance and espionage. In the 1990s, when drone technologies began to be used for civilian purposes, with the launched cameras on drones, a much low-cost and faster alternative than other aircraft emerged for aerial measurements and specific studies.

UAV technology has advanced quickly due to lower research and development costs and operational costs. Simultaneously, the precision of UAV photogrammetry application has increased and provided opportunities to obtain vehicles that provide high-definition data with low secondary risks. The use of UAVs has rapidly diffused in multiple different sectors such as surface topography, topographic analysis of prone regions, analysis of erosion, silting and movement of riverbeds over time, design of drainage systems for both urban flooding purposes, and terrace farming in mountainous areas. Because the advanced camera sensors and drone features provide an opportunity to use in several different applications such as incline of topography, different levels of altitude, the density of the vegetation, different climate conditions, and flight time duration. To collect data in UAVs, different camera sensors can be equipped as a payload. A laser scanner, one of the sensor types used in UAVs, is a good choice for measuring large areas from high altitudes and converting these results into point clouds containing density and return numbers. Cameras, another option, are capable of capturing images in a broad electromagnetic spectrum. Thermal cameras can record infrared and near-infrared images to create spectral compositions. Thus, RGB cameras are sufficient and cost-effective to produce photogrammetric stages such as Dense Cloud, DEM, and Orthoprojection in digital photogrammetry. CCD or CMOS sensors provide the conversion of the spectrum wave into the visible range. The resolution of the UAV data also varies according to the internal parts and ancillary equipment used.

2.5.2 Metric Cameras:

For a camera to be considered metric, its lens must be suitable for modeling through parameters whose distortion properties are repeatable, stable, and can be accurately predicted by the photogrammetric calibration process. It is used to make high-resolution aerial photography but is very expensive compared to non-metric cameras (Liu et al., 2012).

2.5.3 Non-Metric Cameras:

Non-metric cameras are commonly used digital cameras today. Photogrammetrically, digital cameras are called non-metric cameras because the internal orientation elements are partially or entirely unknown, and there are no framing marks on the image. Compared to metric cameras, it is much lower cost and quick to obtain information. An adequate degree of accuracy can be achieved by using narrow-angle cameras in terrestrial image acquisitions. Because of the low geometric accuracy of non-metric cameras, calibration must be done more frequently compared to metric cameras. Since the use of non-metric cameras was supported by the evolution of CV (Computer Vision), it has given a possibility to perform a self-calibration approach to increase the accuracy.

When using non-metric cameras some parameters need to be modeled via a camera calibration procedure. In the calibration process different parameters are considered:

Focal length: The camera lens' focal length defines the captured area and the angle of the light ray. When focal length increases, image distortion decreases. If the focal length is calibrated, it allows for accurate measurement of an acquired image.

Lens distortion: It occurs when rays inclined to the optical axis come to surfaces with different indices and are refracted differently. The distortion direction is usually towards the center of the acquired image or occurs in an outward direction (Wolf et al. 2014).

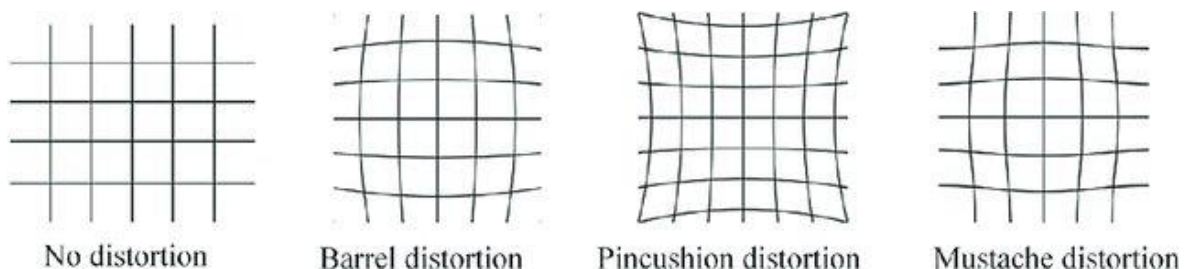


Figure 2. 10 Distortion Types (Pilar Valerga Puerta et al., 2020).

Principal Point: The two-dimensional image represents the three-dimensional image plane through the lens. The principal point is the intersection of the image plane and the camera sensor's line of sight. To obtain a precise result, the lens must be centered on the image sensor.

Radial Coefficient Distortion: The distortions that occur due to the spherical shape of the lens and due to curvature are called radial distortion. It is related to the focal length. Its display in camera calibration covers values between K1 and K4.

Tangential Coefficient Distortion: The distortions caused by the lens components being non-orthogonal and moving away from the optical axis are called tangential distortions. It is displayed between the P1 and P4 values from the camera calibration.

Here are some parameters which are given above about the lens calibration:

f

Focal length measured in pixels.

cx, cy

Principal point coordinates, i.e., coordinates of lens optical axis interception with sensor plane in pixels.

b1, b2

Affinity and Skew (non-orthogonality) transformation coefficients.

k1, k2, k3, k4

Radial distortion coefficients.

p1, p2, p3, p4

Tangential distortion coefficients. (**Agisoft Metashape User Manual Professional Edition, Version 1.5**)

In this phase, all the options (f, cx, cy, b1, b2, k1, k2, k3, p1, p2, p3) have been used for obtaining a good quality result except the k4 and p4 (Agisoft Metashape User Manual, 2019).

2.6. Principles and Fundamentals of Photogrammetry

Photogrammetry deals with image interpretation and computation methods to define its location and surface features from one or more photographs of that object. These methods can be suitable to use if the measurement of an object can be detected from images. The main aim of

photogrammetry measurement is to reconstruct three-dimensional objects with accurate coordinate and geometric properties in a graphical or digital environment (Luhman et al., 2011).

The image coordinate system is determined by the intersection of the x, y, and z axes, with the center point being the reference point. The x-axis and y-axis are collinear in the same plane (x-y plane), with the z-axis being perpendicular to the x-y plane, forming a 3D space in which we can approximate the desired location. Figure 2.5. demonstrates two photographs taken from different angles help to identify the 3D coordinates of point P. In the figure below, f shows the focal length of the camera lens; o1 and o2 illustrate the position of the focal point of the camera lens at the time the photographs were taken. x1 and x2 indicate the direction the UAV was flying at the moment of photography, and the x-axis is determined from the x1 and x2 axes. y1 and y2 are the axes perpendicular to both the UAV flight direction and the z-axis, and the y-axis is determined from the y1 and y2 axes. Point P is present in both photographs and is indicated as p1 and p2. The most crucial point is that the ray of light projecting inside camera 1 and the ray of light projecting inside camera 2 will not intersect at point P on the ground unless there is either the interior orientation inside the cameras that dictates the geometric parameters of the imaging process or good exterior orientation that dictates the precise 3D position for the camera lens' focal point as well as the exact angular orientation of the UAVs carrying the cameras.

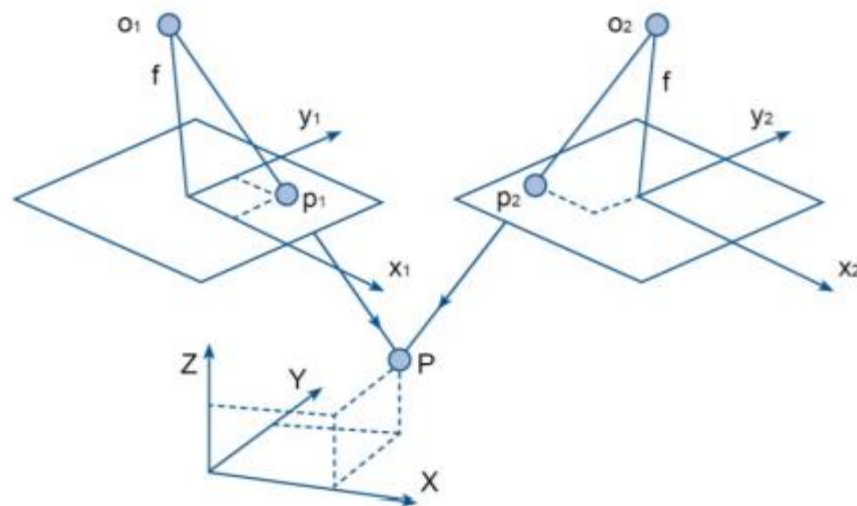


Figure 2. 11 Principles of Photogrammetry the Approximation of 2D measurements on stereo photographs to facilitate 3D mapping of the point on the ground (Osborn et al. 2018)

2.7 Structure from Motion (SfM)

Structure from Motion (SfM) is a photogrammetric image match processing, which reconstructs estimated 3D models with overlapping and offset 2D images taken from different angles of the target in a computer environment.

Traditional photogrammetry reproduces camera calibration parameters and camera poses from ground control points and tie points. Structure from Motion calculates these traditional parameters and a set of sparse 3D points simultaneously (Chiabrando et al. 2015). Moreover, while traditional photogrammetry is based on collinearity equations, SfM works using epipolar geometry. As a difference from traditional survey techniques, among the different methods, SIFT (Scale Invariant Feature Transform) is the most known and commonly used by SfM (Lowe, 2004). SIFT is used to match and align images among themselves, to create a sparse point cloud with the characteristic features of the images, and it makes use of the least square bundle adjustment algorithm for this (Cullen et al. 2018). This repetitive process creates an estimated location between the rotation, internal camera geometry, and external camera position. In this step, control points are optional for reconstructing a sparse cloud model. With the absence of control points, cloud points can still be created, but GCPs allow the georeferencing and scaling of the model and determine more accurate results in photogrammetric processing. Compared to the SfM technique, it requires a longer time and budget for planning and tools for a survey. Therefore, it is not suitable for use in survey processes that require repetition. In contrast, LiDAR enables the identification and filtering of vegetation in the surveyed terrain and the creation of a good terrain model thanks to laser measurement (Mol & Clarke, 2019).

In SfM photogrammetry, although the colors of the points obtained to create DTM can be defined, it cannot automatically identify the vegetation. For this reason, elements that are different from the ground should be classified (Johnson et al. 2014).

2.7.1. Bundle Adjustment

Bundle adjustment (BA) is an improvement technique generally used to enhance the reliability of the data obtained in the traditional photogrammetry and SfM (Kanatani et al. 2011). It has an iterative process and aims to optimize all parameters simultaneously, minimizing a global cost function. It is an essential method for estimating the positions of multiple images in

x, y, and z coordinates and reconstructing matched three-dimensional points. Its purpose is to reconstruct the determined points by specific parameters and minimize the reprojection errors between the estimated and detected points of images (Triggs et al., 2000). Bundle adjustment also concerns defining the order of aerial image acquisition in a survey and detecting the angle of the acquired image to match the slightest error.

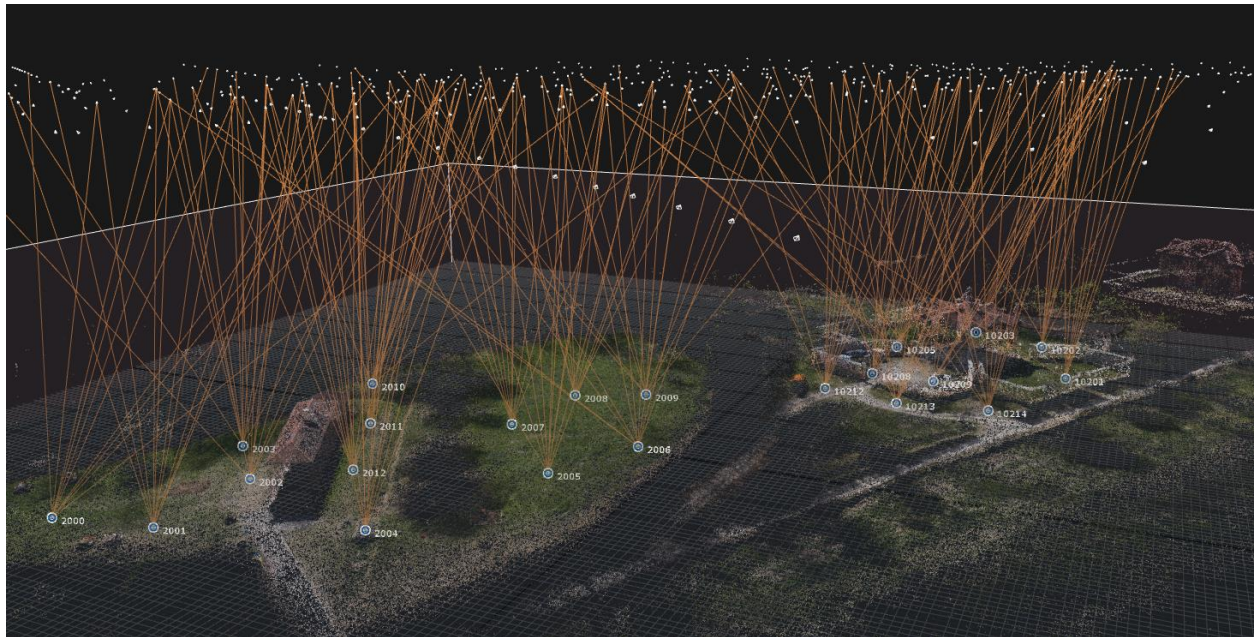


Figure 2. 12 Representation of the demonstration of the bundle-adjustment technique performed by Reality Capture.

This method allows matching different images acquired in the survey with different angles and reconstructing 3D points according to their parameters. Reconstructed points update the estimated position according to the adapted location and recover the reprojection error, which generates more reliable results in the Structure-from-Motion (SfM) technique.

2.8. Application

Photogrammetry is used in many different disciplines dealing with the imaging of objects and the environment. Some of the application areas are:

- **Architectural photogrammetry:** Based on visual data and mathematical coordinates of architectural objects or structures, it covers the creation and processing of models and landforms to document these structures, display, and preserve cultural and historical heritage. With this method, two-dimensional and three-dimensional data of historical

items are obtained, and it helps to create the necessary previews for restoring the surface deterioration and ruins of the buildings.

On the urban scale, with the three-dimensional models, a preview can be created for infrastructure design and creation, emergency plans, land parcellation, and proper urbanization for the future. Close-range photogrammetry is also used in preparing census and statistics about the city, arrangement, and management of green areas, and in studies related to environmental pollution.

- **Archaeological Photogrammetry:** Based on the photogrammetry, it has become possible to monitor collapsed structures, buildings, ancient tombs, shipwrecks, or historical sites more quickly, accurately, and cost-effectively. It has become easier to share the collected data and remotely control the studies globally.
- **Biostereometrics:** Based on analytical geometry principles, it is used to define the human body and its possible post-operative facial changes in three dimensions (S. Berkowitz et al. 1977).

Regardless of its medical application, biodynamic models are created in traffic accidents, and different factors such as speed, vehicle type, and body types can be simulated in the computer environment. An idea can be obtained from the accidents that have occurred.

- **Industrial Photogrammetry:** Photogrammetry is used in industries such as factories, mining, automotive, and aircraft. It is used in the quality control of products in factories to detect possible manufacturing defects.

In the automotive industry, photogrammetry is used in different processes such as the design of vehicle cases, three-dimensional modeling of vehicles and all their intricate parts, robot calibration, optical shape measurement, manufacturing control, and post-manufacturing tests (Luhman et al., 2011).

In the aircraft industry, it is used in the measurement of parabolic antennas, the control of assembly, the modeling of cable routes, and equipment of old aircraft models in CAD.

3. Test Areas

3.1. Benchmark - Wards Hill Quarry



Figure 3. 1 Geolocation of survey site

0 0,02 0,04 0,09 0,14 0,18 Km

The first of the two case study areas, Wards Hill Quarry, is in the county of Northumberland in Northern England. The area is close to the Scotland border, approximately 30 kilometers away. The quarry was used until the 20th century.



Figure 3. 2 Panoramic view of Ward's Hill Quarry. (Figure from <https://geospatialncl.github.io/euroedr-rpas-benchmark>)

The field has an elevation difference due to the stones extracted from the quarry since it is located in the valley and has a natural slope. The quarry was used for limestone mining in the

1920s. Currently, the quarry is privately owned and used as pasture by its owners. The size of the surveyed area is 250 x 350 m, and the topography is lowering 40 m where the limestone is quarried. The ground consists of grass vegetation and shrubs and does not include high vegetation (Peppia et al., 2022).

3.2. Villa Ghia and Ciabòt delle Guardie



Figure 3. 3 Site location of Villa Ghia.

Villa Ghia is now a disused historical building located in La Mandria Park, in the municipality of Venaria Reale, northwest of the Turin city.

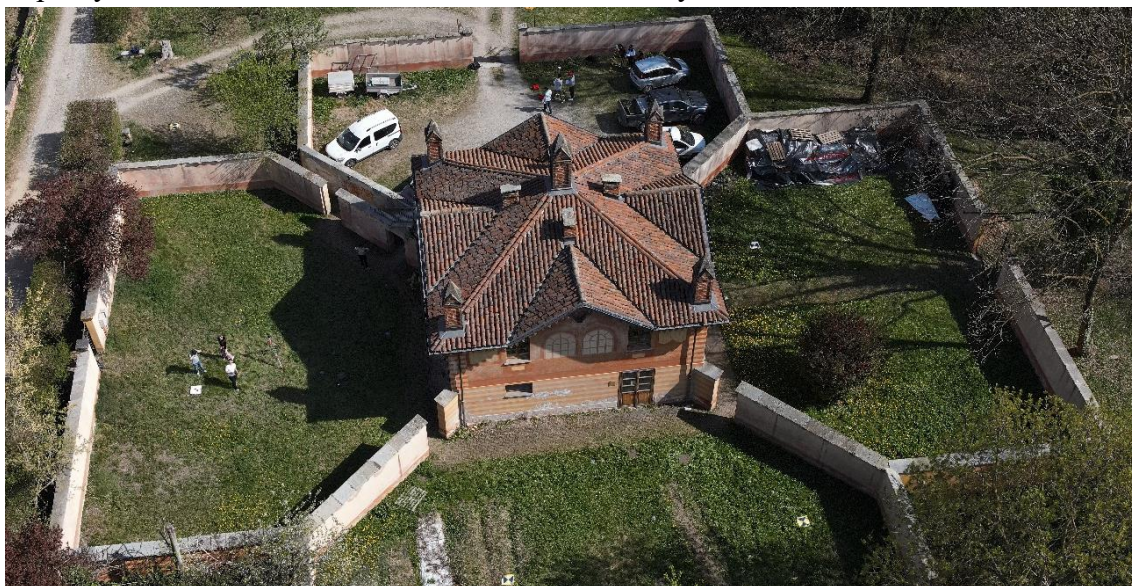


Figure 3. 4 Aerial view of Villa Ghia with its external surrounded walls

Built as a horse-riding station and partially hidden from view by a high boundary wall that also includes the Villetta, it is a complex comprising a square-plan construction developed on two floors above ground with a decidedly projecting roof and cross-shaped pitches and wooden decorations under the eaves and single-story rectangular-shaped stabling with a similar roof.

In the past, the building's ground floor was used as a stable, divided into four individual square rooms. The first floor is served residential purposes and has an external staircase for use.

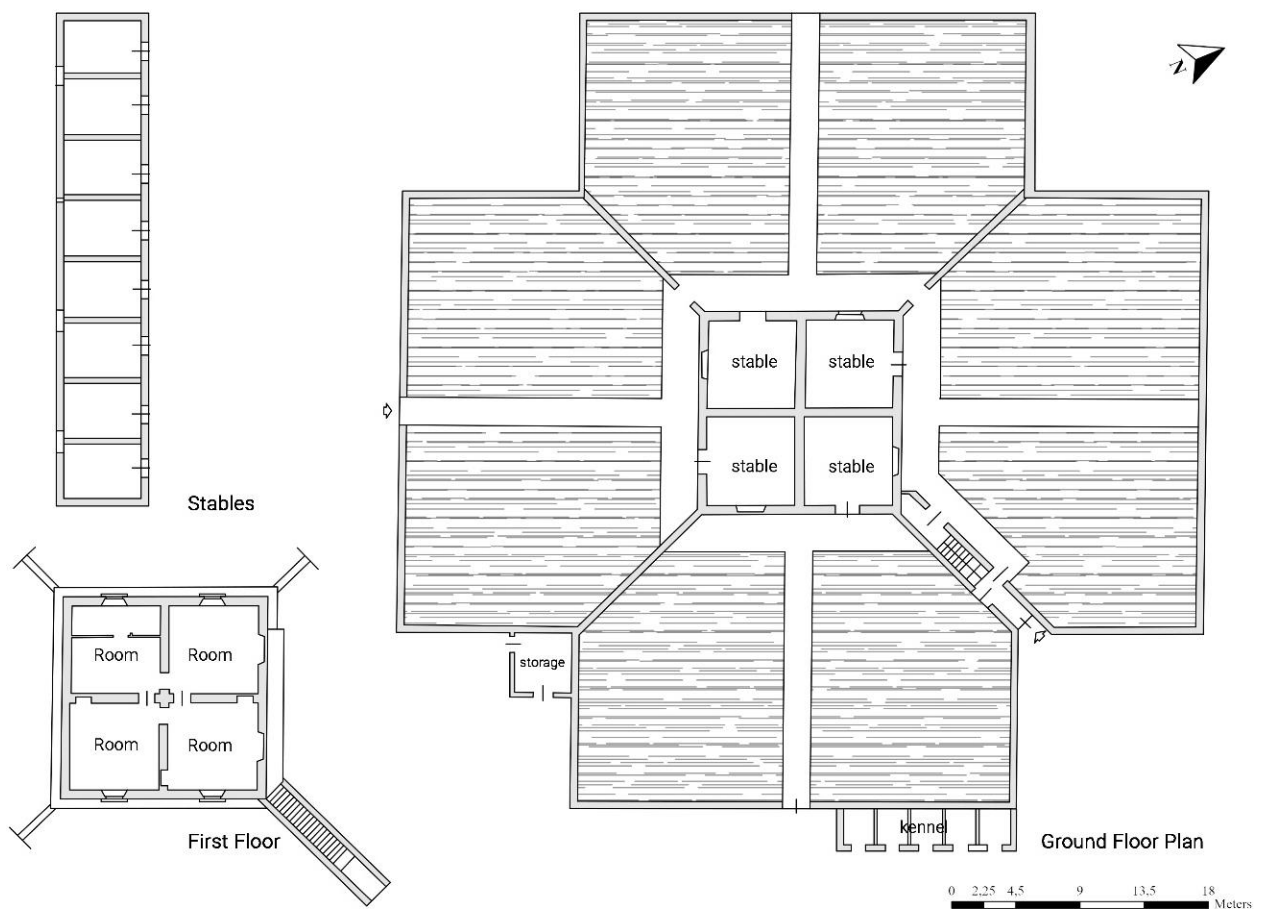


Figure 3. 5 Ground floor and first-floor plans of Villa Ghia

The complex and the stabling have all the façades frescoed with trompe l'oeil as well as the adjacent Villetta. The assembly station is surrounded by a high wall whose course has a characteristic cross shape with internal diagonals, dividing each assembly compartment and different accesses.

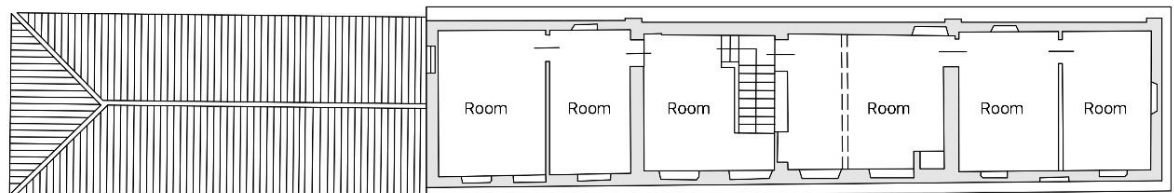
3.3 Ciabòt delle Guardie

Because of its building type, the building is linked with Borgo Castello instead of Villa Ghia.

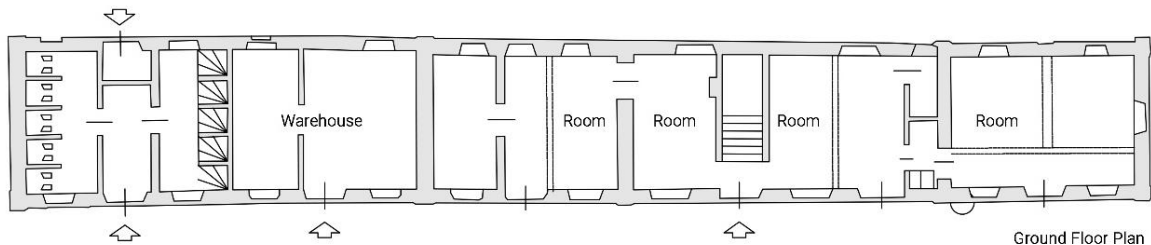


Figure 3. 6 Elevation of the Ciabòt delle Guardie

At the time, conceived as a marquisate, it was constructed with a rectangular plan of simple lines which required the then planned use. Overall, it is divided into two adjacent buildings, one with two floors above ground, the other with one, and both without cellars.



First Floor Plan



Ground Floor Plan



Figure 3. 7 Ground floor plan of the Ciabòt

4. Data Acquisition

4.1. Test Field Details

This chapter will explain the aircraft used in the data acquisition, the sensors equipped, and the methodology applied during the fieldwork.

4.1.1. EUROS DR Benchmark

This thesis' study data includes two different surveys. The first survey contains the examination of a quarry in Morpeth, Northumberland, U.K., carried out by Newcastle Geospatial Engineering. The study was conducted in August 2021.

The surveyed area comprehend 8 Ground Control Points (GCP) and 51 Check Points (CP) as targets. Checkpoints were fixed on boards driven into the ground to make it easier to identify lidar data and avoid errors from ground vegetation. Thus, the height of the ground control points is approximately 15 cm - 45 cm.

The test area is defined using the alphanumeric A to F according to their position and 1 to 8 for each letter label. Three more checkpoints with tag names S1, S2, and S3 have been added to improve accuracy in areas where topography changes. Label names were also sprayed on the grass to avoid mistakes in definitions caused by reflection and some confusion while measuring during the survey.

In this study, DJI ZenMuse P1, DJI ZenMuse L1, and DJI Phantom 4 RTK camera sensors were used for information acquisition. With the DJI Zenmuse P1 sensor, 999 images were obtained with 27 flight lines. In addition, it includes 25 more images taken at a 45° of nadir angle. RTK feature is disabled during flight. Flight mission settings of DJI Zenmuse P1:

- Flight Height: 50m
- Forward Overlap: 80%
- Side Overlay: 70%
- Camera Exposure: Automatic
- Focus: Continuous
- Flight Speed: 5 m/s

3 separate flights were carried out with the DJI Phantom 4 RTK sensor. In these flights, a total of 489 images were obtained, including nadir and oblique images. These three flights' acquisition settings:

First Flight

- nadir plan including 430 images
- 11 parallel flight lines and one cross flight line
- 55 m flying height
- 4.3 m/s aircraft speed
- 80/70 % forward/lateral overlap

Second Flight

- the oblique plan including 38 images
- 3 flight lines over the quarry
- 20° off-nadir angle

Third Flight

- the oblique plan including 21 images
- 2 flight lines over the quarry
- 0° off-nadir angle

254 images were recorded in 13 parallel flights with the DJI Zenmuse L1 sensor. Settings of the captured images:

- Flight Height: 50m
- Overlap: 50%
- Echo Mode: 3
- Flight Speed: 5 m/s
- Calibration Flight: On
- Sampling Rate: 160kHz
- Scanning Mode: Repetitive Scan

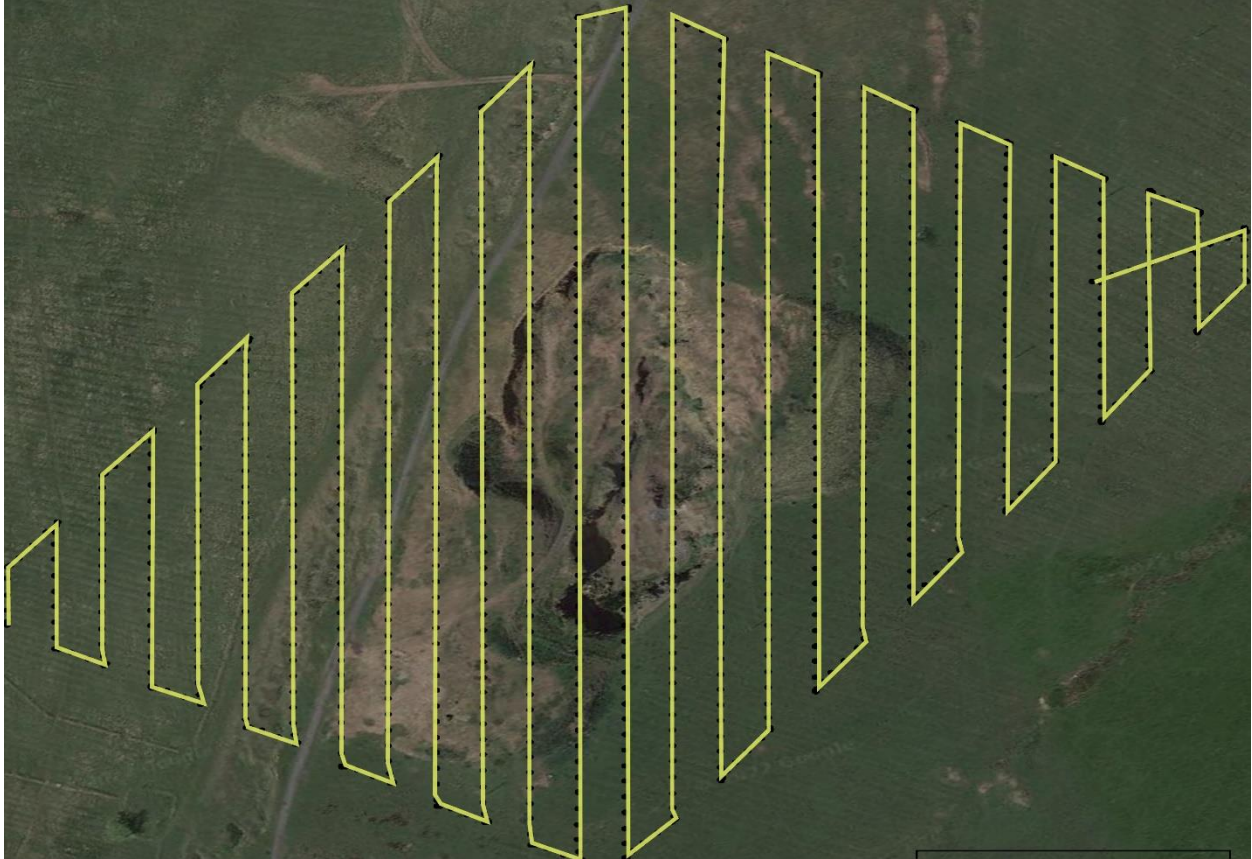


Figure 4. 1 Flight mission path of the Benchmark test site.

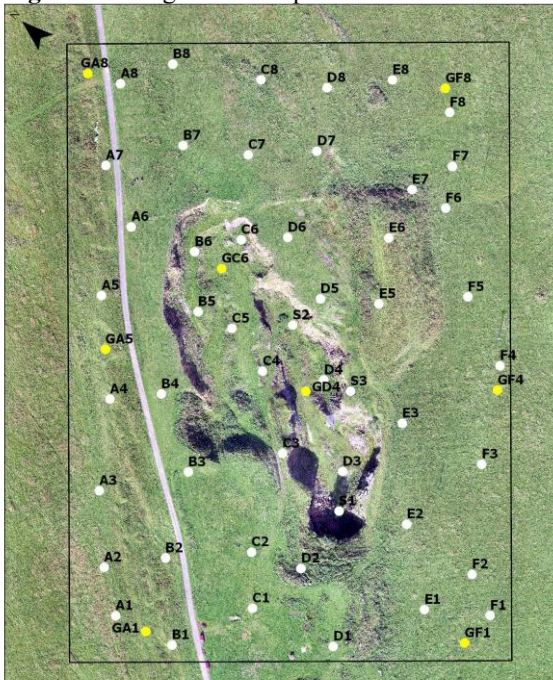


Figure 4. 2 ICP and GCP target location of Benchmark.



Figure 4. 3 CP label sprayed for identification

4.1.2. Villa Ghia

The second survey was performed on 11.04.22 by members of the Politecnico di Torino Geomatics Laboratory during the course of Drones for territorial and architectural survey.

In the Villa Ghia study, 22 Ground Control Points (GCPs) with labels between 2000 and 10200 and 10214 were placed on the ground. Ground Control Points have been placed in the open area around Villa Ghia and Ciabòt delle Guardie to avoid being affected by low-level vegetation and trees.

Likewise, the DJI ZenMuse P1, DJI ZenMuse L1, and DJI Phantom 4 RTK camera sensors used in the Benchmark were used in the Villa Ghia study.



Figure 4. 4 Flight Mission Path of the Villa Ghia test site.

4.2. UAV and Camera Sensors

Drones are powered aircraft that work with their onboard sensors and GNSS, can be remotely controlled using flight plans, or fly autonomously by software in their internal systems. Today, drones are highly preferred because they do not need a pilot, are low in cost, can be controlled remotely, and have higher maneuverability than other aircraft. On the other hand, drones also have disadvantages such as short battery life, being affected by in case of adverse weather, and start-up costs for acquiring the devices and trained pilots.

Drones must be equipped with specific technology for the data can be processed optimally in image acquisition with UAV systems. For example, for the camera sensors to obtain high-accuracy images, they must be launched into the gimbal system, which allows them to absorb the motion caused by external factors and move in all three axes.

The flight controller is also a substantial piece of equipment that can be considered the drone's control center. It processes the inputs transmitted from the GNSS module, remote control, obstacle detection sensor, and compass, ensuring that the engine receives images in the best conditions and its position remains stable. Depending on the field of use, 3D terrestrial scanning systems or lidar scanning sensors that can collect infrared, thermal, multispectral, or RGB images can be preferred. These sensors are usually more expensive than drones themselves.

Considerations when choosing a drone are cost, sensor quality, coverage area, flight time, weight, and size. **Table 4.1.** below compares the DJI Matrice 300 and DJI Phantom 4 RTK drones used in these case studies.



Figure 4. 4 DJI Matrice 300 RTK (Figure from <https://www.ingeniovirtual.com>)

Table 4. 1 comparison between the DJI Matrice 300 and Phantom 4 RTK drones used in these case studies.

	DJI Matrice 300 RTK	DJI Phantom 4 RTK
Dimensions	810×670×430 mm	350 mm
Operating Temperatures	-20 to 40 °C	0-40 °C
Max Flight Time	55 min	30 min
Flight Ceiling	5000 m	6000 m
Max Takeoff Weight	9 kg	1.4 kg
Maximum Flight Range	Up to 15 km	Up to 7 km
Maximum Operating Distance	8 km	6.92 km
Hovering Accuracy	±0.3' / 0.09 m Vertical with V.P. ±1.6' / 0.49 m Vertical with GNSS ±0.3' / 0.09 m Vertical with RTK ±1.0' / 0.30 m Horizontal with V.P. ±4.9' / 1.49 m Horizontal with GNSS ±0.3' / 0.09 m Horizontal with RTK	±0.33' / 0.1 m Vertical with V.P. ±1.64' / 0.5 m Vertical with GNSS ±0.33' / 0.1 m Vertical with RTK ±0.98' / 0.3 m Horizontal with V.P. ±4.92' / 1.5 m Horizontal with GNSS ±0.33' / 0.1 m Horizontal with RTK
GNSS Support	GNSS, GLONASS, BeiDou, Galileo	GNSS, GLONASS



Figure 4. 5 DJI Zenmuse P1
(Figure from <https://www.dji.com>)



Figure 4. 6 DJI Zenmuse L1
(Figure from <https://www.dji.com>)



Figure 4. 7 DJI Phantom 4 RTK
(Figure from <https://www.dji.com>)

Table 4. 2 the comparison of the DJI ZenMuse P1, DJI Phantom 4 RTK, and DJI ZenMuse L1 camera sensors used in Benchmark and Villa Ghia surveys.

	DJI Zenmuse P1	DJI Zenmuse L1	DJI Phantom 4 RTK
Dimensions (mm)	198×166×129	152×110×169	Diagonal distance 350
Camera resolution	45 MP	20MP	20MP
Compatible aircraft	DJI Matrice 300 RTK	DJI Matrice 300 RTK	DJI Phantom 4 RTK
Operating temperature range	-20° to 50° C	-20° to 50° C	0° to 40°C
Max Resolution	8192×5460	5472×3078	5472×3648
Focal Length (mm)	35mm	8.8	8.8
Pixel Size (µm)	4.39 x 4.39	2.41 x 2.41	2.41 x 2.41

The data from the Benchmark were obtained with two different drones. First the DJI Matrice 300 drone was used with DJI Zenmuse P1 and DJI Zenmuse L1 sensors. After that, The DJI Phantom 4 RTK drone, whose camera and drone were designed together, was used. The focal length of the DJI Zenmuse P1 sensor used in the survey was 35 mm, and the images were recorded at a resolution of 8192 x 5460 pixels. The pixel size is 4.39 x 4.39 μm , the flight height is approximately 56.8 meters, and a total of 999 images were captured during the flight. The camera model of DJI Zenmuse L1, another sensor used in the survey, is the EP800. The focal length of the sensor is 8.8 mm, and the images were recorded with a resolution of 5472 x 3648 pixels. The pixel size is 2.41 x 2.41 μm , and the flight altitude is about 62.4 m. A total of 254 images were captured during the flight. The last sensor used in the survey is the DJI Phantom 4 RTK with the FC6310R camera model. The focal length, pixel size, and pixel resolution of the sensor are the same as the L1 sensor, the focal length is 8.8 mm, and the images were recorded with a resolution of 5472 x 3648 pixels. The pixel size is 2.41 x 2.41 μm , and the flight altitude is about 60.4 m. A total of 489 images were captured during the flight.

5. Data Processing

For the data processing stage, the acquired images during the survey were processed in different software for comparison. 3D models were processed and created with different parameters in the software. The error values of the Control Points and Ground Control Points, which are used while creating the model and increasing the precision, are estimated. Then, it was imported to CloudCompare software to compute the distance between the points and the density of the models. Agisoft Metashape was applied to process the data taken from an aerial survey with drones. Reality Capture was used for processing the acquired aerial photogrammetric survey data. CloudCompare for computing the cloud-to-cloud distance dually between DJI Zenmuse P1, DJI Zenmuse L1, and DJI Phantom 4 RTK sensors and applied separately for the generated clouds of the Agisoft Metashape and the Reality Capture. For the last step, the cloud density of each sensor and software are compared individually.

5.1. Image Orientation

This section will discuss how data was processed in Metashape and Reality Capture. First, the images collected from drones during the survey need to be inserted into the software to begin analyzing images. Those images sometimes include more than one folder because every flight includes a different record folder inside the sensor.



Figure 5. 1 – Image orientation of model in Metashape

Alignment provides a three-dimensional projection of the site by combining and reconstructing all the images among themselves. To define tie points in software, every image has key points. Key points can be described as determining characteristic points in images, and tie points are the key points that can be defined in two or more images to calculate a three-dimensional position in a computer program. For aligning phase, the Key Point's limit is 40000, and the limit of the Tie Point is 4000 (Key Points Meaning, n.d.). Alignment parameters in the software can be changed according to the desired quality of the image. The accuracy types can be categorized from lower to higher. Higher accuracy settings provide more reliable camera position estimation because it uses every single image as a source quality. From higher to lower quality, the software reduces the images' resolution and accuracy and shortens the processing

time. Medium setting causes image downscaling by a factor of 4 compared with the higher quality, and Lower quality causes image downscaling by a factor of 16 times.

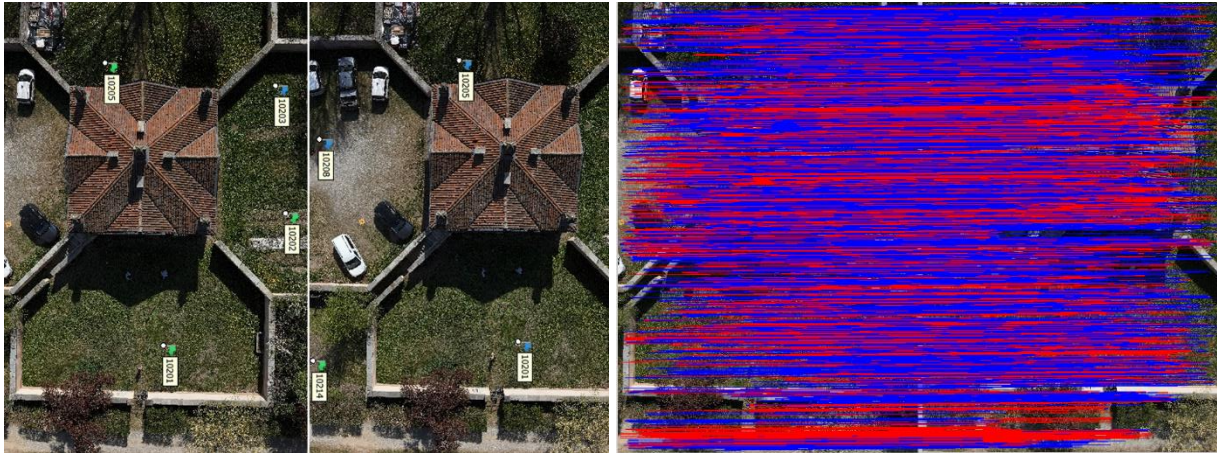


Figure 5. 2 Matched points can be viewed in Agisoft MetaShape after the alignment is done. The blue lines show valid matching, while the red ones indicated non-matched.

5.2. Georeferencing with GCPs

For the model to be created with the aerial images to be obtained in the research using the UAV to give the correct information, the place where the imaging is made must be recorded following the coordinate system.

In this context, two different methods were used to determine the model's geographical reference: direct and indirect.

Thanks to their remote sensing sensors, UAVs allow them to accurately measure the geographical position of the Earth (easting, northing, and altitude) without the need to use traditional-based direct georeferencing measurement methods such as Ground Control Points. In this direction, GPS (Global Positioning System) and GNSS (Global Navigation Satellite System) systems have been established on UAVs to make measurements. For Indirect Georeferencing, targets with coordinates are placed on the survey area, which can be identified in photographs to increase precision. These targets are called Ground Control Points (GCP).

When we compare the two methods, although the direct georeferencing method is faster and low-cost, if it may be affected by environmental and weather conditions or vehicle-related problems, uncertainties or discrepancies can be seen in the precise points required to be calculated in the survey. For this reason, although it is costly and time-consuming due to the consumption of more labor in the indirect method, more precise results are achieved than in the direct method.



Figure 5. 3 Modules of Ground Control Points (GCPs)



Figure 5. 4 Leica GNSS1200



Figure 5. 5 GNSS on a tripod

In Reality Capture, at least two different images must be defined to see the projections of the same GCP. Meanwhile, Agisoft Metashape is enough to see all the projections for each Ground Control Point (GCP) after defining one marker on a single image. Nevertheless, in some cases, it needs manual intervention to increase its accuracy. Ground Control Points (GCP) may need to be adjusted for the following reasons:

- The reference point at the target's center cannot be located because the sun reflects off the target's surface, leaving a glint that makes a clear view impossible.
- As the placed targets are surrounded by trees or vegetation during imaging.
- Due to the area's topography, the target cannot be fully visualized in some angled images.
- Resolution of images may not be suitable according to the selected camera sensor or the distance from the survey's acquired image.

After we pointed the markers in the center of GCPs at the images, each software created the Error values of every singular image as a metric(m) and Pixel (pix). The error value indicates how much the pointed center of the same targets was displaced in all images as a pixel and metric. When GCPs are used in the survey, and the model's sparse cloud is filtered for precise results, the error results would be between 0 to 2 centimeters.

For the Benchmark case, the coordinate axes: easting, northing and the altitude (E, N, A) in the coordinate system of OSGB 1936 / British National Grid – EPSG:27700 and for the Villa Ghia case, the coordinate axes: easting, northing and the altitude (E, N, A) in the coordinate system of WGS 84 / UTM zone 32N. After the coordinate system is selected in the software, the labels of GCPs defined correctly by choosing each projected image and adding markers to it. Otherwise, when the GCP coordinates are imported into the software, they would not match with the labels, and it cannot provide an accurate result for the location.

Error-values were detected as high in several markers. Firstly, camera parameters are optimized with all the markers to obtain reliable results. Then after using the ‘‘Gradual Selection Tool’’ selection, markers with high error values are removed from the model.

5.2.1 Georeferencing without Ground Control Points

For UAVs to perform an autonomous flight, they must be connected to the GNSS system. GNSS also performs georeferencing, and Real-Time Kinematic (RTK) is estimated centimeter-level positioning in real-time based on the correction signal sent to the GNSS receiver by a fixed station (Ekaso et al., 2020). It aims to reduce dependency on ground control points, which will increase the accuracy of measurements, by making future georeferencing directly from the satellite (Wanninger, 2004). Considering the high sensor cost, using Real Time Kinetics (RTK) is a more economical solution. However, if it is desired to increase the accuracy of Direct Georeferencing (DG), parameters that are not included in GNSS RTK such as Inertial Measurement Unit (IMU), Inertial Navigation System (INS), adaptation of motorized yaws moving in flight, image clarity, and overlap also need to be developed, typical as photogrammetric processing from Structure from Motion (SfM) (Sherwood et al. 2018).

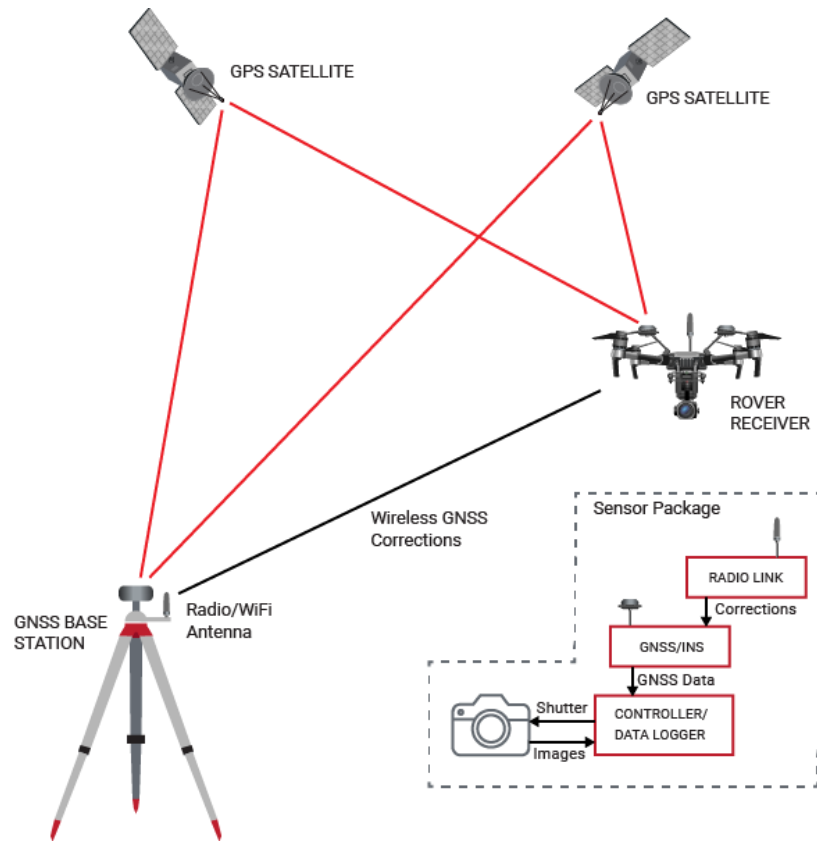


Figure 5. 6 Work principle of RTK

Figure from: <https://geo-matching.com/content/vectornav-gnss/ins-systems-for-aerial-photogrammetry>

5.3. Tie Points Filtering

The purpose of the gradual selections is to filter and adjust the erroneous and mismatched tie points in the sparse and dense clouds and allow more accurate results with these parameters. The gradual selection tool in Metashape includes four different options. Reprojection Error, Reconstruction Uncertainty, Image Count, and Project accuracy. Except for the Image Count, three of these processes have been tested for creating more accurate and fewer tie points in a cloud model.

Reconstruction Uncertainty: Reconstruction uncertainty is related to the precision of key points in the cloud. It takes the intersection of two rays and identifies a direction where the variation for that point position is at a maximum and a minimum. These minimum and maximum values are divided, and a level of uncertainty is assigned to each point within a dense or sparse point cloud.

Projection Accuracy: This parameter indicates the localized irrelevant points in the cloud and saves the accuracy proportion for each phase.

Reprojection Error: Reprojection error indicates the distance between the point where a three-dimensional point created on the model is projected and the projection of the point where this three-dimensional point is marked in at least two different images.

To acquire a high-quality cloud model in the Metashape, noise filtering was applied with the Gradual Tool Selection option. Respectively, the reconstruction uncertainty, projection accuracy, and reprojection error selections were applied to remove overlapping points and winnow out the inaccurate points, in a way that would not exceed 10% of the number of points and would not impair the accuracy of the model.



Figure 5. 7 Noise filtering point selection in the model

The overlapped points of the exact location occur the uncertainty of the accuracy of the models. Figure 5.6. displays gradual selection tools to define the key points of overlapped images, select and remove the points that cause uncertainty, and create more accurate models. The pink dots represent the overlapping dots in the same location and are removed in software by noise filtering.

5.4. Building Dense Cloud

The next step after the photo-alignment phase is Build Dense Cloud. The point cloud model is generated based on the images and camera positions at this step. The points are generated from the geometry of the modeled area.

In Metashape, each image imported to the software contributes to point cloud generation. The software calculates depth information for every image into a single-point cloud based on estimated camera positions with three axes of coordinate (Agisoft LLC, 2019: 25-26).

Some parameters must be set before starting to build dense cloud processing:

Quality: Generating Dense Cloud includes five different processing options from Ultra High to Lowest. Higher quality options provide more detailed models simultaneously because processing the density of pixels requires a longer time for processing. When Ultra High-quality runs with the original photos, every downscaling quality by 4 factors (Agisoft LLC, 2019: 25-26). To reduce time, obtain a good model resolution, and for the small file size, the quality was set as a medium for three different camera sensors (DJI Zenmuse P1, DJI Zenmuse L1, and DJI Phantom 4 RTK) and both survey areas (Benchmark & Villa Ghia).

Depth Filtering Modes: In this phase, Metashape determines depth maps for every single image from a survey. It allows the user to determine which option to use to avoid outlier values in the point cloud due to noisy or defocused images. According to the desired results for processing, there are four different options to choose from for processing. (Mild, moderate, aggressive, and disabled.)

Mild depth filtering is recommended for complex projects because it allows for filling the spatial areas, unlike the Aggressive Depth option. This way, essential features will not be detected as outliers and will remain in the model. If the dense cloud includes unnecessary details, The Aggressive Depth option is helpful to distinguish outliers and remove them. Therefore,

Aggressive Depth's process time is shorter than Mild Depth filtering. To obtain detailed and better results, the Mild Depth option was selected for both projects.

Calculate Point Colors: It allows the user to get dense clouds in color or gray tones. If color tones are unimportant, gray tones would be selected to save time.

Reuse depth maps: It provides to reuse of the depth maps in the chunk for generating dense cloud processes.

5.5. Generate Mesh and Texture

Build mesh is the phase that links the bunch of three adjacent points to the triangular surface, joins all the points with each other, and generates the solid mesh and smooth surface of the model. The higher quality and adjusted dense cloud allow the creation of more solid surfaces on the mesh. When the mesh surface is reconstructed and the location of the cameras is known, a textured mesh can be generated with matched colors from survey photos.

Agisoft Metashape allows building to mesh with its textured model simultaneously, while it must be processed separately in Reality Capture. The calibration of parameters is nearly the same in both software, and the quality of models is close to each other, but when the processing time is compared, Reality Capture is faster than Metashape in generating a mesh and textured model.



Figure 5. 8 and Figure 5. 9 Generated Photogrammetric Model of Villa Ghia in Reality Capture, Mesh (left) and Textured Model (right)

5.6. Generate of Digital Elevation Models and Orthoprojection

Orthoprojection is a high-resolution image of overlapped and merged survey photos taken from the UAVs, and due to the perspectival elevation dislocations of overlapping, orthoprojections are geometrically corrected for camera tilt, topographic surface, and lens distortion, which allows removing topographical effects and creates same scale and distance measurement all around the image. Orthoprojection transforms three-dimensional surfaces into a two-dimensional homogenous and highly detailed product.

To create an Orthoprojection image, Digital Terrain Models or Digital Surface Models must be used because DTM projects the digital cartographic dataset, which defines each object's point of elevation on the Z axis and its position on the X and Y axis throughout the coordinate system. DTM does not include non-topographic features such as buildings, vegetation, and any other infrastructure because it represents the bare topography. On the contrary, the Digital Surface Model captures all the elevation features on the topography because DSMs represent the current surface of the ground with the natural and artificial elements. In both model types, the height of the objects will be defined with different colors for each Pixel according to their elevation, which allows recognition of the differences between the terrain and the object. In photogrammetry studies, usually, the Digital Surface Model is followed.

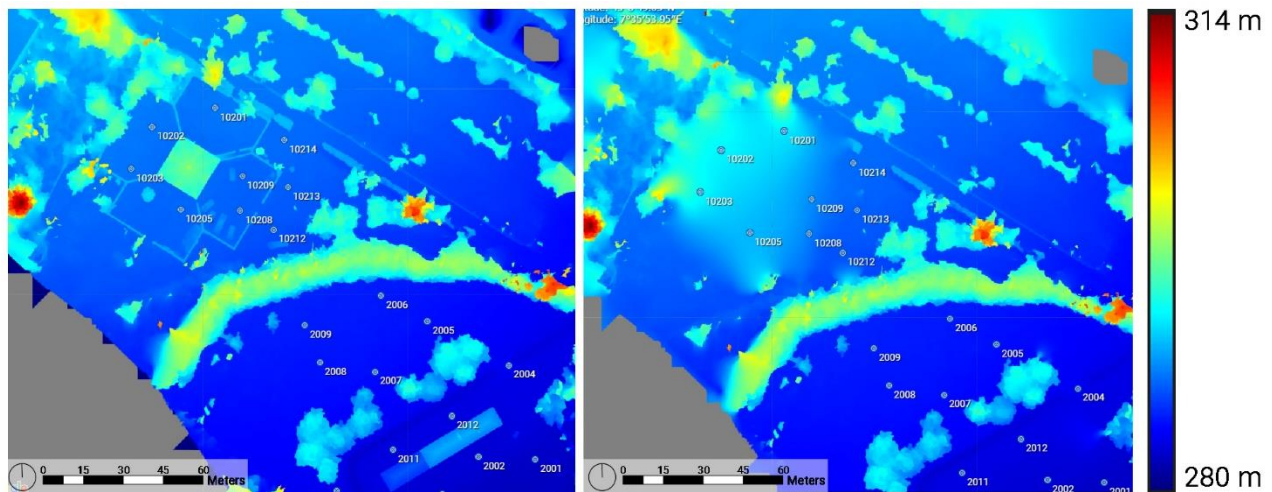


Figure 5. 10 And **Figure 5. 11** the Digital Surface Model (left) and the Digital Terrain Model (right).

The main difference between both models, DSM considers natural and artificial features on the ground and generates the models with a higher altitude, as mentioned above. The altitude on the surface is

defined from the light to the dark colors for expressing when the elevation is increased. As seen from the DSM model(left), the higher elevation has shown with the red and orange tones instead of green and blue.

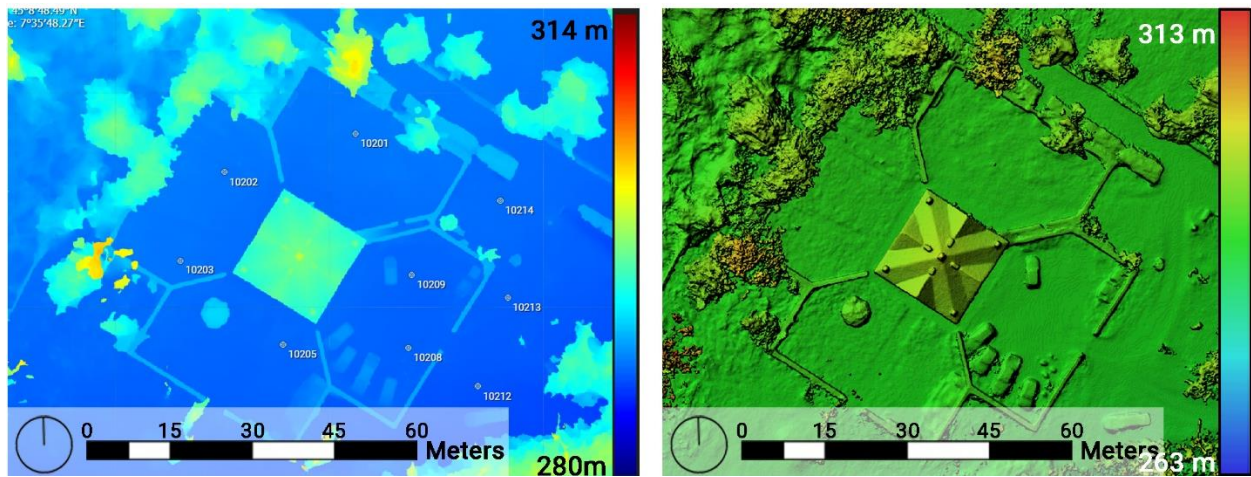


Figure 5. 12 and **Figure 5. 13** two Digital Surface Models from the exact location but processed with different software. (Left - Reality Capture and right – Metashape)



Figure 5. 14 and **Figure 5. 15** the difference between mesh (left) and Orthorectification photo (right).

The difference in accuracy and perspective can be seen between the two photographs. Orthorectification can be considered the "Orthorectified" version of aerial photo, which means geometrically corrected for the lens distortion and camera angle. The model's perspective is

visible in the aerial image, and the high resolution and great detail in the Orthoprojection photo on the right can be seen.



Figure 5. 16 and Figure 5. 17 Orthoprojection seamline method taken by different software.

Figure 5. 15 (Metashape) shows uniform parceled regions based on photos taken from the UAV during the survey. On the other hand, Figure 5. 16 (Reality Capture) shows a parceled randomly done by the software. When chosen, the random parcels display higher resolution Orthoprojection making it easier to analyze the details of the Orthoprojections.

5.7. Cloud-to-Cloud (C2C) Distance:

Cloud-to-cloud distance is one of the features of point clouds that allow defining the nearest neighbor distance. This software is free to use and helps calculate and compare different 3D point clouds and triangular meshes. It started development in 2003 and has been a crucial part of the photogrammetry software.

Cloud-to-Cloud comparison is a method that finds the closest point in a point cloud by either finding the closest neighboring point or calculating the distance from a reference point in the point cloud, which is identified by the best-fitting plane going through the closest point and its neighbor. This procedure is the simplest solution to monitor differences between the point clouds; however, it does not allow distinguishing between negative or positive charges. The density of the point clouds and model overlapped will define the accuracy of the distance estimation. (La Rocca, 2020)

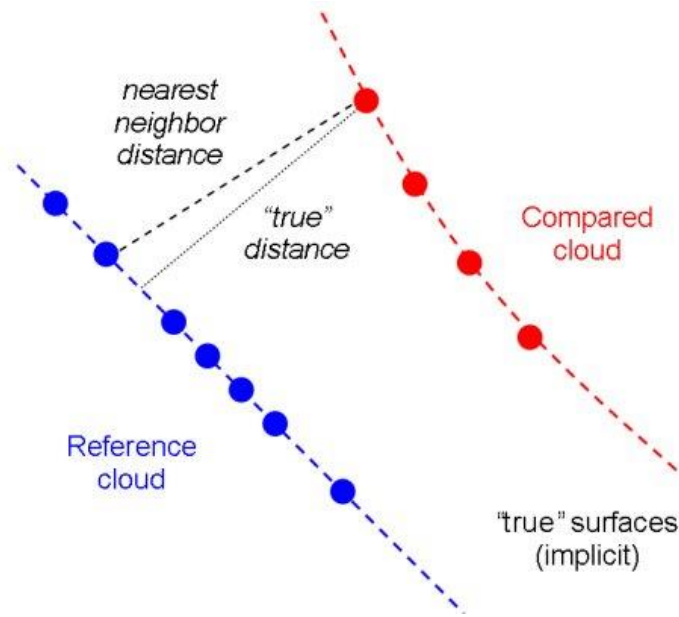


Figure 5. 18 The scheme of Cloud-to-Cloud work principle

To estimate the distance between the two clouds, a cloud-to-cloud (C2C) distance assessment was applied between the two georeferenced clouds, which were taken from the same survey with the exact coordinates but scanned with different camera sensors. To perform this process, three different camera sensors' clouds (DJI Zenmuse P1, DJI Zenmuse L1, and DJI Phantom 4 RTK) were compared with each other, with the DJI Zenmuse P1 camera sensor as a reference, just because this sensor is the densest and detailed one among them, which allows obtaining of more accurate results.

The sensors' data were processed separately for each software. The cloud-to-cloud distance of these three sensors was computed using the maximum distance parameter of 50 mm to estimate better the distance of both the same cloud points acquired in the different sensors.

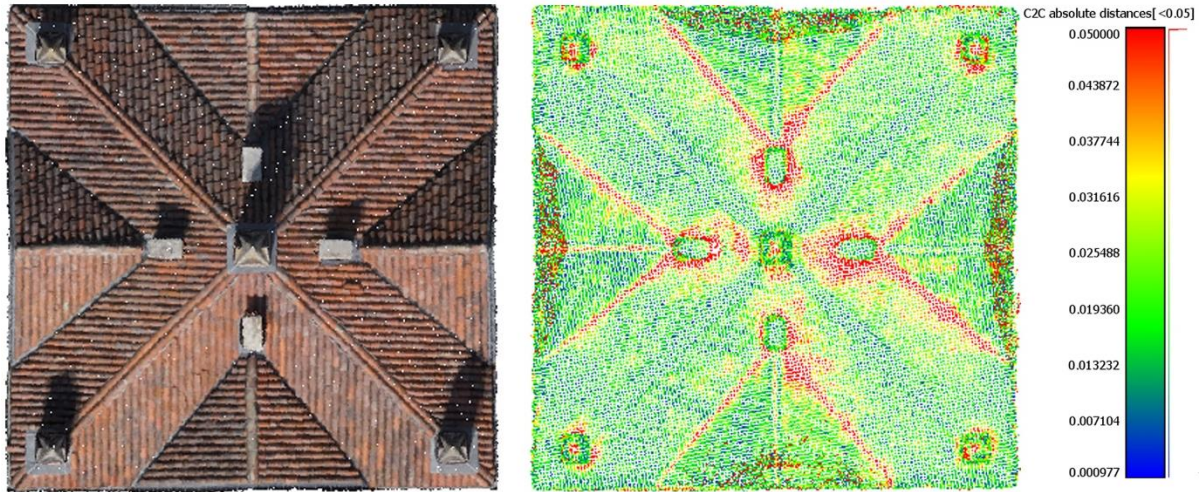


Figure 5. 19 C2C distance analysis generated by CloudCompare

The model with higher resolution and accuracy was accepted as the reference (left). In the compared model (right), the matching distances in the two models were calculated, and the distance values were defined to progress from blue to red.

6. Model Analysis and Results

6.1. Benchmark Case Study

This chapter presents the obtained data and UAV Photogrammetry modeling of the survey at Wards Hill Quarry in England and Villa Ghia in Turin. The same three sensors (DJI Zenmuse P1, DJI Zenmuse L1, and DJI Phantom 4 RTK) were used for surveying in both case studies. The Benchmark study has three different data stages. The first stage includes raw data obtained without using precision-enhancing methods such as GCP, the second stage includes images enabled by the GNSS base station, and the third stage includes data that is planned to contain the most accurate result, including both GNSS base station processing and GCPs. Since the data of the Benchmark was already ready and freely distributed, this study was considered as a theoretical study; together with the methods and information learned from here, the survey of Villa Ghia was made from beginning to end, and the results were analyzed. The sparse cloud models of these two studies were simultaneously created by two different software, and the dense cloud model, Digital Elevation Model (DEM), and Orthoprojection were generated respectively from these dense cloud models. The results of each sensor are used without adjusting the data, so obtained data can be compared with each other in the best way. The Reality Capture software was used only in the Villa Ghia case study because, in the absence of GCPs, Benchmark data processing in Reality Capture has yielded incomplete and confusing results to define error deviations. The parameters used in the model creation process and the attributes of the created model are given in

Table 6. 1 Input and Output results of Benchmark and Villa Ghia by Metashape

Input and Output Result	Matched & Total Images	Tie Points	Depth Map Parameters	Dense Point Cloud	Polygon Faces in Models	DEM Resolution (cm/pix)
BM P3 – P1	994/994	513,853	Medium/Mild	206,138,307	15,910,825	2.8
BM P3 – L1	252/252	264,693	Medium/Mild	47,522,406	1,829,847	6.68
BM P3 – Phantom	500/500	248,590	Medium/Mild	38,959,682	1,955,603	7.24
V. G. P1	789/897	548,457	Medium/Mild	127,972,844	5,246,221	2.89
V. G. L1	126/140	88,610	Medium/Mild	17,662,955	1,177,525	6.04
V. G. Phantom	475/497	278,851	Medium/Mild	32,491,270	2,166,058	5.91

The table 6.1. shows the models' characteristic features when they are created with the same parameters. DJI Zenmuse P1 sensors' tie points, polygon faces, and dense point cloud are greater

than DJI Zenmuse L1 and DJI Phantom 4 RTK due to the number and resolution of the acquired images during the survey.

Table 6.2. The overview of the data generated by Metashape in these two case studies..

	Date	Number of Images	Flying Altitude	Ground Resolution (cm/pix)	Tie Points	Projections	Reprojection error (pix)	Coverage area (km²)
BM P1	08.21	999	56.8 m	0.69	516,057	3,699,858	1.56	0.0731
BM L1	08.21	254	60.4 m	1.75	176,582	545,027	0.751	0.0847
BM Phantom	08.21	489	60.4 m	1.66	197,080	950,670	0.935	0.0753
V. G. P1	04.22	897	57.5 m	0.72	548,457	1,647,346	0.876	0.0509
V. G. L1	04.22	140	52.4 m	1.51	88,610	258,137	0.698	0.0391
V.G. Phantom	04.22	498	49.5 m	1.48	278,851	824,186	1.08	0.0536

Table 6.2. indicates the overview of the Benchmark and Villa Ghia case studies. The surveys were performed between the 50-60m altitude. In both case studies, DJI Zenmuse P1 has a high projection error in direct proportion to projection and has the lowest ground resolution value among the three sensors.

Camera location errors can directly affect the georeferenced position of the models. The camera position errors of the models produced in Metashape are listed in **Table 6.3**. The acquired data are added to the Metashape report, which consists of alignment and other steps after calibration.

Table 6. 3 Camera Location Error of Metashape Models

Camera Location Sensor & Phase	X error (m)	Y error (m)	Z error (m)	XY error (m)	Total error (m)
Phase 1 – P1	0.093	0.141	0.259	0.169	0.309
Phase 1 – L1	0.190	0.232	2.465	0.299	2.483
Phase 1 - Phantom	0.220	0.372	0.790	0.433	0.901
Phase 2 – P1	0.086	0.058	0.423	0.103	0.436
Phase 2 – L1	0.145	0.109	0.520	0.182	0.551
Phase 2 - Phantom	0.158	0.194	0.237	0.251	0.346
Phase 3 – P1	0.727	0.375	1.562	0.818	1.763
Phase 3 – L1	0.695	0.386	0.834	0.795	1.152
Phase 3 – Phantom	0.736	0.382	0.786	0.829	1.142
Villa Ghia P1	1.241	0.606	50.533	1.382	50.552
Villa Ghia Phantom	0.346	0.204	50.477	0.402	50.479
Villa Ghia L1	0.123	1.338	49.267	1.344	49.286

Table 6.3 contains the camera location errors of the Metashape models. The presence of the GCPs in the Benchmark test site caused the camera location errors to increase because the aligned images' position is corrected with the imported GCPs, and the estimated position of the images is changed. The processed images with the GNSS base station data showed the lowest camera location error result between 34-55 cm. Villa Ghia measurements, we obtained 50.552, 50.470, and 49.286 meters of error margins for the P1, Phantom, and L1 sensors. These margins appear to be much larger than those we obtained from the sensors in Phases 1, 2, and 3. These error margins are caused by the geoid, uneven surface of the Earth, as opposed to the ideal, smooth, hypothetical ellipsoid surface required by the sensors to produce highly accurate measurements.

Table 6. 4 Ground Control Points error of Benchmark and Villa Ghia generated by Metashape

GCP Sensor & Phase Name	X error (cm)	Y error (cm)	Z error (cm)	XY error (cm)	Total error (cm)
Phase 1 – P1	1.54	2.57	2.27	3.00	3.76
Phase 1 – L1	1.86	1.61	0.52	2.46	2.51
Phase 1 - Phantom	6.09	11.34	3.30	12.87	13.29
Phase 2 – P1	2.56	1.50	3.36	2.97	4.48
Phase 2 – L1	3.24	3.05	1.13	4.45	4.59
Phase 2 - Phantom	4.60	7.79	7.09	9.05	11.49
Phase 3 – P1	0.33	0.35	0.35	0.48	0.59
Phase 3 – L1	0.27	0.29	0.47	0.40	0.40
Phase 3 – Phantom	0.37	0.40	0.56	0.55	0.78
Villa Ghia P1	1.25	1.22	1.83	1.75	2.53
Villa Ghia Phantom	1.21	1.06	1.37	1.61	2.11
Villa Ghia L1	1.30	1.24	1.95	1.79	2.65

Table 6.4. displays the error values of the three sensors in the Benchmark and Villa Ghia case studies. The GCPs are used in the Villa Ghia and Benchmark’s third phase. It can be seen from the table these models’ results have the lowest error values when they are compared with Phase 1 and Phase 2. In the absence of GCPs, a large fluctuation in error values is observed in the DJI Phantom 4 RTK sensor, and the total error decreased from 13.3 cm to 0.8 cm when GCPs are imported into the model. Except for the DJI Phantom 4 RTK Phase 1 results, the error values didn’t exceed 8 cm in any phase of the Benchmark and Villa Ghia test site. DJI Zenmuse L1 has the lowest and most consistent GCP error results between 0.4 cm to 4.59 cm when it is compared with other sensors.

After the models were processed in the software, the density analysis and cloud-to-cloud distance between the sensors' clouds performed in CloudCompare, was used to analyze the facade and the roof. In these analyses, while the dense cloud of the whole building is required in the C2C distance analysis, the analyses were made in the density analysis in modules of 5 x 5 meters from the roof and characteristically the most prominent facade. The result of analysis showed that the DJI Zenmuse P1 was the most significant sensor due to its resolution, details, and abundance of images recorded in the survey. For this reason, this sensor was chosen as a reference cloud model when computing the cloud-to-cloud distance.

Agisoft Metashape computes other criteria, such as ground resolution, projections, and projection errors, to evaluate the project's accuracy and the images' positions. The values of these parameters are given below in **Table 6.5**. Ground resolution is also known as Ground Sampling Distance (GSD). The distance between the centers of the two closest pixels to each other. In this case, it can be said that as the distance of the image between consecutive pixels increases, its resolution and details decrease. The projection value is the measurement of the distance of the same point in the cloud point in two different photographs with triangulation technique. On the other hand, the reprojection error is the average distance between the images' tie points. Each point is reprojected via the root mean, and the resulting distance deviation is called the margin of error. (Agisoft LLC. (2019))

Table 6.5 The value of Ground resolution, projections and reprojection error of Metashape models.

Site name	Ground resolution (mm/pix)	Projections	Reprojection error (pix)
Phase 1 – P1	6.92	3,699,858	1.56
Phase 1 – L1	1.75	545,027	0.751
Phase 1 - Phantom	1.66	950,670	0.935
Phase 2 – P1	6.91	3,696,534	1.57
Phase 2 – L1	1.71	852,156	1.12
Phase 2 - Phantom	1.8	1,617,081	1.33
Phase 3 – P1	6.9	2,246,816	1.18
Phase 3 – L1	1.71	807,571	1.3
Phase 3 – Phantom	1.8	1,687,064	1.47
Villa Ghia P1	7.24	1,647,346	0.876
Villa Ghia L1	1.51	258,137	0.698
Villa Ghia Phantom	1.48	824,186	1.08

Table 6.5 shows the ground resolution, projections, and reprojection error in both case study models generated by Metashape. DJI Zenmuse P1 has the greatest result among these three-characteristic features. When the Villa Ghia and Benchmark are compared, Villa Ghia's DJI Zenmuse P1 sensor has shown better ground resolution and reprojection error than Benchmark while DJI Zenmuse L1 and DJI Phantom 4 RTK have lower quality results.

6.1.1. Benchmark – DJI Zenmuse P1

The data was acquired with the P1 camera sensor mounted to the DJI Matrice 300 drone in Benchmark's case study. Since the survey data of all three stages does not change in the Benchmark, and only the methods are different in these three stages, the data obtained from these stages will be given under each sensor, respectively. The combination of all 999 photos recorded at an altitude of about 56.8 meters was used to create the model. To align the images more accurately and efficiently, 8 ground control points and 51 control points were placed on the site, but since the coordinate information of only eight ground control points was given, 51 control points (CPs) were not included in this study. At least 10 images for each control point are marked in Metashape to increase the accuracy of the results. After the photo alignment, necessary filters were applied to improve the model's accuracy, and a sparse cloud was created. To process dense cloud after sparse cloud, medium quality option and mild depth filtering parameters are used in terms of quality/duration performance. Thus, a smooth model surface with no roughness on the surface was obtained. After the dense cloud was created, the DEM creation phase from the tie points and the Orthoprojection production based on the Digital Elevation Model was followed.

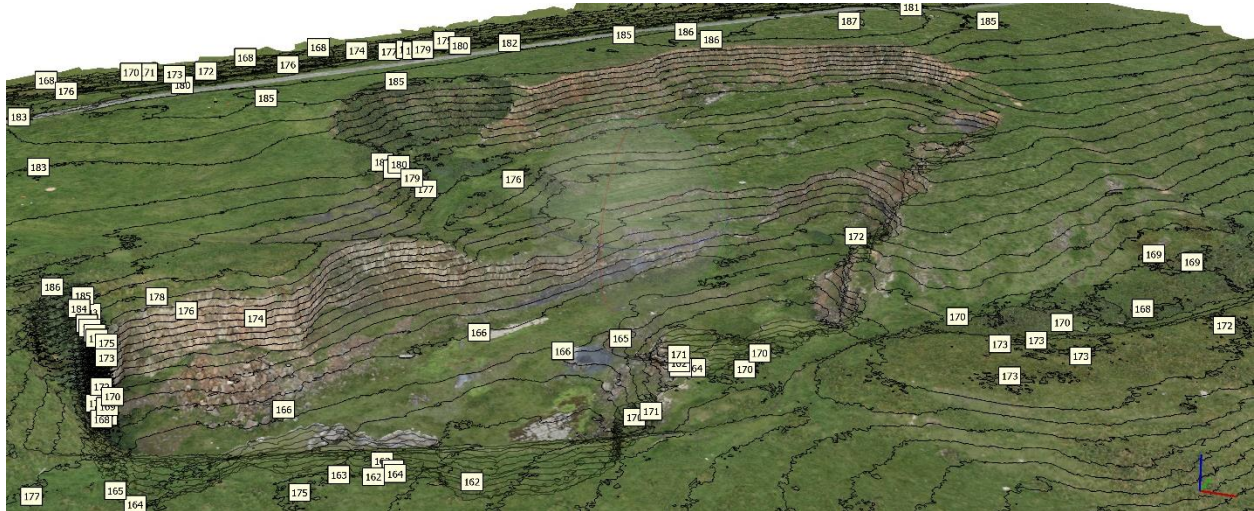


Figure 6. 1 the generated contour lines of the Benchmark site by Agisoft Metashape. It can be seen the elevation difference of the quarry in the center of the model.

Table 6. 6 The initial data obtained for the Benchmark case study with the Zenmuse P1 sensor.

Label	X error (cm)	Y error (cm)	Z error (cm)	Total Error (cm)	XY Error (cm)
GA1	-1.9	-0.2	-0.3	2.0	1.9
GA5	0.2	1.4	0.7	1.6	1.4
GA8	0.6	-1.2	-0.6	1.4	1.3
GF1	2.1	2.1	0.4	3.0	3.0
GF4	0.0	-3.7	-1.0	3.8	3.7
GF8	-1.0	1.6	0.8	2.0	1.9
Check Points					
GC6	-0.1	-4.2	12.6	2.0	4.2
GD4	3.3	-4.8	-6.6	1.6	5.8

Table 6. 7 The enabled images acquired for the Benchmark case study with the Zenmuse P1 sensor.

Label	X error (cm)	Y error (cm)	Z error (cm)	Total Error (cm)	XY Error (cm)
GA1	-2.5	-1.3	0.3	2.9	2.9
GA5	0.2	-0.6	0.2	0.7	0.7
GA8	0.8	-0.9	-0.5	1.3	1.3
GF1	0.8	2.9	-0.2	3.0	3.0
GF4	-0.3	-1.3	-0.1	1.3	1.3
GF8	0.9	1.3	0.3	1.6	1.6
Check Points					
GC6	-2.7	-1.5	16.0	16.3	3.1
GD4	6.3	-0.3	-19.9	20.8	6.3

Table 6. 8 Error values after GCPs imported model of the Zenmuse P1 sensor.

Label	X error (cm)	Y error (cm)	Z error (cm)	Total Error (cm)	XY Error (cm)
GA1	0.1	0.4	0.0	0.5	0.5
GA5	0.0	0.3	0.0	0.3	0.3
GA8	-0.4	-0.4	0.0	0.6	0.6
GF1	-0.2	-0.3	-0.1	0.4	0.4
GF4	0.6	-0.2	0.2	0.6	0.6
GF8	-0.1	0.1	-0.2	0.2	0.1
Check Points					
GC6	-0.1	-0.5	-1.6	1.7	0.5
GD4	0.2	-0.2	-2.9	2.9	0.3

Tables 6.6, 6.7, and 6.8 demonstrate the error values of the DJI Zenmuse P1 sensor's Phase 1, 2, and 3 generated by Metashape. Phase 3 shows the lowest error due to processing with GCPs and increased preciseness of the model. The error of Phase 2 mostly has the highest values among these three phases. The maximum total error of control points is 3.8 cm in Phase 1, 3 cm in Phase 2, and 0.3 cm in Phase 3.

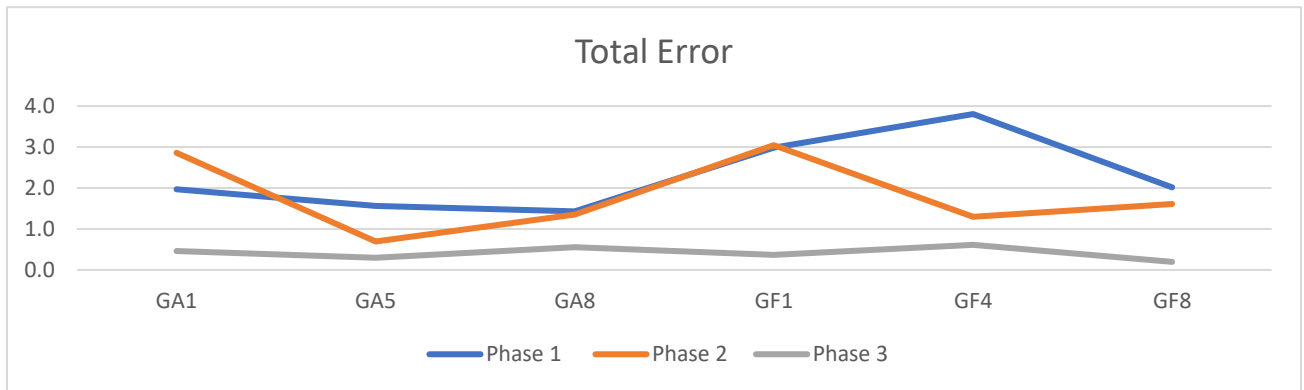
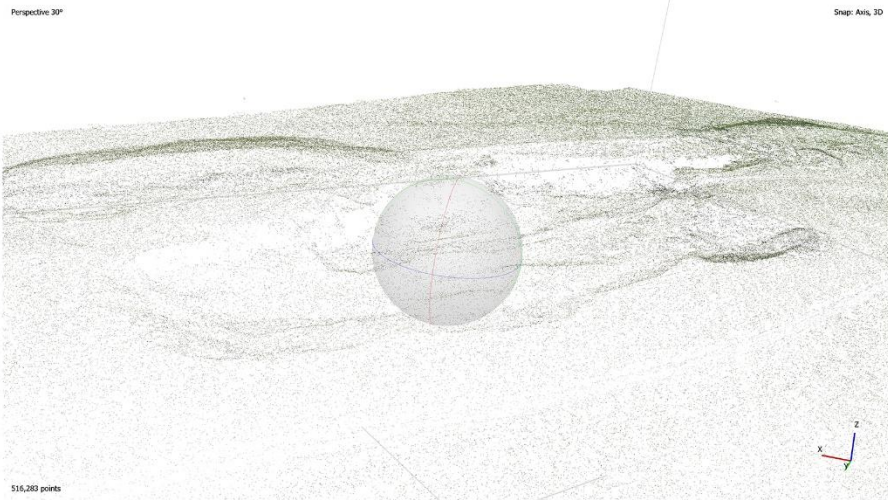


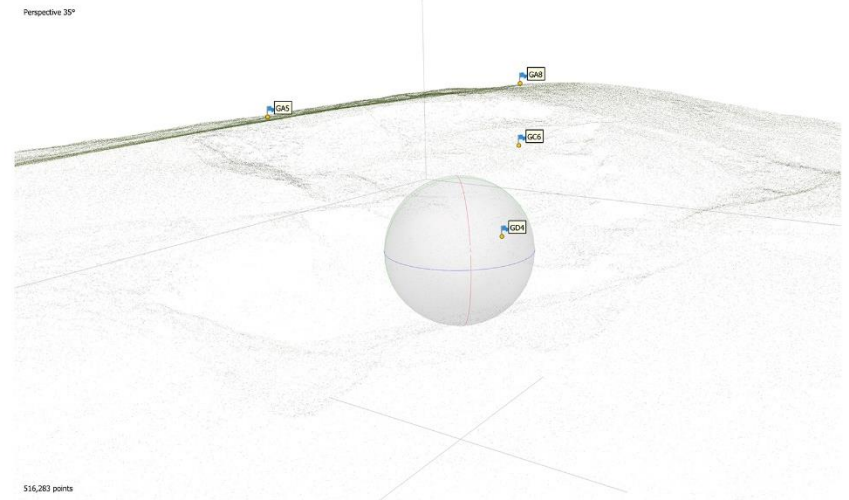
Figure 6. 2 the Total Error values of the DJI Zenmuse P1 Sensor



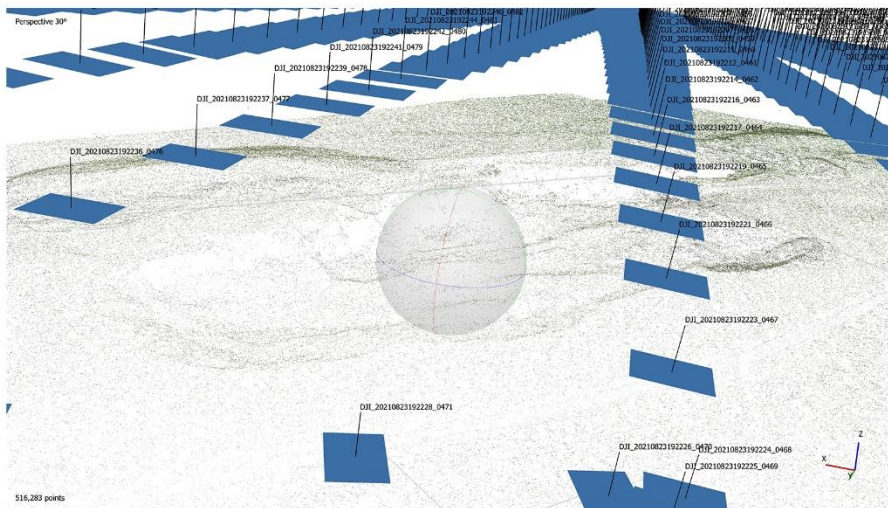
Figure 6. 3 the Orthoprojection image of the DJI Zenmuse P1 sensor's model



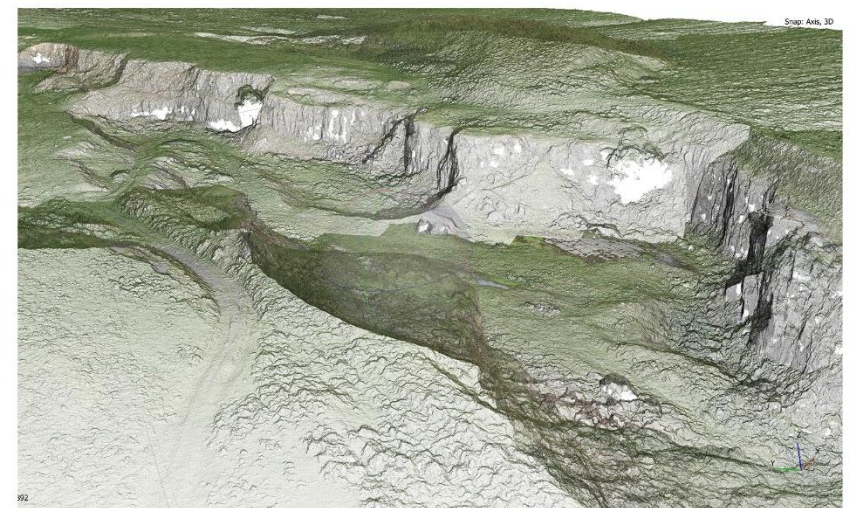
The sparse cloud generated in Metashape from nadir & inclined images acquired in the Benchmark survey.



Import of GCPs to the model generated in Metashape from images acquired in the Benchmark survey.



Accuracy check and camera calibration by Metashape in the Benchmark survey.



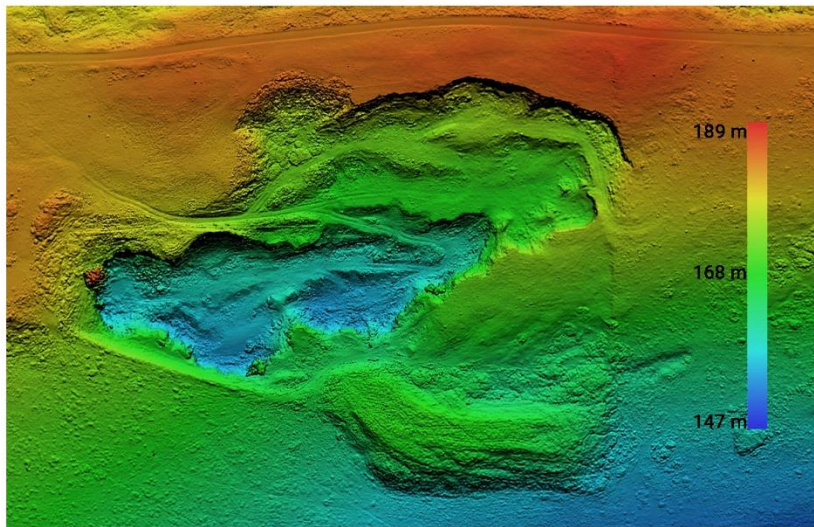
Dense Cloud in Metashape from images acquired in the Benchmark survey.



The mesh generated in Metashape from nadir & inclined images acquired in the Benchmark survey.



Model textured generated in Metashape from nadir & inclined images acquired in the Benchmark survey



Digital Elevation Model of generated model by Metashape in the Benchmark survey.



The orthoprojection of generated model by Metashape in the Benchmark survey.

Figure 6. 4 Workflow steps, camera location, mesh, texture, and Digital Elevation Model, Orthoprojection of DJI Zenmuse P1's model in Benchmark

6.1.2. Benchmark – DJI Phantom 4 RTK

The DJI Phantom 4 RTK drone and camera is another sensor used in the survey. The case study area is still the same, and the coverage area is approximately 0.09 km². Five hundred images were acquired during image acquisition, and all were successfully mapped during model creation. The altitude of the images obtained with the drone is approximately 65.4 m. Since the parameters such as camera resolution and focal length of the Phantom are lower than the P1 sensor, it was observed that the values such as tie points, ground resolution, and projections obtained after the model was created are lower. Eight Ground Control Points (GCPs) were used for processing the photogrammetric block. To increase the model's precision, ten images for each ground control point were marked in the software and aligned again as done in the P1 sensor. After the sparse cloud was created, dense cloud, mesh, texture, DEM, and Orthoprojection were created.



Figure 6. 5 Orthoprojection image of DJI Phantom 4 RTK

Table 6. 9 The initial data obtained for the Benchmark case study with the Phantom 4 RTK sensor.

Label	X error (cm)	Y error (cm)	Z error (cm)	Total Error (cm)	XY Error (cm)
GA1	8.1	-5.3	2.9	10.1	9.7
GA5	-6.9	7.4	-7.4	12.5	10.1
GA8	4.0	-5.3	5.0	8.3	6.7
GF1	-5.4	-0.7	-1.5	5.7	5.5
GF4	-1.2	-1.3	4.6	4.9	1.7
GF8	1.3	5.2	-3.6	6.5	5.4
Check Points					
GC6	-0.3	-20.9	32.1	38.3	20.9
GD4	3.5	5.6	-0.7	6.7	6.7

Table 6. 10 The enabled images acquired for the Benchmark case study with the Phantom 4 RTK sensor.

Label	X error (cm)	Y error (cm)	Z error (cm)	Total Error (cm)	XY Error (cm)
GA1	-1.9	-0.2	-0.3	2.0	1.9
GA5	0.2	1.4	0.7	1.6	1.4
GA8	0.6	-1.2	-0.6	1.4	1.3
GF1	2.1	2.1	0.4	3.0	3.0
GF4	0.0	-3.7	-1.0	3.8	3.7
GF8	-1.0	1.6	0.8	2.0	1.9
Check Points					
GC6	-0.1	-4.2	12.6	13.3	4.2
GD4	3.3	-4.8	-6.6	8.8	5.8

Table 6. 11 The error values after GCPs imported model of the Zenmuse Phantom 4 RTK sensor.

Label	X error (cm)	Y error (cm)	Z error (cm)	Total Error (cm)	XY Error (cm)
GA1	0.2	0.1	0.3	0.3	0.2
GA5	0.2	0.0	0.4	0.5	0.2
GA8	0.1	-0.4	-0.7	0.8	0.5
GF1	0.0	-0.5	-0.7	0.8	0.5
GF4	-0.8	-0.1	0.4	0.9	0.8
GF8	0.3	0.9	0.3	1.0	1.0
Check Points					
GC6	-0.4	0.1	-2.1	2.1	0.2
GD4	0.1	0.4	-0.6	0.7	0.2

Tables 6.9, 6.10, and 6.11 display the error values of the DJI Phantom 4 RTK sensor's Phases 1, 2, and 3 generated by Metashape. The results of the Phase 3 model processed with GCPs have the lowest error value of 1.0 cm. Processed with GNSS base station data, Phase 2 has the highest total error of 12.5 cm. Especially Phase 2's control points have shown a big undulation between these 3 phases.

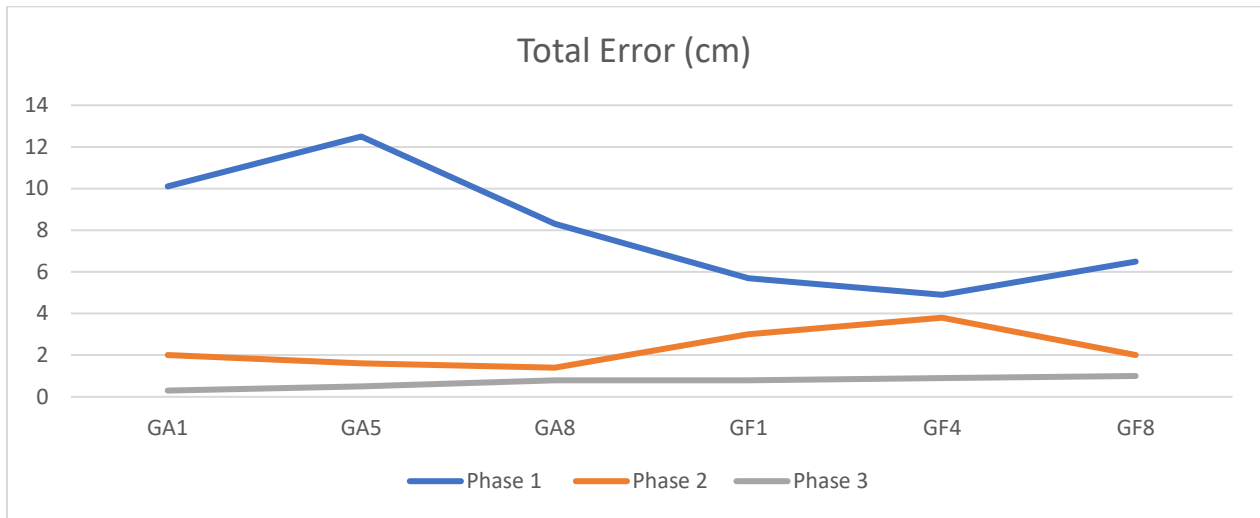


Figure 6. 6 Total Error comparison of different phases of the DJI Phantom 4 RTK sensor

6.1.3. Benchmark – DJI Zenmuse L1

The last sensor used in the benchmark case study is the DJI Zenmuse L1 sensor, which is used with the DJI Matrice 300 drone, such as the DJI Zenmuse P1. The features of the DJI Zenmuse L1 sensor, such as resolution, focal length, and pixel size, are the same as the DJI Phantom 4 RTK sensor. All 252 images recorded at an altitude of approximately 63 m of the site were successfully mapped during model creation. While the generated model's tie points and ground resolution are almost equal to the DJI Phantom 4 RTK sensor, the number of projections created is almost half.



Figure 6. 7 Orthoprojection image of DJI Zenmuse L1

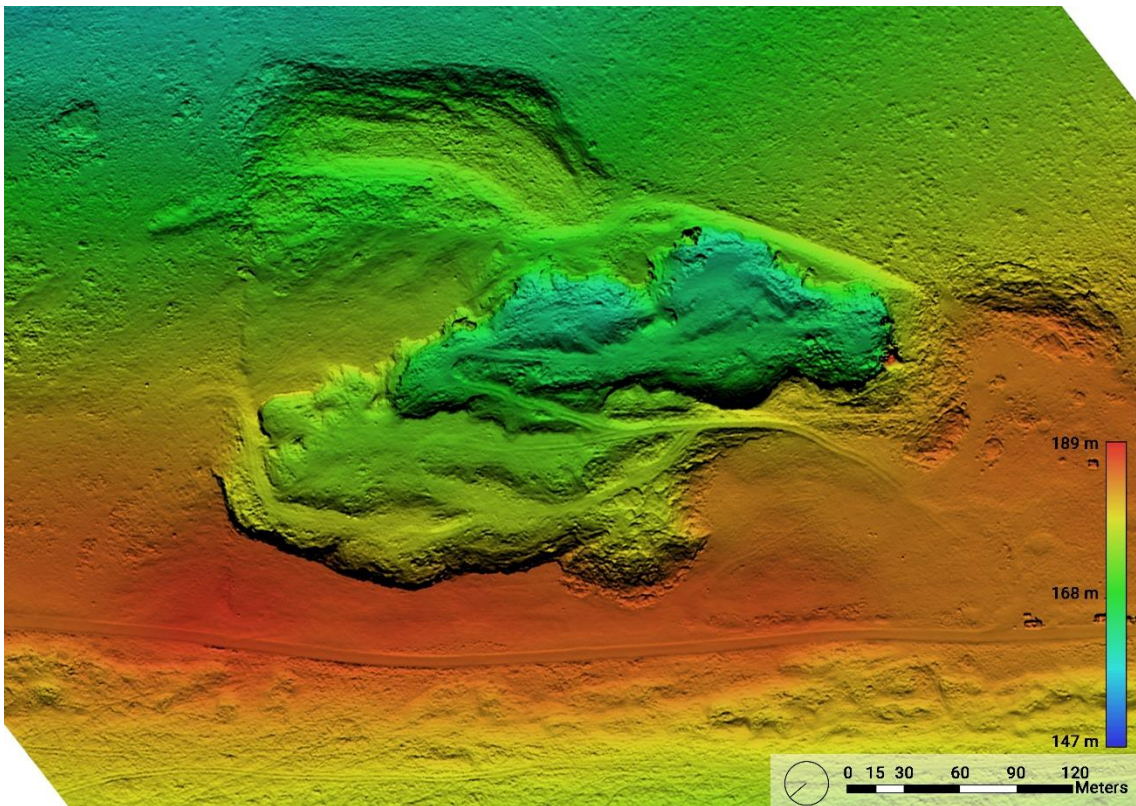


Figure 6. 8 Digital Elevation Model of DJI Zenmuse P1

Table 6. 12 the initial data obtained for the Benchmark case study with the Zenmuse L1 sensor.

Label	X error (cm)	Y error (cm)	Z error (cm)	Total Error (cm)	XY Error (cm)
GA1	-0.7	0.0	0.2	0.8	0.7
GA5	-0.2	-0.2	-0.2	0.4	0.3
GA8	-0.2	0.2	0.2	0.3	0.3
GF1	-0.5	1.1	-0.2	1.2	1.2
GF4	2.4	-0.3	0.2	2.4	2.4
GF8	-0.7	-0.8	-0.2	1.1	1.1
Check Points					
GC6	-1.4	4.1	10.7	11.6	4.4
GD4	-10.2	-6.5	-12.5	17.4	12.1

Table 6. 13 The enabled images acquired for the Benchmark case study with the Zenmuse L1 sensor.

Label	X error (cm)	Y error (cm)	Z error (cm)	Total Error (cm)	XY Error (cm)
GA1	1.1	0.8	-0.4	1.4	1.4
GA5	0.9	0.7	0.0	1.1	1.2
GA8	0.4	-0.1	0.2	0.5	0.2
GF1	3.0	-0.8	-0.1	3.1	2.9
GF4	-6.1	-4.2	0.7	7.5	5.8
GF8	0.6	3.7	-0.3	3.7	2.0
Check Points					
GC6	4.6	10.1	8.0	13.6	11.0
GD4	5.4	3.2	-64.1	64.4	6.3

Table 6. 14 The error values after GCPs imported model of the Zenmuse L1 sensor.

Label	X error (cm)	Y error (cm)	Z error (cm)	Total Error (cm)	XY Error (cm)
GA1	0.1	-0.3	-0.1	0.3	0.3
GA5	0.4	-0.1	0.0	0.4	0.4
GA8	0.1	0.0	0.0	0.2	0.1
GF1	-0.2	-0.3	0.1	0.4	0.4
GF4	-0.6	0.4	0.0	0.7	0.7
GF8	0.2	0.3	0.0	0.4	0.4
Check Points					
GC6	0.9	-0.8	2.0	2.3	1.2
GD4	0.0	-0.6	4.3	4.4	0.6

Tables 6.12, 6.13, and 6.14 show the error values of the DJI Zenmuse L1 sensor's model Phases 1, 2, and 3 created by Metashape. The results of the Phase 3 model processed with GCPs have the lowest total error value of 0.7 cm in Ground Control Points. The total error of Phase 2 has the highest value with 7.5 cm. Especially Phase 2's control points values have shown a big undulation among these 3 phases.

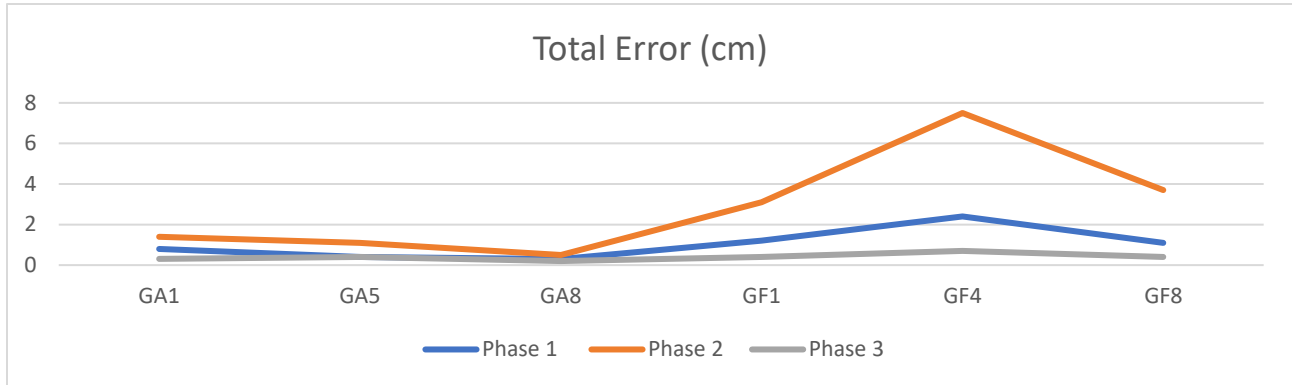


Figure 6. 9 Total Error comparison of different phases of the DJI Zenmuse L1 sensor

6.2. Villa Ghia Case Study

In Villa Ghia's study, the theoretical knowledge learned and applied for the Benchmark was used practically, images enabled with GNSS base station, and the Ground Control Points imported for creating the most precise results in the alignment phase. Twenty-two ground control points were located on the site. With the presence of the ground control points throughout the study, instead of using only Agisoft Metashape, the data was also processed with Reality Capture software to compare the results. DJI Zenmuse P1 and L1 and DJI Phantom RTK sensors were used in Villa Ghia, as in the Benchmark case study. Unlike Benchmark, it was aimed to model not only the terrain but also the buildings on the site. The analysis of the facade and roof of Villa Ghia for architectural heritage protection was created in each of the models produced, and the density analyses between the sensors were made through CloudCompare software. Image acquisitions were completed on the same day in this area, where historical buildings and vegetation are located.

6.2.1. Villa Ghia DJI Zenmuse P1 - Metashape

For the case study, an image of approximately 0.05 km² surface area was obtained with the P1 sensor. In the survey, 879 images were recorded from 57.5 m altitude, 789 of which were used for alignment. Images were processed with medium quality and mild filtering parameters.

After the alignment was done, 548,457 tie points were formed after the reflection error, reconstruction uncertainty, and projection accuracy filters were applied to improve the accuracy of the constructed model. After the Sparse cloud production, mesh, texture, DEM, and Orthoprojection production followed. The number of polygon faces formed during the mesh production phase is 1,647,346. The model's ground resolution is 7.24 mm/pix, and the reproduction error in the cloud is 0.876 pixels. Due to the resolution quality of its images and the highest number of captured images, the P1 sensor was the sensor that required the most processing time from the processing stage. Since P1 was the most advanced sensor in the survey, P1 was used as a reference in the Cloud-to-cloud distance analyses between the sensors.

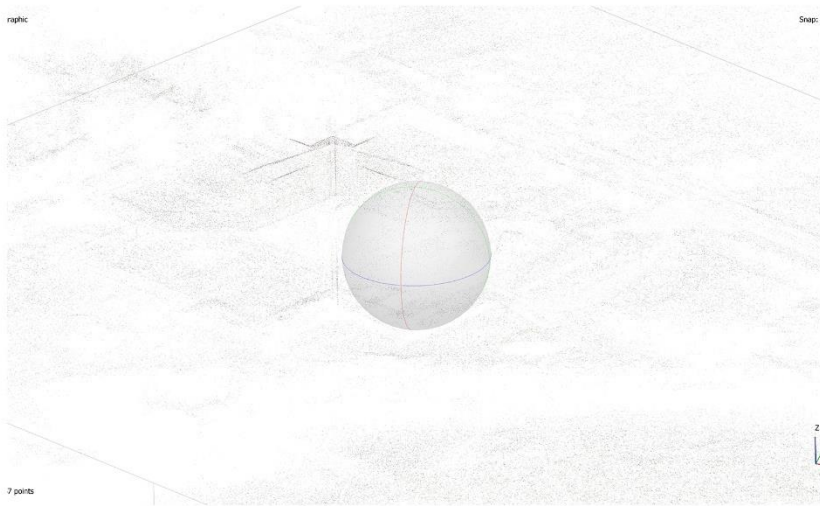
Table 6. 15 GCPs value of the P1 sensor in the Villa Ghia case study created by Metashape

Label	X error (cm)	Y error (cm)	Z error (cm)	Total Error (cm)	XY Error (cm)
2000	-2	0.7	0	2.1	2.1
2002	-1.1	-0.5	-2.8	3	1.2
2003	-1.6	0.6	-1.3	2.1	1.7
2005	1.8	3.3	1.9	4.2	3.8
2011	0.1	0.1	-0.2	0.2	0.2
2012	2.7	-0.9	-0.4	2.9	2.9
10203	-1.7	-0.3	-0.2	1.8	1.8
10205	-0.3	0.3	0.2	0.5	0.5
10208	0.1	-1.8	-2.5	3.1	1.8
10212	-0.8	-1.1	-2.2	2.6	1.4
10213	0.4	-0.7	0.1	0.8	0.8
10214	1.2	1.9	-0.2	2.3	2.3
Check Points					
2001	-0.6	-0.4	-3.3	3.3	0.8
2004	-1.4	-0.8	-2.1	2.6	1.6
10201	-0.6	1.2	0	1.4	1.4
10202	-1.8	-0.1	-0.2	1.8	1.8

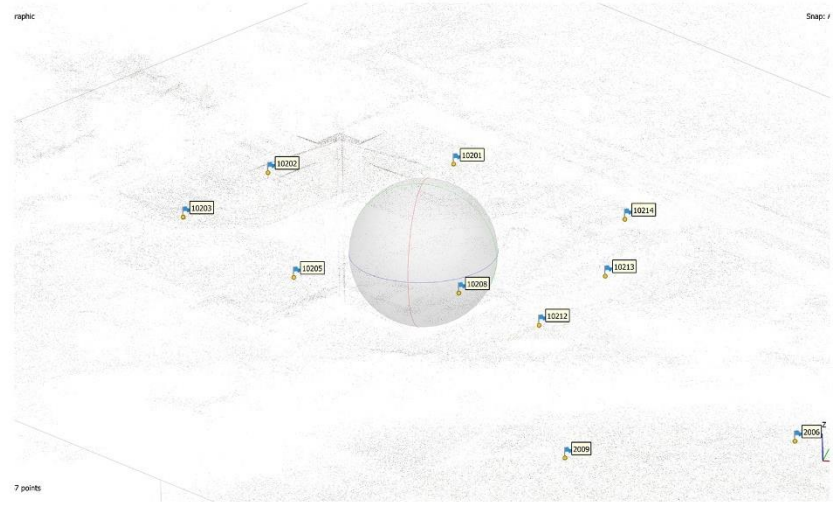
Table 6.15 indicates the error values of the DJI Zenmuse P1 sensor acquired from the Villa Ghia survey created by Agisoft Metashape. Error values are low as Ground Control Points are imported into the model and processed and the value of the Total error of the model doesn't exceed 4.2 cm along the Ground Control Points.



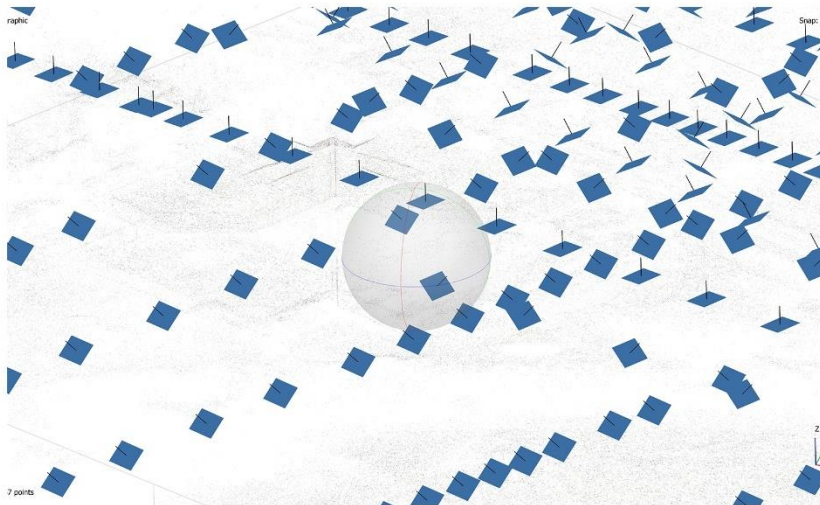
Figure 6. 10 Orthoprojection image of DJI Zenmuse P1 in Villa Ghia



The sparse cloud generated in Metashape from nadir & inclined images acquired in the Villa Ghia survey.



Import of GCPs to the model generated in Metashape from images acquired in the Villa Ghia survey.



Accuracy check and camera calibration by Metashape in the Villa Ghia survey.



Dense Cloud in Metashape from images acquired in the Villa Ghia survey.



The mesh generated in Metashape from nadir & inclined images acquired in the Villa Ghia survey.



Model textured generated in Metashape from nadir & inclined images acquired in the Villa Ghia survey.



Digital Elevation Model of generated model by Metashape in the Villa Ghia survey.



The orthorectification of generated model by Metashape in the Villa Ghia survey.

Figure 6. 11 Workflow steps, camera location, and Digital Elevation Model of DJI Zenmuse P1's model in Villa Ghia

6.2.2. Villa Ghia DJI Zenmuse P1– Reality Capture

The acquired images of the P1 sensor are also used for processing with Reality Capture. Although the processing methods are similar, the parameters are not identical as in Metashape. The downscale factor was determined as four for creating a medium-quality model in the alignment process. 987 images were imported to the software for the alignment, but 637 were used to create the model. Since Ground Control Points will be used as the base, the absolute poses of the images uploaded to the software are defined as unknown in order not to create complexity and to obtain more accurate results. Among the 7 distortion models, Brown4 with tangential2 was chosen to minimize distortions in the model. There are 681,980 tie points in the sparse cloud produced. The mean reproduction error of the generated cloud is 1.23 pixels. After creating mesh and texture in Reality Capture, The Digital Terrain Model (DTM) and Digital Surface Model (DSM) were obtained without needing additional processing, such as DEM creation in Metashape, and the results can be detailed in the report as desired. Finally, the Orthoprojection was rendered by choosing the "True ortho from a textured model" and the 0.005 ortho pixel size parameters recommended by the software for the Orthoprojection.

Table 6. 16 GCPs value of the P1 sensor in the Villa Ghia case study created by Reality Capture

Label	X error (cm)	Y error (cm)	Z error (cm)	Total Error (cm)	XY Error (cm)
2000	0.6	-0.8	-1.3	1.6	1.0
2002	1.0	0.1	1.2	1.6	1.0
2003	1.1	-0.4	-0.2	1.2	1.2
2005	-0.4	-2.6	-1.4	3.0	2.6
2011	0.5	0.7	-0.3	0.9	0.9
2012	-2.0	1.0	-0.9	2.4	2.2
10203	0.2	0.1	0.2	0.3	0.2
10205	-0.2	-0.4	-0.6	0.7	0.4
10208	-0.2	1.3	1.4	1.9	1.3
10212	1.1	0.6	1.4	1.9	1.3
10213	0.1	0.8	-0.3	0.9	0.8
10214	-0.9	-1.0	0.4	1.4	1.3
Check Point					
2001	0.1	-0.7	1.8	1.9	0.7
2004	2.1	0.2	1.6	2.6	2.1
10201	-0.4	-0.2	1.5	1.6	0.4
10202	0.0	0.8	0.8	1.1	0.8

Table 6.16 shows the error values of the DJI Zenmuse P1 sensor’s model generated by Reality Capture. Maximum Value didn’t exceed 3.0 cm in Total Error and 2.6 cm in XY error. Based on the GCPs’ presence, the values’ accuracy is enhanced, and error deviations are low.

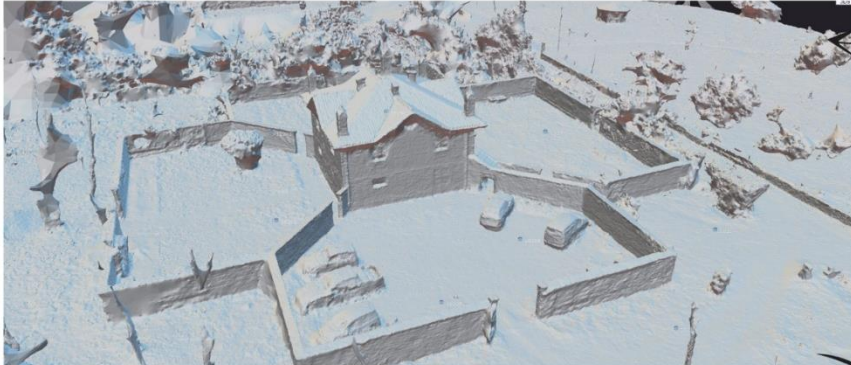


Figure 6. 12 Orthoprojection image of DJI Zenmuse P1 processed by Reality Capture

Sparse Cloud of the P1 Sensor created in Reality Capture



Model Mesh of the P1 Sensor created in Reality Capture



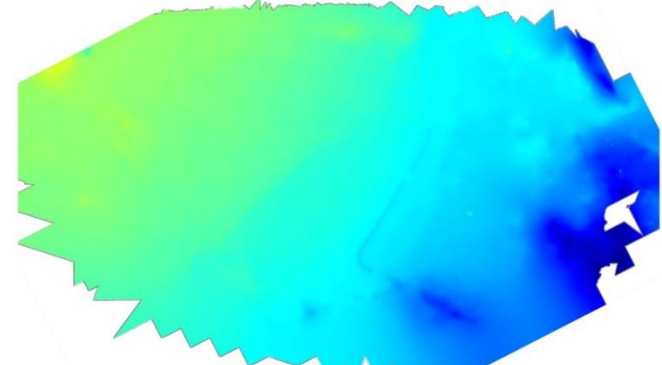
Textured Model of the P1 Sensor generated in Reality Capture



Seamlines of Villa Ghia model performed with P1 sensor



Digital Terrain Model of Villa Ghia performed with P1 sensor



Digital Surface Model of Villa Ghia performed with P1 sensor

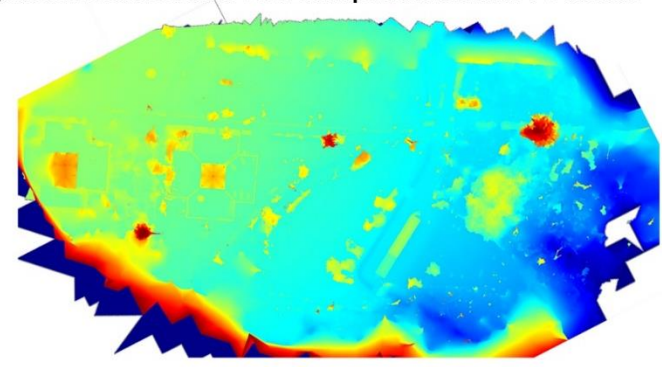


Figure 6. 13 Workflow steps, Model's seamlines, and Digital Elevation Model of DJI Zenmuse P1's model in Villa Ghia generated by Reality Capture

6.2.3. Villa Ghia DJI Zenmuse L1 - Metashape

In data collection, 140 images were captured with the DJI Zenmuse L1 camera sensor from a flight altitude of approximately 52.4 m. While doing the alignment, 126 images successfully formed the model cloud. The created model covers an area of approximately 0.04 km². There are 88,610 tie points in the sparse cloud created due to the alignment. In the medium quality and mild filtering mode, 17,662,955 points were created in the dense point cloud and 1,177,525 faces in the model. The ground resolution of the model was calculated as 1.51 cm/pix, and the Reprojection error was calculated as 0.698 pix. After the dense cloud was created, build mesh, texturize, build DEM, and Orthoprojection stages were performed, respectively.

Table 6. 17 GCPs value of the Zenmuse L1 sensor in the Villa Ghia case study created by Metashape

Label	X error (cm)	Y error (cm)	Z error (cm)	Total Error (cm)	XY Error (cm)
2000	-1.9	-0.5	0.7	2.1	2.0
2002	-1.6	0.0	-2.0	2.6	1.6
2003	-2.5	2.8	2.6	4.5	3.7
2005	1.7	4.7	1.7	5.3	5.1
2011	0.3	1.9	3.6	4.1	1.9
2012	2.5	0.2	1.5	2.9	2.5
10203	0.0	-0.5	3.3	3.3	0.5
10205	1.0	1.8	5.3	5.7	2.1
10208	1.0	0.7	1.0	1.6	1.2
10212	-1.4	1.2	0.6	2.0	1.9
10213	-0.5	1.0	-0.3	1.1	1.1
10214	0.3	1.6	-1.7	2.4	1.7
Check Points					
2001	0.1	-0.8	-3.2	3.3	0.8
2004	-1.2	-1.3	-1.3	2.1	1.7
10201	-1.0	1.0	-0.8	1.6	1.4
10202	-1.3	0.0	0.6	1.5	1.3

Table 6.17 shows the error values of the DJI Zenmuse L1 sensor acquired from the Villa Ghia survey created by Agisoft Metashape. The Total Error-values are mostly low based on the increased accuracy due to the GCPs. Total Error is between 1.5 to 7.7 cm except for the “2008” GCP label which is a 15.8 cm error value.



Figure 6. 14 Orthoprojection image of DJI Zenmuse L1 processed by Metashape



Figure 6. 15 Orthoprojection image of DJI Zenmuse L1 processed by Reality Capture

6.2.4. Villa Ghia DJI Zenmuse L1–Reality Capture

In data acquisition, 140 images were acquired with the L1 sensor. During the alignment of the images, 116 of these photos were successfully matched in Reality Capture. The model was aligned with the medium image quality render option, the Brown4 with tangential2 lens

parameter, and the downscale factor of 4. The area of the resulting terrain model is approximately 0.27 km², and the number of key points of the sparse cloud is 68,564. Mass and texture were created in the render with the downscale factor of 4. Finally, "True ortho from a textured model" was chosen as the rendering method in Orthoprojection, and the ortho pixel size was determined as 0.003. The mean reproduction error for the L1 sensor is 1.19 pixels.

Table 6. 18 GCPs value of the L1 sensor in the Villa Ghia case study created by Reality Capture

Label	X error (cm)	Y error (cm)	Z error (cm)	Total Error (cm)	XY Error (cm)
2000	-0.1	-0.7	-1.7	1.8	0.7
2002	0.8	-0.3	1.4	1.6	0.9
2003	0.8	-0.7	0.3	1.1	1.1
2005	0.1	-1.7	-1.7	2.4	1.7
2011	0.3	0.5	0.0	0.6	0.6
2012	-1.8	0.4	-1.0	2.1	1.8
10203	0.3	0.2	0.2	0.4	0.4
10205	-0.2	-0.5	-0.6	0.8	0.5
10208	-0.3	0.4	0.2	0.5	0.5
10212	0.5	-0.6	-0.2	0.8	0.8
10213	1.0	0.6	0.4	1.2	1.2
10214	-0.5	0.2	0.4	0.7	0.5
Check Point					
2001	0.1	-1.0	0.4	1.1	1
2004	3.1	-0.3	-1.8	3.6	3.1
10201	2.0	0.5	0.1	2.1	2.1
10202	0.6	0.9	0.5	1.2	1.1

Table 6.18. displays the model's total error, XY error, and error in X, Y, and Z axes. Among the GCPs, the highest error value is 2.4 cm from label 2005 and the GCP errors show an alteration between 0.8 to 2.4 cm.

6.2.5. Villa Ghia DJI Phantom 4 RTK - Metashape

In Villa Ghia, a DJI Phantom 4 RTK drone and camera sensor flew at 49.5 m altitude to collect data; 498 images in both vertical and oblique orientation were obtained during the flight. For the alignment process, 475 of these images were successfully used to construct the model,

and the area of the generated terrain model is 0.05 km². The alignment process was completed with a sparse cloud with 278,851 tie points. A dense cloud with 32,491,270 points is created with medium quality and mild filtering mode, and the model has 2,166,058 faces. The ground resolution of the generated cloud is 1.48 cm/pix, the reprojection error is 1.08 pix, and the projection number in the model is 824,186.

Table 6. 19 GCPs value of the Phantom 4 RTK sensor in the Villa Ghia case study created by Metashape

Label	X error (cm)	Y error (cm)	Z error (cm)	Total Error (cm)	XY Error (cm)
2000	-1.4	0.6	1.6	2.2	1.6
2002	-0.5	-0.8	-2.0	2.2	0.9
2003	-0.9	1.1	-1.9	2.4	1.5
2005	1.5	2.5	1.6	3.3	2.9
2011	-0.1	-0.3	-0.5	0.6	0.3
2012	3.1	-1.1	0.4	3.3	3.2
10203	-1.5	-0.4	0.4	1.6	1.6
10205	-0.4	0.8	0.6	1.0	0.8
10208	0.1	-1.4	-2.0	2.5	1.4
10212	-0.8	-1.4	-1.2	2.0	1.6
10213	0.2	-0.9	-0.8	1.2	0.9
10214	1.3	1.0	0.7	1.8	1.7
Check Points					
2001	0.1	-0.8	-3.2	3.3	3.3
2004	-1.2	-1.3	-1.3	2.1	2.1
10201	-1.0	1.0	-0.8	1.6	1.6
10202	-1.3	0.0	0.6	1.5	1.5

Table 6.19 contains the error values of the Villa Ghia model generated by the images of the Phantom 4 RTK sensor. The total error value is not high and ranges between 0.6 and 3.3 cm. The highest error value is found in the 2005 and 2012 labels and the error is 3.3 cm.



Figure 6. 16 Orthorectification image of DJI Phantom 4 RTK processed by Metashape



Figure 6. 17 Orthorectification image of DJI Phantom 4 RTK processed by Reality Capture

6.2.6. Villa Ghia DJI Phantom 4 RTK– Reality Capture

To capture the images with the aerial photogrammetry technique in Villa Ghia, 498 images were acquired with the Phantom sensor. During the alignment of the images, 421 of these photos were successfully matched in Reality Capture. As applied in the other sensors, the model was aligned with the medium image quality render option, the Brown4 with tangential2 lens parameter, and the downscale factor of 4. The model's terrain surface is approximately 0.39 km², and the number of key points of the sparse cloud was 169,370. Mass and texture were created in the render with the downscale factor of 4. Lastly, "True ortho from a textured model" was chosen as the rendering method in Orthoprojection, and the ortho pixel size was determined as 0.004. The mean reproduction error for the Phantom sensor is 1.34 pixels.

Table 6. 20 GCPs value of the Phantom sensor in the Villa Ghia case study created by Reality Capture

Label	X error (m)	Y error (m)	Z error (m)	Total Error (m)	XY Error (m)
2000	0.006	-0.004	-0.010	0.012	0.007
2002	0.008	0.005	0.019	0.021	0.009
2003	0.008	-0.007	0.007	0.013	0.011
2005	-0.006	-0.019	-0.014	0.024	0.020
2011	0.005	0.005	0.001	0.007	0.007
2012	-0.021	0.01	-0.01	0.025	0.023
10203	0.003	0.003	0.008	0.009	0.004
10205	-0.002	-0.007	-0.006	0.009	0.007
10208	-0.001	0.010	0.024	0.026	0.010
10212	0.011	0.008	0.010	0.017	0.014
10213	0.001	0.006	0.016	0.017	0.006
10214	-0.010	-0.008	0.017	0.021	0.013
Check Points					
10201	0.01	0.00	0.04	0.04	0.01
10202	0.01	0.01	0.02	0.02	0.01
2001	0.00	0.00	0.03	0.03	0.00
2004	0.02	0.01	0.01	0.03	0.02

Table 6.20 show the GCP error values of the Phantom sensor generated by Reality Capture. The values were distributed homogenously in Control Points between 0.9 cm to 2.6 cm for the total. The values are quite low, and the peak total error value is in the label 10208 with 2.6 cm.

6.3. Cloud-to-Cloud Distance Analysis Results

Cloud-to-cloud distance analysis was performed to calculate the distance of the nearest neighbor point between two cloud models and to classify the distance between them. Initially, the area of the main object for which the distance of the cloud models is to be computed is determined. This area is marked in both models with the segmentation option and cut with the segment in option. In this way, unnecessary calculation of undesirable areas was prevented, and the points where the images are low, and the accuracy is not precise are prevented from reducing the accuracy of the model. Of the two models, the model with more resolution and number of points was chosen as a reference. Thus, DJI Zenmuse P1 was determined as the reference cloud model, and the distance analysis was performed with DJI Phantom 4 RTK and DJI Zenmuse L1 as the compared models, respectively. The maximum distance of 0.05 m was accepted as the calculation parameter, and the distance analysis of the clouds was carried out with this value.



Figure 6.15. Specification and cut of the model area with Segment In option for the C2C distance analysis in CloudCompare.

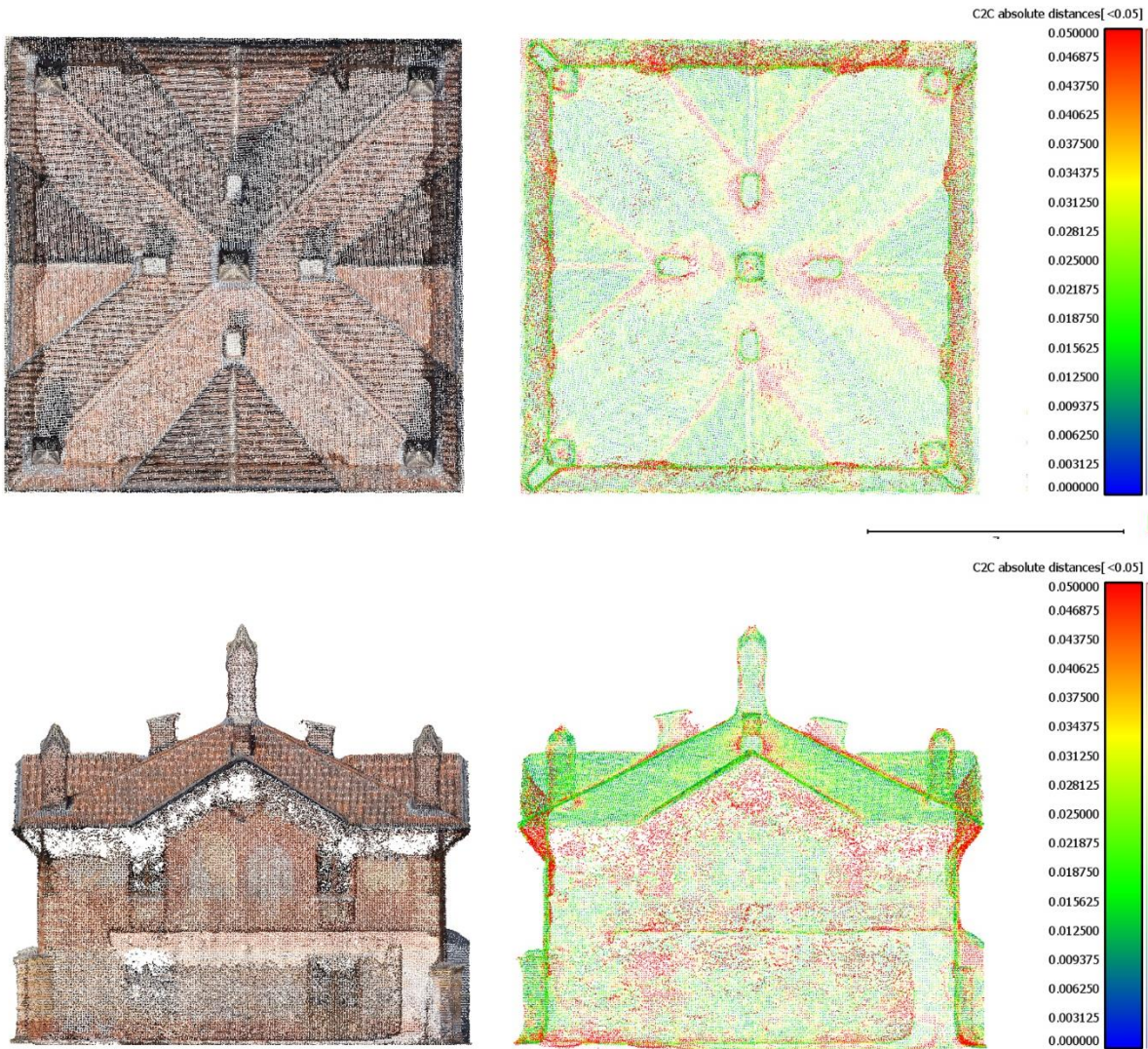


Figure 6. 18 Cloud-to-cloud (C2C) Distance of DJI Zenmuse P1 and DJI Phantom 4 RTK Sensors generated by Metashape cloud model

The roof and façade between the DJI Zenmuse P1 and DJI Phantom 4 RTK sensors show the cloud-to-cloud distance. DJI Zenmuse P1 is the reference, and the DJI Phantom 4 RTK is the compared sensor in this computation. Since the images of the model were taken from an aerial survey, the section just underneath the roof could not be created clear in the two cloud models. Therefore, in the distance comparison of the two models, the most significant distance differences were found on the red color scale. Especially on facades in the shade and with structures such as balconies, the point distances between the two models are excessive because the information cannot be entirely obtained during the measurement. Therefore, the model was calculated in software with red dots indicating high distance matching.

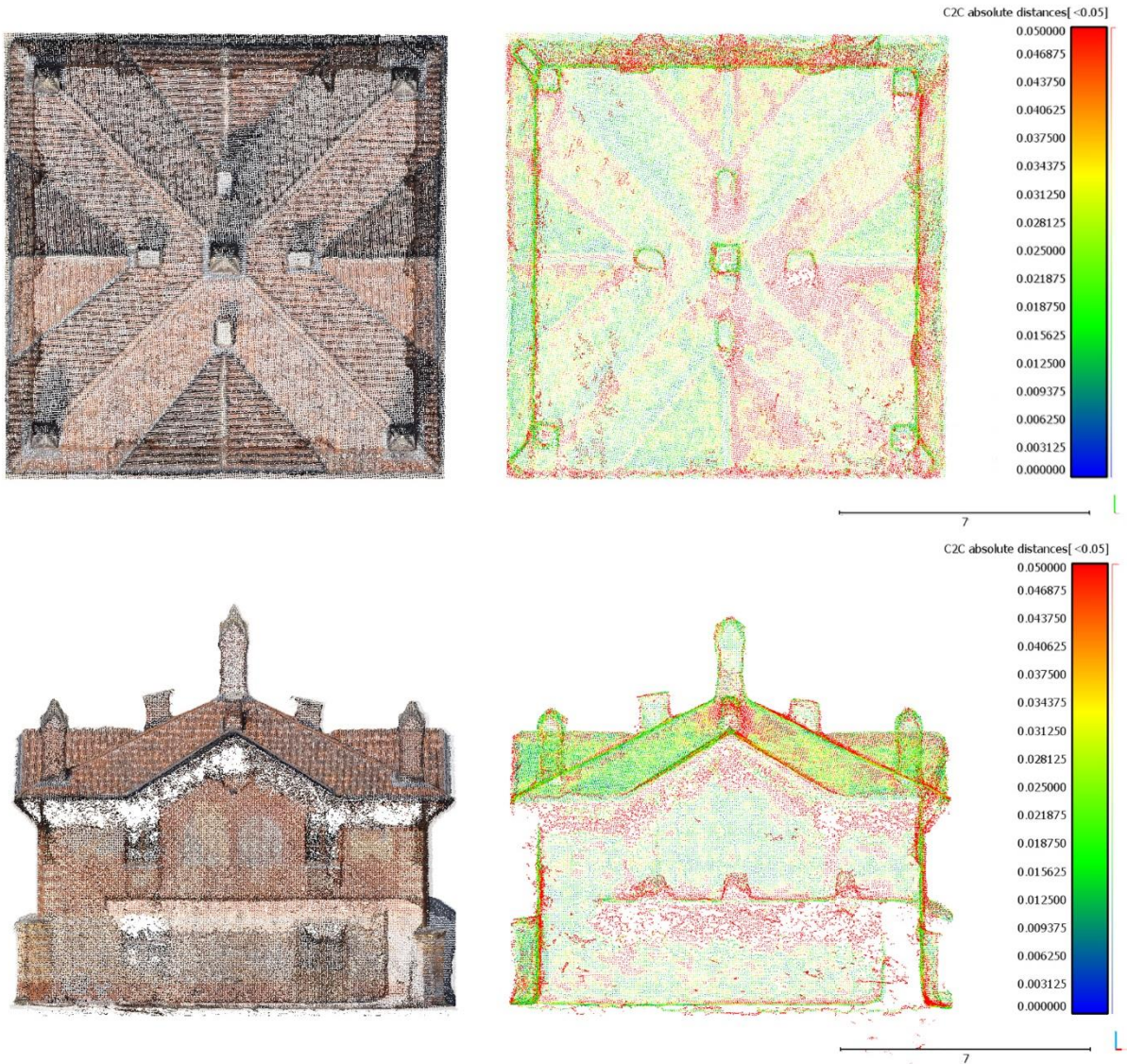


Figure 6. 19 The Cloud-to-cloud Distance computation of DJI Zenmuse P1 and DJI Zenmuse L1 sensors generated by Metashape cloud

The cloud-to-cloud distance analysis of the roof and façade of the DJI Zenmuse P1 and DJI Zenmuse L1 sensor comparison. Compared to the P1 and DJI Phantom 4 RTK analysis in figure 6.15., the point matching distance of the cloud models, especially on the roof, is much larger. In the P1-Phantom distance comparison, the point distance range of the lower right part of the roof matched around 2 cm, while the distance comparison was above 5cm in the P1-L1 distance comparison.

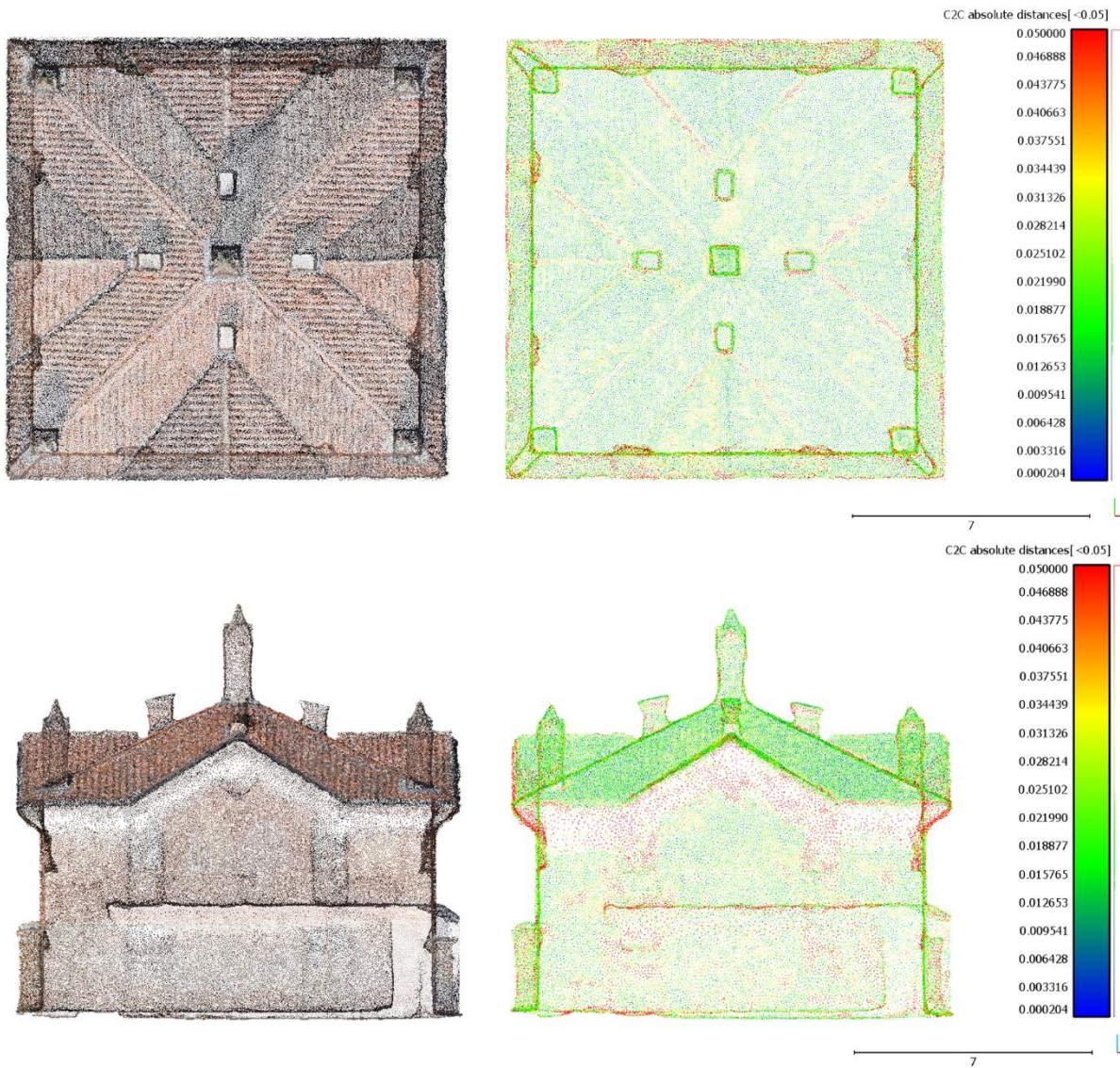


Figure 6.20 Cloud-to-cloud (C2C) Distance of Zenmuse P1 and Phantom 4 RTK Sensors generated by Reality Capture cloud model

The DJI Zenmuse P1 and DJI Phantom 4 RTK sensors' cloud-to-cloud (C2C) distance computation is demonstrated. When the distance comparison was processed for P1 and Phantom sensors in both software, Reality Capture's cloud points were distributed more homogeneously than Metashape. The difference in both software is evident, especially along the edges and façade of the Villa. Except for the eaves and the parts underneath the roof and balcony, the distribution of the cloud points computation matched around 2 cm along the entire façade, which is considered a good result.

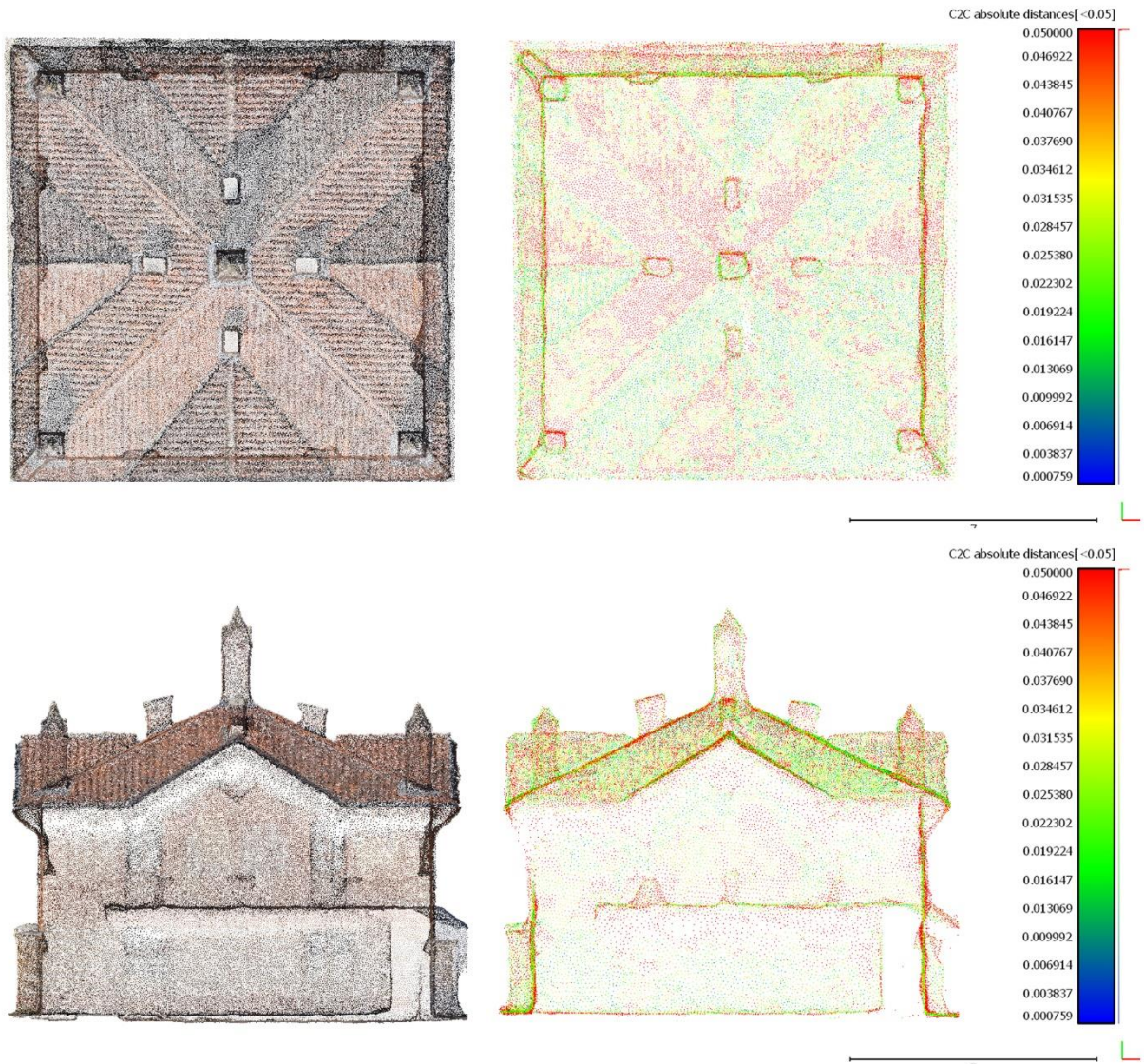


Figure 6. 21 The Cloud-to-cloud Distance computation of Zenmuse P1 and Zenmuse L1 sensors generated by the Reality Capture cloud

The cloud-to-cloud distance of the roof and façade between the DJI Zenmuse P1 and DJI Zenmuse L1 sensors. Models provided by two different software are compared with the same analysis; the distribution of compared distance points with more than 5 centimeters difference are more homogeneous in Reality Capture, while the same points were more concentrated in specific locations in Metashape.

6.4. Density Analysis Results

Table 6. 21 The models' Surface Density Analysis generated by CloudCompare

Surface Density (A=5x5 m, r=1)	Cloud Size [n. pts]	Mean [n. pts]	Std. Deviation [n. pts]
DJI Zenmuse P1 M.	62,480	1205.03	556.28
DJI Phantom 4 RTK M.	12,908	293.05	111.64
DJI Zenmuse L1 M.	9,708	296.33	88.18
DJI Zenmuse P1 R.C.	37,020	968.97	226.86
DJI Phantom 4 RTK R.C.	9,578	260.397	70.32
DJI Zenmuse L1 R.C.	7,751	206.07	53.43

Table 6.21.: The surface density analysis was generated on the sensors and software with 5m x 5m area. The number of neighbors of these three sensors indicates that DJI Zenmuse P1 has the most significant number of neighbors compared to the other sensors. Moreover, the number of neighbors of the DJI Phantom 4 RTK and Zenmuse L1 are similar, but DJI Phantom RTK is slightly greater. On the other hand, the results of Metashape are twice as much as Reality Capture's results.

Table 6. 22 The Volume Density analysis of three different sensors generated in two different software.

Volume Density (A=5x5 m, r=1)	Cloud Size [n. pts]	Mean [n. pts]	Std. Deviation [n. pts]
DJI Zenmuse P1 M.	62,480	903.77	417.20
DJI Phantom 4 RTK M.	12,908	219.79	83.73
DJI Zenmuse L1 M.	9,708	222.25	66.13
DJI Zenmuse P1 R.C.	37,020	726.68	170.15
DJI Phantom 4 RTK R.C.	9,578	195.30	52.74
DJI Zenmuse L1 R.C.	7,751	154.55	40.07

Table 6. 22 shows the Volume and Surface Density analysis of the Villa Ghia survey's models generated by Metashape and Reality Capture. According to sensor resolution and pixel size, the greatest cloud size, mean points, and standard deviation belong to the DJI Zenmuse P1 sensor. DJI Phantom 4 RTK and DJI Zenmuse L1 show close characteristics and results.

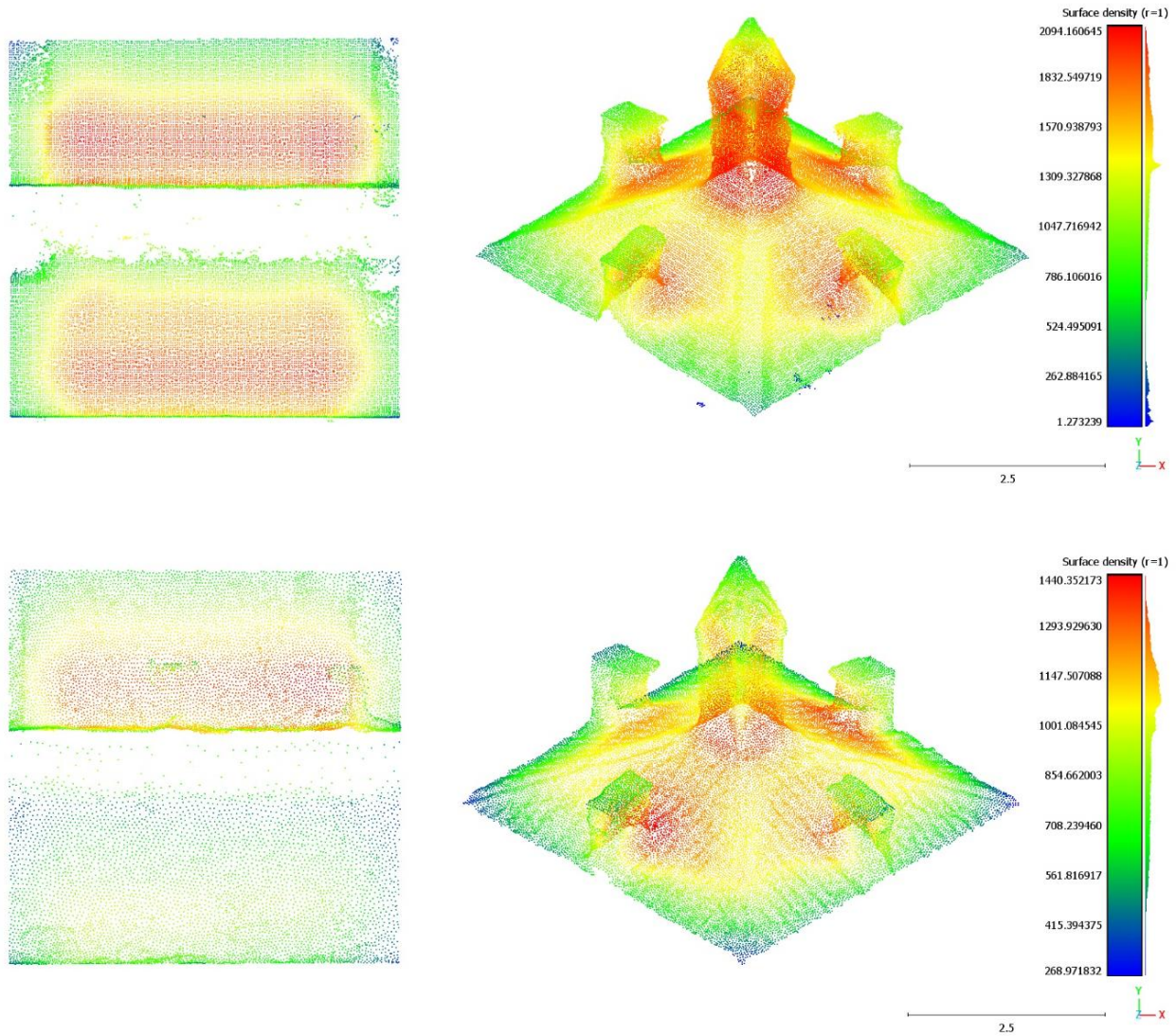


Figure 6. 22 the DJI Zenmuse P1 Sensor's Cloud Density analyses.

The cloud above belongs to the model provided by Metashape, while the image below represents the Reality Capture. When considering Metashape's cloud model (2094.1), the density is distributed more homogeneously and is twice as dense as Reality Capture's model (1440.) along the building. Specifically, the chimney of the Metashape cloud model has the densest and most visible structure all along the sensors. On the contrary, when the rooftops are compared between the two software, the Reality Capture model is much denser than the Metashape model.

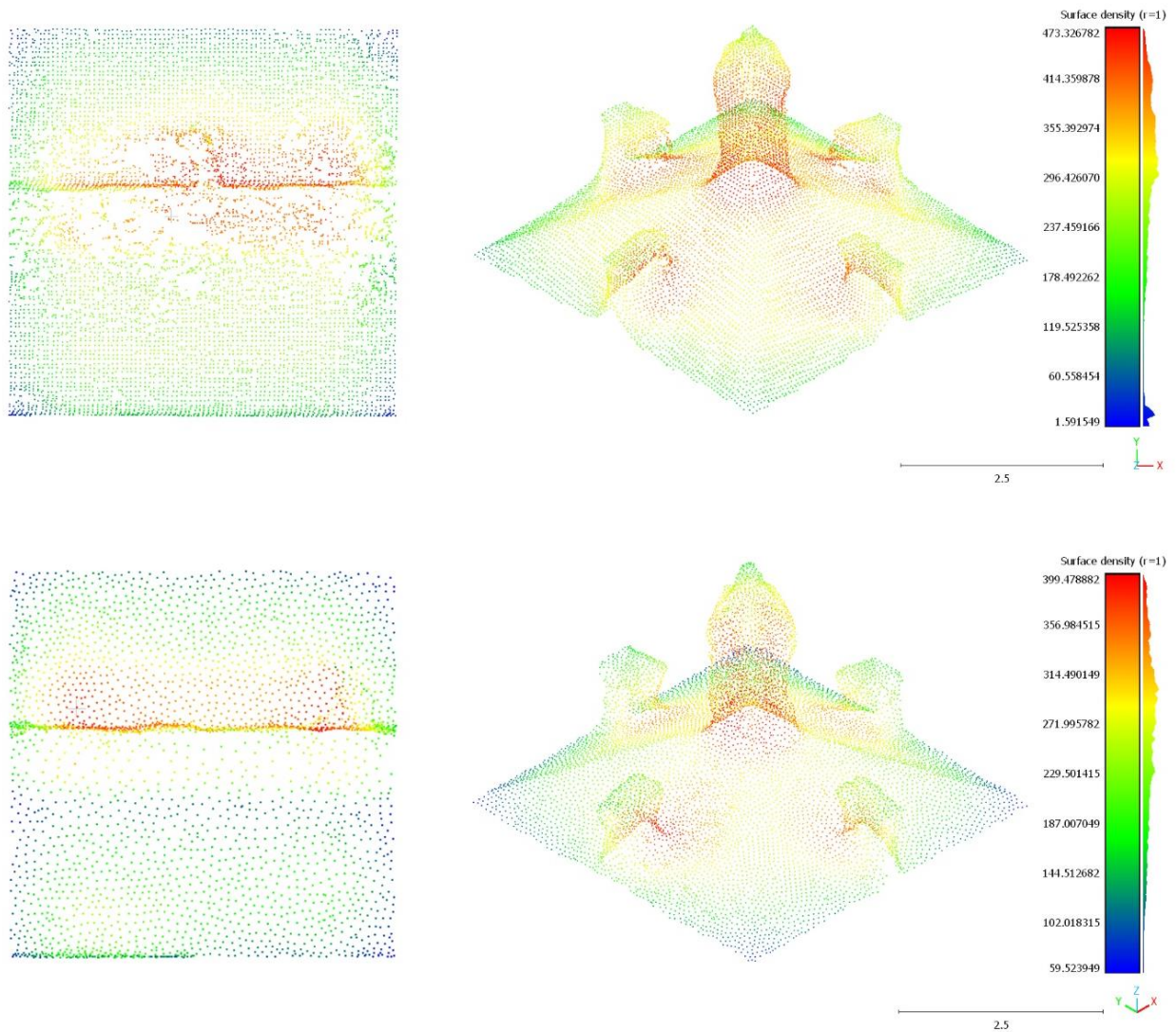


Figure 6. 23 the density analyses of the DJI Phantom 4 RTK sensor from the Metashape and Reality Capture (The model above – Metashape, the model below – Reality Capture).

The density of the cloud model of Metashape (473.32) is slightly greater than Reality Capture (399.47) for DJI Phantom 4 RTK. Especially underneath the roof, and the edges of the building in the model below seem to be sparse. Due to the aerial image acquisition, the rooftops are denser when they are compared with the distribution of the cloud model in the façade of the Villa.

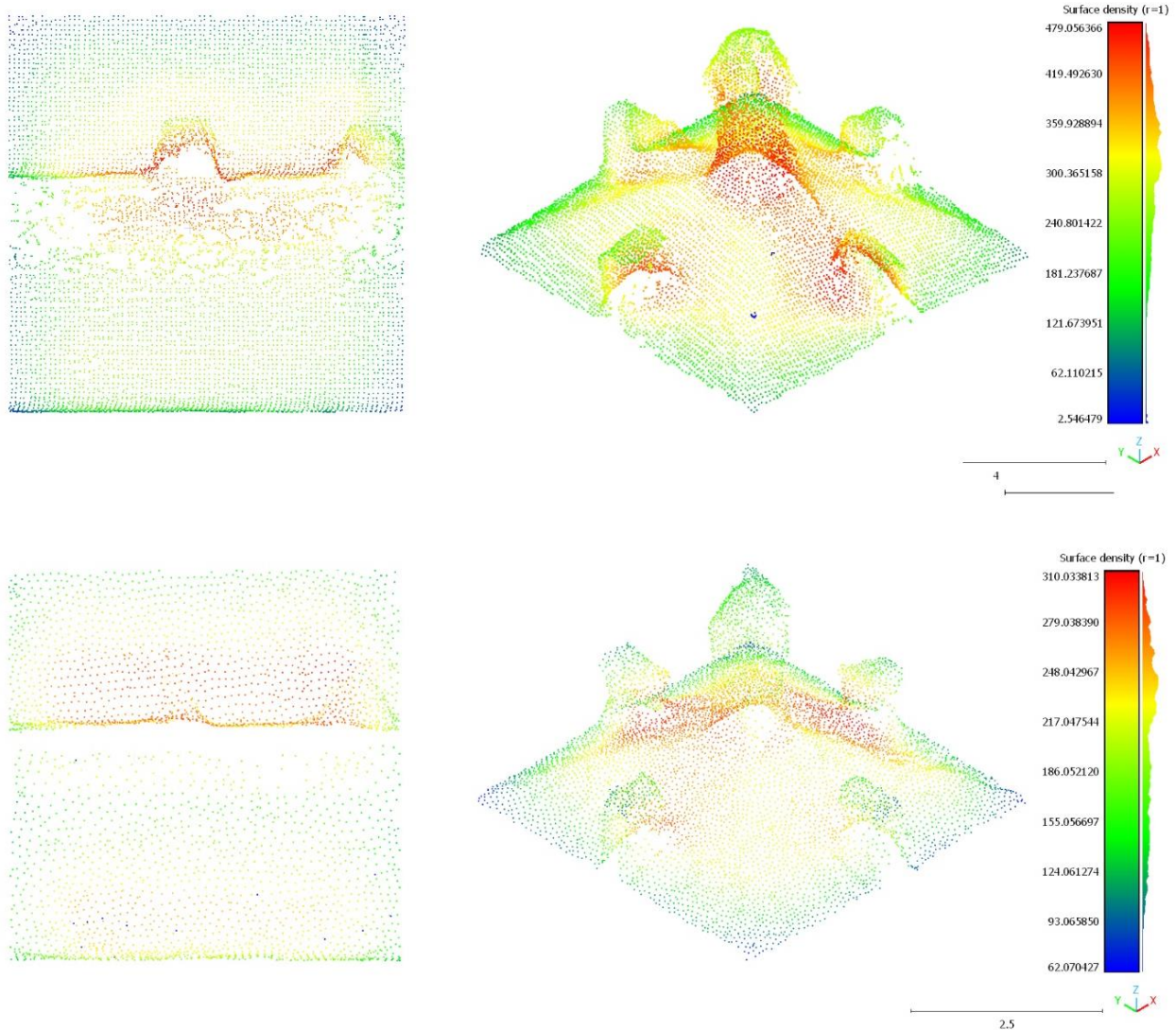


Figure 6. 24 the DJI Zenmuse L1 Sensor's Cloud Density analyses.

The cloud above belongs to the model of the DJI Zenmuse L1 sensor provided by Metashape, while the image below represents the Reality Capture. As seen in both software clouds, the computation of the model is not defined in specific regions of the building. Especially underneath the balcony of the Villa couldn't be generated by the software due to the acquired image taken aerial and these parts are out of sight. The density of the rooftop is higher than the facades of both models because the aerial image acquisition includes the top side of the objects. The computed surface density analysis with a radius of 1 meter showed that with the same images and information, Metashape's cloud model (479.05) is about 1.5 times denser than the Reality Capture model (310.03) which renders the model more visible and understandable in CloudCompare.

7. Discussion & Conclusion

Chapter 1 of this thesis discussed the use of UAVs to generate 3D models of the image-acquired case study at the Northumberland, U.K. Benchmark. In this study, the results of the 3D models produced by the software of the three sensors used for image acquisition were compared among themselves. The photogrammetric data processing and workflow were learned in the Benchmark study. Then the second case study with the same sensors was performed in Veneria Reale, Italy. Villa Ghia. Thus, it was possible to use and apply the methods and data processing techniques learned in the Benchmark case study from the beginning to the end of the Villa Ghia study. The precision and accuracy of the produced models were compared, and then the criteria such as data collection, labor, and time of the produced models were evaluated, and the results were examined for cost-benefit-gain.

Chapter 2 concerns the historical development of UAV photogrammetry, its applications, documentation, and the characteristics of the tools used during the survey. It provides a perspective to understand the working principles and methods of equipment used in data acquisition and describes the calibration parameters that need to be adjusted to improve the accuracy and precision when acquiring data.

Chapter 3 contains geographic and historical overviews and illustrations of the sites. Chapter 4 describes the methods considered during data acquisition, the specific features of drones and cameras that record images, and a comparison. Chapter 5 discusses the post-processing workflow of the collected data in model production using Agisoft Metashape and Reality Capture, and then detailed cloud analysis of these produced models using CloudCompare.

Chapter 6 includes analyzing the results of models from different sensors and software. These analyzes show the production parameters of products such as mesh, texture, dense cloud, DEM, Orthoprojection, the numerical values of the results, their resolution, the accuracy of ground control points, and camera locations.

7.1. Discussion

7.1.1. Benchmark – DJI Zenmuse P1

The DJI Zenmuse P1 sensor has the highest resolution and accuracy in the study. In addition to being the most significant and high-resolution model created among the sensors, it also has a long run time and heavy file sizes (Approximately 80 GB). The size of each captured image is between 18-22MB. Therefore, in cases where the hardware used is insufficient and low, heavy operations such as Orthoprojection production are performed on Agisoft Metashape's servers with the cloud processing feature, which is valid in versions after 1.5 of Agisoft Metashape. Because the DJI Zenmuse P1 has high ground resolution and projection, the reprojection error is higher than other sensors. (Table 6.4.) Since there is no vegetation in the benchmark study area, the Digital Terrain Model (DTM) was produced successfully and the map color difference resulting from the elevation difference can be seen very clearly. While the error of the camera images was low in the raw data, which was the first phase, it was larger as it was realigned with the import of the Ground Control Points to be closer to the actual result. By importing the coordinates of the Ground Control Points and realigning the model, ground control point errors decreased to the lowest error value (about 20% of the first stage) in Phase 3.

7.1.2. Benchmark – DJI PHANTOM 4 RTK

The images were acquired with the DJI Phantom 4 RTK drone and camera sensor. Because it does not have a very high resolution and like the DJI Zenmuse P1, the resolution and projection number of the model created were lower. Compared to P1, the processing time was much shorter, and cloud processing was not needed as the processes were not heavy. Each image obtained during the survey is approximately 8 MB in size. It had the lowest camera location total error in all three phases among the three sensors. In GCP sensor error, it had the highest error value among these three sensors. Although the ground resolution is roughly the same as the L1 sensor, the projection number is about twice that. Despite the successful creation of the DEM, the elevation values of the pit in the quarry did not give much detail compared to the DJI Zenmuse P1 sensor and remained in the same color tone of blue. With the import of the ground control points in the 3rd phase, there was a very high decrease in the error rate in the model and a more accurate and accurate result emerged.

7.1.3. Benchmark - DJI Zenmuse L1

The DJI Zenmuse L1 sensor is the only LIDAR sensor among these three sensors and has approximately the same camera features as the DJI Phantom 4 RTK. Therefore, the durations of the data processing phases were close to each other. There wasn't any fluctuation in the error results. The sparse cloud produced is less frequent than the others. The resolution values in the produced Orthoprojection have a slightly higher resolution than the Phantom sensor's model. However, because the acquired images with the DJI Zenmuse L1 were inclined, the resolution of the individual image remained very low, and when marking ground control points on the software for realignment, these reference points were much more difficult to find than with other sensors.

7.1.4. Villa Ghia – Metashape DJI Zenmuse P1

The model was created with 897 images recorded during the Villa Ghia survey with the DJI Zenmuse P1 sensor. Although the number of captured images was 897, only 789 images were used to generate the model since the site was surrounded by vegetation. Due to the high image quality and the high number of images the processes such as alignment, dense cloud creation, mesh, texturize, dem, and Orthoprojection were made with cloud processing. The size of the resulting project was approximately 80 GB, as in the Benchmark project. Undefined images mostly coincide with the area of vegetation and can be viewed from the resulting Orthoprojection. Since the ground control points are imported, the results of the created model are more accurate and accurate, and the error deviation is at most 2.5 cm. These values are roughly the same for all three sensors in Villa Ghia. Unlike Benchmark, since there is an additional historical building on this land, not only the Digital Terrain Model but also the Digital Surface model was produced in all Villa Ghia sensors.

7.1.5. Villa Ghia Metashape – DJI Phantom 4 RTK

Although 498 images were obtained in the survey to create the model, 475 of these images were defined in the software. Unidentified images still cover the wooded area, as with the DJI Zenmuse P1 sensor. Since the image resolution is lower than the P1 sensor, all workflow stages are performed much faster. Although it has the approximate DEM resolution value as the

DJI Zenmuse L1 sensor, it is much more than the Dense Point Cloud, Tie points, and polygon faces L1 sensor in the model. The Phantom sensor has the lowest margin of error as GCP sensor errors, with a Total Error of 2.11 cm. The produced Orthoprojection image and Digital Elevation model are close to the model of the P1 sensor in terms of resolution.

7.1.6. Villa Ghia Metashape – DJI Zenmuse L1

The DJI Zenmuse L1 sensor captured 140 images during field data acquisition. In total 126 images were successfully used to create the Cloud Model. During the survey, images were mostly obtained at an oblique angle. Therefore, the generated model is not as successful as the DJI Zenmuse P1 and DJI Phantom 4 RTK models. With the import of Ground Control Points, the total error increased to 2.65 cm. With this value, the DJI Zenmuse L1 was the sensor with the highest Total Error. Since the created Digital Elevation Model and Orthoprojection do not have a homogeneous and rectangular shape like other sensors, it can be said that DJI Zenmuse L1 has the unstable result among these three sensors. Advantageously, the DJI Zenmuse L1 was the sensor most clearly defined by the vegetation when creating the DEM, as the flight was performed at an inclined angle.

7.1.7. Villa Ghia Reality Capture DJI Zenmuse P1

Images of the P1 sensor used in Metashape were also used in Reality Capture. During the survey, 897 images were acquired. The number of images that were successful for alignment is 637. In the alignment setting with the medium rendering parameter, the processing time was much shorter than the processing time in the Metashape software. It was seen that the number of tie points and projections is more than the Metashape model. The model is produced in software with options for alignment, mesh, texturize, and Orthoprojection. Unlike Metashape, there is no individual phase like building a Dense Cloud, but the Dense Cloud is created together with Mesh. With the transfer of Ground Control Points to the model, XY error and Total Error results were precise and accurate. When compared with Metashape, ground control point errors were observed to be much lower. When the Orthoprojection was rendered from the textured model, it could not successfully process the areas where the vegetation coincides. However, this method was necessary to generate the buildings and artifacts on the surface in Orthoprojection. The

Orthoprojection was rendered with the "image mosaicing (aerial)" option and the vegetation was perfectly transferred to the Orthoprojection, but the distortions were observed on the roofs of the buildings with that parameter.

7.1.8. Villa Ghia Reality Capture DJI Phantom 4 RTK

The total number of images acquired was 498. During the alignment, 421 images were rendered successfully. The processing time was completed in a short time due to the parameters of the software and the image resolution not being very high. Although the Orthophoto of the model was not as successful as the Zenmuse P1, the deterioration in the vegetation part draws attention. The XY Error of the ground control points is 0.9 cm, and the Total Error is 1.2 cm.

7.1.9. Villa Ghia Reality Capture Zenmuse L1

The DJI Zenmuse L1 sensor acquired 140 images and 114 images matched for alignment in Reality Capture. It is the sensor with the least size and model values among these three sensors. Although the Orthoprojection was rendered from the Textured Model, the high distortion was detected on the Ciabot's roof. Since the images are acquired inclined, the vegetation in the Orthoprojection is relatively more distinct than the models of other sensors. The XY Error of the Ground Control Points is computed as 1 cm, and the Total Error is 1.5 cm.

7.2. Limitations of the UAV Photogrammetry Technology

Three critical factors limit the potential of UAV surveying techniques. These are time, data size, and access. The last limitation is addressed to the exchange of the processed and raw data between the different disciplines and professionals. It also concerns accessing this data by the public.

Time is of great importance. In camera and drone systems, suitable drones for the working area and high battery capacity affect the time spent in the survey. To process the acquired site images and information in a shorter time and with high quality, new and high processing capacity computer equipment should be acquired. Considering that, the time devoted to a photogrammetric measurement does not only belong to post-processing and Model

Generation. It has many components such as calibrating the GNSS system, making necessary adjustments to the drone before the flight, creating a flight path, collecting aerial images, and improving the obtained images before processing.

In addition, the generated models in Metashape and Reality Capture are exported to other software for the measurement of analyzes such as density, accuracy, and distance calculations. It shows that besides post-processing, there are many other steps, and they must be done in a sequence, and time is needed for this.

The field data acquisition time is not known as the benchmark image data is uploaded into the system. Data acquisition for DJI Zenmuse L1 and DJI Phantom 4 RTK took approximately one hour each for the aerial survey conducted at Villa Ghia on April 11, 22. Since the number of images collected in the DJI Zenmuse P1 sensor is also high, data was obtained with this sensor between 1.5-2 hours.

Data Size: The field data acquisition time is not known as the benchmark image data is loaded into the system ready. Data acquisition for DJI Zenmuse L1 and DJI Phantom 4 RTK took approximately one hour each for the aerial survey conducted at Villa Ghia on April 11, 22. Since the number of images collected in the DJI Zenmuse P1 sensor is also high, data was obtained with this sensor between 1.5-2 hours.

Table 7. 1 Storage size of the models

Sensor & Phase	Image Size (GB)	Model size (GB)	Total (GB)
Benchmark-1 P1	21	79.8	100.8
Benchmark-1 L1	4.3	6.1	10.4
Benchmark-1 Phantom	4.0	10	14
Benchmark-2 P1	-	52.1	52.1
Benchmark-2 L1	-	0.1	0.1
Benchmark-2 Phantom	-	0.1	0.1
Benchmark-3 P1	21	79.3	100.3
Benchmark-3 L1	5.8	10.2	16
Benchmark-3 Phantom	4.1	15.6	19.7
Villa Ghia P1	20.9	43.1	64
Villa Ghia L1	2.5	3.2	5.7
Villa Ghia Phantom	4.0	9.4	13.4
Villa Ghia P1 R.C.	-	20.7	20.7
Villa Ghia L1 R.C.	-	6.0	6.0
Villa Ghia Phantom R.C.	-	5.3	5.3
CloudCompare	-	12.0	12.0
Total			440.6

Table 7.1 shows the size of the Benchmark and Villa Ghia case studies for the generation of their models. The area covered by the models produced with medium quality parameters is approximately 440 GB. As can be seen from the table, high-capacity memories or internet storage areas such as the cloud are required for photogrammetric processes.

Access: Finally, we can examine access in two different categories. As the first factor, problems may arise in sending and storing high-capacity models and projects by professionals. Secondly, the models produced are difficult to upload except for a few 3D model websites, and the results of most studies are not easily accessible by the public in terms of data privacy.

7.3. Future Research

As shown in this thesis, not every camera sensor is optimal for the architectural space. It must be remembered that the ground may not be seen, especially in studies involving densely wooded areas, and the image acquisition cannot be achieved clearly due to the angles where

vegetation is dense. Another consideration is the use of a camera sensor with a resolution that can define the details of the architectural elements in the area. For example, in some cases the DJI Zenmuse L1 camera sensor was not unable to capture the Ground Control Points and architectural details, which are references placed in the field, in the images, resulting in loss of time when making markings and degrading the quality of the model.

Another consideration will be the determination of the season and environmental conditions in which the survey will be carried out. For example, in areas with heavy vegetation, in summer, trees may increase in volume due to their leaves and shade the architectural elements or the snow covers the site in winter and causes unexpected results. In addition, the time-of-day image acquisition should be well determined. If the sun is at an opposite angle, it means that it reflects during image acquisition and the images lose their clarity.

Flight at low altitudes is not preferred in terrain surveys as it makes it difficult to determine the topography and to define areas with dense vegetation and trees. However, in architectural sites, the low-altitude flight is preferred to capture images that will create a higher ground resolution, provide multiple overlaps between these images, and allow multi-viewing. In slow-speed image acquisition, distortions can be reduced and the images' precision can be improved.

7.4. Conclusion

In this thesis, we evaluated the combined results of the UAV photogrammetry. Firstly, we created a 3D model of the site where the quarry is located with the ready data in the Benchmark case study. We compared the results obtained from Metashape of the models we created the models using the raw data, the data processed with GNSS, and the data with increased precision and accuracy with presence of GCPs, respectively. Afterward, we got the results of UAV photogrammetry in a historical and architectural site, by processing all the stages in the Villa Ghia case study, which was done with the same sensors in Benchmark (DJI Zenmuse P1, L1, and DJI Phantom 4 RTK).

In surveyed site, the values didn't exceed XY Error 1.79 cm, and 2.65 cm Total Error, especially in both software where Ground Control Points were imported. I think that the results

of the models are accurate and acceptable. However, in terms of the reliability of the cloud model, I think that the sensor produced with the DJI Zenmuse P1 is the most precise for this study due to its resolution and the quality of the model. The model created with the DJI Phantom 4 RTK can also be used, but products such as Orthoprojection, which are created by the images obtained from the DJI Zenmuse L1 sensor, should only be used for comparison with other sensors. Especially if we assume that the results obtained from Reality Capture are accurate and the processing time is completed in a much shorter time compared to Metashape, Reality Capture will give satisfactory results in time-limited situations. On the other hand, Metashape's simple interface, detailed processing option, cloud processing and the option to use heavy models in Agisoft's database, the ability to calculate the estimated error in the absence of Ground Control Points, and the fact that it has a wider repository of information about usage on the internet are attractive. Besides, the generated reports of Reality Capture don't create a simple and all-in-one reports as Metashape. It can be exported single report such as Orthoprojection, model, Digital Surface Model etc. On the other hand, both software didn't process the vegetative area in the 3D model and Orthoprojection. When the Metashape has created a void in Orthoprojection instead of vegetation, the Reality Capture filled these undefined areas as a blurry mosaic.

The second question of the research was whether there was a cost-benefit gain by using UAV photogrammetry techniques. The answer to this question depends on factors that cannot be addressed in this study. Many factors such as the size of the site, external access, and rough topography affect the cost. Considering how long the pre-processing and post-processing stages in the acquisition of UAV data take, the price of tools and software, and that pilot training to perform aerial photogrammetry will be taken, it can be concluded that this may not always be the best method.

Although the results of this thesis are promising in some respects, they cannot give a clear answer to the two research questions I asked at the beginning. However, this does not mean that the study will not shed light on future research for UAV photogrammetry technology. I believe it will give a point of view for future runs.

As Debasish Mridha said, *"The sun enlightens everyone, but the light of knowledge enlightens those who are actively seeking the light."*

References:

- [1.] Agisoft Metashape User Manual. (2019). Agisoft. https://www.agisoft.com/pdf/metashape-pro_1_5_en.pdf
- [2.] Awange, J. L., & Kyalo Kiema, J. B. (2013). Fundamentals of Photogrammetry. *Environmental Geoinformatics*, 157–174. https://doi.org/10.1007/978-3-642-34085-7_11
- [3.] Berkowitz, S., & Cuzzi, J. (1977, November). Biostereometric analysis of surgically corrected abnormal faces. *American Journal of Orthodontics*, 72(5), 526–538. [https://doi.org/10.1016/0002-9416\(77\)90021-5](https://doi.org/10.1016/0002-9416(77)90021-5)
- [4.] Bone, E., & Bolkcom, C. (2004, August 1). *Unmanned Aerial Vehicles: Background and Issues*. Nova Science Pub Inc.
- [5.] Chiabrandò, F., Donadio, E., & Rinaudo, F. (2015, August 11). SfM for Orthophoto to Generation: A Winning Approach for Cultural Heritage Knowledge. *The International Archives of the Photogrammetry, Remote Sensing and Spatial Information Sciences*, XL-5/W7, 91–98. <https://doi.org/10.5194/isprsarchives-xl-5-w7-91-2015>
- [6.] Cullen, N. D., Verma, A. K., & Bourke, M. C. (2018, November 13). A comparison of structure from motion photogrammetry and the traversing micro-erosion meter for measuring erosion on shore platforms. *Earth Surface Dynamics*, 6(4), 1023–1039. <https://doi.org/10.5194/esurf-6-1023-2018>
- [7.] De Wulf, A. (2014, June 20). Geomatics Bachelor and Masters Program in Belgium. SGEM *International Multidisciplinary Scientific GeoConference EXPO Proceedings*. <https://doi.org/10.5593/sgem2014/b53/s22.081>
- [8.] *Anatomy of a Drone Infographic*. (n.d.). Retrieved September 10, 2022, from <https://www.dronefly.com/the-anatomy-of-a-drone>
- [9.] Geographic Information Science: Defining the Field. (2003, January 30). *Foundations of Geographic Information Science*, 9–25. <https://doi.org/10.1201/9780203009543-7>

- [10.] Eisenbeiss, H. (n.d.). *UAV Photogrammetry* [Doctoral Thesis]. ETH Zürich.
- [11.] Ekaso, D., Nex, F., & Kerle, N. (2020b, January 23). Accuracy assessment of real-time kinematics (RTK) measurements on unmanned aerial vehicles (UAV) for direct geo-referencing. *Geo-Spatial Information Science*, 23(2), 165–181. <https://doi.org/10.1080/10095020.2019.1710437>
- [12.] *Key Points Meaning*. (n.d.). Retrieved September 10, 2022, from <https://www.agisoft.com/forum/index.php?topic=9241.0#:%7E:text=A%20Tie%20Point%20is%20a,found%20common%20to%20the%20photographs.>
- [13.] Foster, S., & Halbstein, D. (2014). 3D Design and Photogrammetry. *Integrating 3D Modeling, Photogrammetry and Design*, 69–96. https://doi.org/10.1007/978-1-4471-6329-9_5
- [14.] Gomarasca, M. A. (2014, November 28). *Basics of Geomatics* (2009th ed.). Springer.
- [15.] Habib, A., Ghanma, M., & Taita, M. (2004b). PS ThS 1 Integration and Fusion of Data and Models . *Integration of Lidar and Photogrammetry for Close Range Applications* . <https://www.isprs.org/proceedings/xxxv/congress/comm5/papers/697.pdf>
- [16.] Jackson, B. (2021, December 17). *Fixed Wing vs Multirotor Drones for Surveying*. COPTRZ. Retrieved September 10, 2022, from <https://coptrz.com/fixed-wing-vs-multirotor-drones-for-surveying/>
- [17.] Johnson, K., Nissen, E., Saripalli, S., Arrowsmith, J. R., McGarey, P., Scharer, K., Williams, P., & Blisniuk, K. (2014, October). Rapid mapping of ultrafine fault zone topography with structure from motion. *Geosphere*, 10(5), 969–986. <https://doi.org/10.1130/ges01017.1>
- [18.] Kanatani, K., & Sugaya, Y. (2010, December 22). Bundle Adjustment for 3-D Reconstruction: Implementation and Evaluation. *Bundle Adjustment for 3-D Reconstruction: Implementation and Evaluation*, 27–35.
- [19.] Kingslake, R. (1942, March 1). Lenses for Aerial Photography*. *Journal of the Optical Society of America*, 32(3), 129. <https://doi.org/10.1364/josa.32.000129>

- [20.] Kolb, A., Barth, E., Koch, R., & Larsen, R. (2010, March). Time-of-Flight Cameras in Computer Graphics. *Computer Graphics Forum*, 29(1), 141–159. <https://doi.org/10.1111/j.1467-8659.2009.01583.x>
- [21.] Kugler, L. (2019, October 24). Real-world applications for drones. *Communications of the ACM*, 62(11), 19–21. <https://doi.org/10.1145/3360911>
- [22.] La Rocca, A. (n.d.). *A photogrammetry application to rockfall monitoring: the Belca, Slovenia case study* [MA Thesis]. Politecnico di Torino.
- [23.] Liu, T., Burner, A. W., Jones, T. W., & Barrows, D. A. (2012, October). Photogrammetric techniques for aerospace applications. *Progress in Aerospace Sciences*, 54, 1–58. <https://doi.org/10.1016/j.paerosci.2012.03.002>
- [24.] Lowe, D. G. (2004, November). Distinctive Image Features from Scale-Invariant Keypoints. *International Journal of Computer Vision*, 60(2), 91–110. <https://doi.org/10.1023/b:visi.0000029664.99615.94>
- [25.] Luhman, T., Robson, S., Kyle, S., & Harley, I. (2011, July 1). *Close Range Photogrammetry: Principles, Techniques and Applications* (Cdr). Whittles Publishing.
- [26.] Mol, L., & Clarke, L. (2019, July 30). Integrating structure-from-motion photogrammetry into rock weathering field methodologies. *Earth Surface Processes and Landforms*, 44(13), 2671–2684. <https://doi.org/10.1002/esp.4693>
- [27.] Osborn, J., Dell, M., Stone, C., Iqbal, I., Lacey, M., Lucieer, A., & McCoull, C. (2018, July). Deployment and integration of cost-effective, high spatial resolution, remotely sensed data for the Australian forestry industry. *Photogrammetry for Forest Inventory*, 1–86. https://www.fwpa.com.au/images/resources/-2018/Photogrammetry_for_forest_inventory_June_2018.pdf
- [28.] Pepe, M., & Costantino, D. (2020, October 22). UAV Photogrammetry and 3D Modelling of Complex Architecture for Maintenance Purposes: the Case Study of the Masonry Bridge on the Sele River, Italy. *Periodica Polytechnica Civil Engineering*. <https://doi.org/10.3311/ppci.16398>

- [29.] Peppas, M. V., Morelli, L., Mills, J. P., Penna, N. T., & Remondino, F. (2022, May 30). Handcrafted and Learning-Based Tie Point Features – Comparison Using The EUROSUR RPAS Benchmark Dataset. *The International Archives of the Photogrammetry, Remote Sensing and Spatial Information Sciences*, XLIII–B2, 1183–1190. <https://doi.org/10.5194/isprs-archives-xliii-b2-2022-1183-2022>
- [30.] Pilar Valerga Puerta, A., Aletheia Jimenez-Rodriguez, R., Fernandez-Vidal, S., & Raul Fernandez-Vidal, S. (2020, October 28). *Photogrammetry as an Engineering Design Tool. Product Design*. <https://doi.org/10.5772/intechopen.92998>
- [31.] Przybilla, H.-J. & Wester-Ebbinghaus, W. (1979): Bildflug mit ferngelenktem Kleinflugzeug. *Bildmessung und Luftbildwesen*, 47, 137-142.
- [32.] *RealityCapture - 3D Models from Photos and/or Laser Scans*. (n.d.). Retrieved September 10, 2022, from <https://www.capturingreality.com/>
- [33] Saczuk, E. (2020, March 30). Chapter 1.3 – Ground Control Points – *Processing Multi-spectral Imagery with Agisoft MetaShape Pro*. Pressbooks. Retrieved September 10, 2022, from <https://pressbooks.bccampus.ca/ericsaczuk/chapter/chapter-1-3-ground-control-points/>
- [34] Schenk, T. (2005, season-03). *Introduction to Photogrammetry*. The Ohio State University. <https://www.mat.uc.pt/~gil/downloads/IntroPhoto.pdf>
- [35.] Sherwood, C. R., Warrick, J. A., Hill, A. D., Ritchie, A. C., Andrews, B. D., & Plant, N. G. (2018, November 1). Rapid, Remote Assessment of Hurricane Matthew Impacts Using Four-Dimensional Structure-from-Motion Photogrammetry. *Journal of Coastal Research*, 34(6), 1303. <https://doi.org/10.2112/jcoastres-d-18-00016.1>
- [36.] Kumar, M. V. K. S., World Meteorological Organization, India. Meteorological Department, Organisation Météorologique Mondiale, Pacific, C. F. S. S. A. T. E. I. A. A. T., Indian Institute of Remote Sensing, India. National Remote Sensing Agency, Indian Space Research Organisation. Space Applications Centre, World Meteorological Organization, India. Meteorological Department, Centre for Space Science and Technology Education in Asia and the Pacific, Indian Institute of Remote Sensing, India. National Remote Sensing Agency, & Indian

Space Research Organisation. Space Applications Centre. (2004). *Satellite Remote Sensing and GIS Applications in Agricultural Meteorology: Proceedings of the Training Workshop 7-11 July, 2003, Dehra Dun, India*. World Meteorological Organisation.

[37.] Slattery, K. T., & Slattery, D. K. (2013, April). Modeling Earth Surfaces for Highway Earthwork Computation Using Terrestrial Laser Scanning. *International Journal of Construction Education and Research*, 9(2), 132–146. <https://doi.org/10.1080/15578771.2012.700298>

[38] Finding Your Brownstone– IN 1924 – *The Brownstone Detectives*. (2020, May 22). Retrieved September 10, 2022, from <https://www.brownstonedetectives.com/finding-your-brownstone-in-1924/>

[39] Triggs, B., McLauchlan, P. F., Hartley, R. I., & Fitzgibbon, A. W. (2000). Bundle Adjustment — *A Modern Synthesis*. *Vision Algorithms: Theory and Practice*, 298–372. https://doi.org/10.1007/3-540-44480-7_21

[40] Venier, L. A., Swystun, T., Mazerolle, M. J., Kreutzweiser, D. P., Wainio-Keizer, K. L., McIlwrick, K. A., Woods, M. E., & Wang, X. (2019, November 27). Modelling vegetation understory cover using LiDAR metrics. *PLOS ONE*, 14(11), e0220096. <https://doi.org/10.1371/journal.pone.0220096>

[41] Wackwitz, K., & Bödecker, H. (2008, May). UAV Workflow Integration. *Unlocking the Full Potential of Aerial Data*. <https://leica-geosystems.com/>

[42] Wanninger, L. (2008, June 16). *Introduction to Network RTK*. Wasoft. <http://www.wasoft.de/e/iagwg451/intro/introduction.html>

[43] Wester-Ebbinghaus, W. (2006, August 26). Aerial Photography by Radio Controlled Model Helicopter. *The Photogrammetric Record*, 10(55), 85–92. <https://doi.org/10.1111/j.1477-9730.1980.tb00006.x>

[44.] Williams, R. S., & Carter, W. D. (1976). ERTS-1, a new window on our planet. *Professional Paper*. <https://doi.org/10.3133/pp929>

[45] Wolf, P., DeWitt, B., & Wilkinson, B. (2014, January 7). *Elements of Photogrammetry with Application in GIS, Fourth Edition* (4th ed.). McGraw Hill.

[46.] Zhang, Y., Xiong, J., & Hao, L. (2011, June). Photogrammetric processing of low-altitude images acquired by unpiloted aerial vehicles. *The Photogrammetric Record*, 26(134), 190–211.

<https://doi.org/10.1111/j.1477-9730.2011.00641.x>

Acknowledgment

First, I would like to thank Professor Filiberto Chiabrando for giving me the opportunity to work in this field and for his unwavering support during this period. He always made me feel that the door was open to helping me whenever I had a problem. I am grateful to Alessio Calantropio and Lorenzo Teppati Losè for their endless patience with me and their unending willingness to teach something new, for their kindness to minimize the obstacles in this process for me.

I want to thank my mother Menekse, my father Yasar, my sister Pinar and my cousin Safa for their unconditional support throughout my life, for always trusting me, and for providing me with the necessary motivation to go further under any circumstances.

I would like to express my debt of gratitude to my friends Emir Akbuga, Eren Can Katnas, and Hilal Uney who make me feel more than siblings, for always being there for me, finding things to make me laugh, and showing that I can always be reached when I call and showing that true friendship will remain even after years of childhood.

I am also grateful to my friends Kamil, Meltem, Eda, Alper, Tolunay, and Ugur who never stopped believing in me.

I would also like to thank Gozde, Stefania, Mariella, Marco, and Amri for their love and help throughout my stay in Italy.